الجمهورية الجزائرية الديمقراطية الشعبية République Algérienne Démocratique et Populaire وزارة التعليم العالي والبحث العلمي

Ministère de l'enseignement supérieur et de la recherche scientifique

Université Mohamed Khider Biskra Faculté des Sciences et de la technologie Département : Génie Electrique

Ref:....



جامعة محمد خيضر بسكرة كلية العلوم والتكنولوجيا قسم: الهندسة الكهربائية

المرجع:

Thèse présentée en vue de l'obtention Du diplôme de

Doctorat LMD en Génie Electrique

Option: Energie Renouvelable

Techniques Modernes de gestion d'énergie d'un système de stockage hybride, dédié au véhicule électrique

Présentée par :

HASROURI Malika

Soutenue publiquement le 12/05/2025 devant le Jury composé de :

SAADI Ramzi	Professeur	Président	Université de Biskra
CHARROUF Omar	MCA	Directeur de thèse	Université de Biskra
BETKA Achour	Professeur	Co-directeur	Université de Biskra
DRID Said	Professeur	Examinateur	HNS RE&ESD Batna
MOHAMMEDI Messaoud	MCA	Examinateur	Université de Biskra

الجمهورية الجزائرية الديمقر اطية الشعبية Democratic and Popular Republic of Algeria وزارة التعليم العالي والبحث العلمي Ministry of Higher Education and Scientific Research

Mohamed Khider University Biskra Faculty of Science and Technology Department: Electrical Engineering



جامعة محمد خيضر بسكرة كلية العلوم والتكنولوجيا قسم: الهندسة الكهربانية

المرجع:

Ref:....

A thesis submitted for the degree of

Doctor of Philosophy in Electrical Engineering

Option: Renewable Energy

Modern energy management techniques for a hybrid storage system dedicated to electric vehicles

Presented by:

HASROURI Malika

Publicly defended on 12/05/2025, in front of the Jury composed of:

SAADI Ramzi	Professor	President	University of Biskra
CHARROUF Omar	Associate Professor A	Supervisor	University of Biskra
BETKA Achour	Professor	Co-supervisor	University of Biskra
DRID Said	Professor	Examiner	HNS RE&ESD Batna
MOHAMMEDI Messaoud	Associate Professor A	Examiner	University of Biskra



To

my parents, who never stopped believing in me
my sisters and brothers, my strength and unwavering support in life
all those who encouraged me during tough times

I dedicate this simple work



 $m{T}$ irst and foremost, all praise is due to Allah, who blessed me with the strength and patience to complete this thesis.

I would like to express my sincere gratitude to my thesis supervisors Dr. CHAROUF Omar, and Pr. BETKA Achour for their constant guidance and support throughout years of collective work at the LGEB laboratory in Biskra. This thesis would not have been possible without their supervision. The enthusiasm, patience, humility, and wisdom I see in them have inspired me in not only my research but also in my life.

I would also like to thank the team members Pr. ABDEDDAIM Sabrina, and Dr. Tiar Mourad, for their availability and invaluable advice. I would also like to thank Mr. ZOUZOU Salah Eddine, the previous director, and Mr. NAIMI Djemai, the current director of the LGEB Laboratory, for their efforts in providing a suitable research environment.

Moreover, I would like to thank Mr. SAIDI Ramzi, Professor at the University of Biskra, who honored me to chair the jury for this thesis. I would also like to thank the honorable members of the jury who agreed to assess my thesis, Mr. DRID Said, Professor at the University of Batna 2, and Mr. MOHAMMEDI Messaoud, Associate Professor A at the University of Biskra.

Last but not least, my special thanks go to my parents, everything I have accomplished is a testament to their love, sacrifices, and constant belief in me, for which I am eternally thankful.



This thesis presents the development and the experimental validation of an Energy

Management System for a real Hybrid Energy Storage System using lithium-ion batteries and supercapacitors in an electric vehicle emulator. The EMS allocates power based on source dynamics, managing real-time power distribution between the battery and SC, with the SC assisting the battery during high demands and recovering braking energy. Frequency-sharing techniques have been proposed to achieve this goal, including two innovative adaptive Wavelet Transform based on the development of the conventional versions. The first method employs an adaptive wavelet technique within the EMS, adjusting the wavelet decomposition level according to the state of charge of the supercapacitor. This allows for dynamic changes in the wavelet decomposition during high power peaks and when the supercapacitor has a high charge, reducing the battery's workload. The second method integrates an adaptive wavelet with adaptive fuzzy logic within the EMS. This approach modifies wavelet transform levels and fuzzy logic outputs using a k-means-SVM pattern recognition system. The combination of k-means clustering and Support Vector Machine classification enhances driving pattern recognition, enabling real-time decision-making. The adaptive wavelet dynamically manages power distribution between the battery and SC, while the fuzzy logic maintains the supercapacitor at optimal levels and shields the battery from peak current surges. These proposed systems maintain the supercapacitor charge by dynamically managing power between the battery and SC, taking into account real-time driving conditions. As a result, it reduces battery aging, extends battery lifespan, and lowers overall operational costs in electric vehicles.

Keywords: Electric vehicle, Energy Management System, Adaptive wavelet transform, Adaptive fuzzy logic, Driving pattern recognition



Cette thèse présente le développement et la validation expérimentale d'un système de gestion

de l'énergie pour un système de stockage d'énergie hybride réel utilisant des batteries lithium-ion et des supercondensateurs dans un émulateur de véhicule électrique. Le système de gestion de l'énergie alloue la puissance en fonction de la dynamique de la source, en gérant la distribution de la puissance en temps réel entre la batterie et le système de stockage d'énergie, le système de stockage d'énergie aidant la batterie en cas de forte demande et récupérant l'énergie de freinage. Des techniques de partage des fréquences ont été proposées pour atteindre cet objectif, y compris deux transformées d'ondelettes adaptatives innovantes basées sur le développement des versions conventionnelles. La première méthode utilise une technique d'ondelettes adaptative au sein de l'EMS, ajustant le niveau de décomposition des ondelettes en fonction de l'état de charge du supercondensateur. Cela permet des changements dynamiques dans la décomposition des ondelettes pendant les pics de puissance élevés et lorsque le supercondensateur a une charge élevée, réduisant ainsi la charge de travail de la batterie. La deuxième méthode intègre une ondelette adaptative avec logique floue adaptative (AWT-AFL) au sein de l'EMS. Cette approche modifie les niveaux de transformation des ondelettes et les sorties de la logique floue à l'aide d'un système de reconnaissance des formes k-means-SVM. La combinaison du regroupement k-means et de la classification Support Vector Machine améliore la reconnaissance des schémas de conduite, ce qui permet une prise de décision en temps réel. L'ondelette adaptative gère dynamiquement la répartition de la puissance entre la batterie et le supercondensateur, tandis que la logique floue maintient le supercondensateur à des niveaux optimaux et protège la batterie contre les pointes de courant. Les systèmes proposés maintiennent la charge du supercondensateur en gérant dynamiquement la puissance entre la batterie et le SC, en tenant compte des conditions de conduite en temps réel. Ils permettent ainsi de réduire le vieillissement de la batterie, d'allonger sa durée de vie et de réduire les coûts de fonctionnement globaux des véhicules électriques.

Mots-clés : Véhicule électrique, Système de gestion de l'énergie, Transformée en ondelettes adaptative, Logique floue adaptative, Reconnaissance des modèles de conduite



تقدم هذه الأطروحة تطوير والتحقق التجريبي من نظام إدارة الطاقة لنظام تخزين طاقة هجين حقيقي يستخدم بطاريات الليثيوم أيون والمكثفات الفائقة في محاكي سيارة كهربائية. يقوم نظام إدارة الطاقة بتوزيع الطاقة بناءً على ديناميكيات المصدر، حيث يدير توزيع الطاقة في الوقت الفعلي بين البطارية والمكثف الفائق، حيث يساعد المكثف البطارية أثناء الطلبات العالية ويستعيد الطاقة أثناء الكبح. تم اقتراح تقنيات تقاسم التردد لتحقيق هذا الهدف، بما في ذلك تقنيتين مبتكرتين مبنيتين على تطوير التحويل المويجي التقليدي. تعتمد الطريقة الأولى على تقنية تحويل مويجي تكيفي داخل نظام إدارة الطاقة، حيث تعدل مستوى تحليل التحويل المويجي وفقًا لحالة شحن المكثف الفائق. يسمح هذا بإجراء تغييرات ديناميكية في التحويل المويجي أثناء الذروة العالية للطاقة وعندما يكون المكثف الفائق عند مستوى شحن عالى، مما يقلل من العبء على البطارية. أما الطريقة الثانية فتدمج التحويل المويجي التكيفي مع المنطق الضبابي التكيفي داخل نظام إدارة الطاقة. تقوم هذه التقنية بتعديل مستويات التحويل المويجي ومخرجات المنطق الضبابي باستخدام نظام التعرف على الأنماط المستند إلى التجميع باستخدام k-means وتصنيف الآلات الداعمة SVM. يعزز هذا المزيج من التجميع وتصنيف الآلات الداعمة من التعرف على أنماط القيادة، مما يمكّن اتخاذ القرارات في الوقت الفعلي. يدير التحويل المويجي التكيفي توزيع الطاقة ديناميكيًا بين البطارية والمكثف الفائق، بينما يحافظ المنطق الضبابي على مستويات شحن المكثف الفائق ويحمى البطارية من تيارات الذروة. تساهم هذه الأنظمة المقترحة في الحفاظ على شحن المكثف الفائق من خلال إدارة الطاقة ديناميكيًا بين البطارية والمكثف الفائق، مع مراعاة ظروف القيادة في الوقت الفعلى. ونتيجة لذلك، يقلل من شيخوخة البطارية، ويطيل عمر ها، ويخفض تكاليف التشغيل الإجمالية للسيارات الكهربائية. الكلمات المفتاحية: السيارة الكهربائية، نظام إدارة الطاقة، تحويل الموجات التكيفي، المنطق الضبابي التكيفي، التعرف على أنماط القيادة

Contents

List of T	Γables		iii
List of F	Figures		iv
List of a	acronym	s and symbols	vii
		1 Introduction	
	•		1
		Background and motivation	
		Contributions	
		Thesis plan	
	_	2 Review of hybrid energy storage systems in the context of electric vehic	
		ntroduction	
4		Electric Vehicle	
		. Historic	
		2. Electric vehicle prices and sales	
		3. Types of EVs	
	2.2.4	I. The Multifaceted Dynamics of Electric Vehicle Adoption	10
2	2.3. E	Energy sources in electric vehicle	11
	2.3.1	Battery	11
		2.3.1.1 Choice of storage technology	11
		2.3.1.2 Battery price	13
	2.3.2	2. Supercapacitor	15
	2.3.3	3. Topologies	16
2	2.4. E	Energy Management Strategies	18
	2.4.1	. Rule-Based Energy Management Strategies	19
	2	2.4.1.1.Deterministic rule-based	19
	2	2.4.1.2.Frequency-based	20
		2.4.1.3.Fuzzy based	
		2. Optimization-based	
		2.4.2.1.Global optimization-based.	

Contents

		2.4	.2.2.Real-time optimization	25
	2.4	1.3.	Learning-Based Energy Management Strategies	27
	2.5.	Dr	iving Pattern Recognition-Based Energy Management Strategies	28
	2.6.	Co	nclusion	29
3.	Chapte	er 3	Modeling of hybrid energy storage systems and electric vehicles	
	3.1.	Int	roduction	31
	3.2.	En	ergy source modeling	31
	3.2	2.1.	Battery	31
	3.2	2.2.	Supercapacitor	35
	3.2	2.3.	Parameters identification	37
	3.3.	DO	bus modeling	42
	3.4.	DO	C/DC converter modeling	42
	3.5.	Tra	action chain modeling	43
	3.5	5.1.	Vehicle Dynamics model	43
	3.5	5.2.	Traction motor	45
	3.5	5.3.	Regeneration	47
	3.6.	Siz	ing of sources	48
	3.7.	Co	nclusion	52
4.	Chapte	er 4	Description of proposed strategies	
	4.1.	Int	roduction	54
	4.2.	HE	EV emulator	54
	4.2	2.1.	Description	54
	4.2	2.2.	System modeling	56
	4.2	2.3.	Converters control approaches	57
	4.2	2.4.	DC- link voltage control	59
	4.3.	Fre	equency-based energy management strategies	60
	4.3	3.1.	Fixed frequency-based energy management system:	60
	4.3	3.2.	Adaptive frequency-based energy management system	61
	4.4.	Wa	avelet-based energy management system	62
	4.4	4.1.	Conventional Wavelet-based Energy Management System	62
	4.7	1 2	Adaptive wavelet-based energy management system	65

Contents

4.5. Adaptive Wavelet-Adaptive Fuzzy Logic based K-Means-SVM			laptive Wavelet-Adaptive Fuzzy Logic based K-Means-SVM Pattern	
		Re	cognition	67
	4.	5.1.	Driving Pattern Recognition.	68
		4.5	5.1.1.Extraction of the driving patterns characteristic parameters	70
		4.5	5.1.2.K-means cluster	73
		4.5	5.1.3.SVM classifier	74
	4.	5.2.	Adaptive wavelet transform	76
	4.	5.3.	Adaptive fuzzy	77
	4.6.	Tra	action part control	80
	4.	6.1.	Speed control based on Sliding mode.	80
	4.	6.2.	Speed control based on Back-stepping	82
	4.	6.3.	Torque control based on PI controller	84
	4.7.	Co	nclusion	86
5.	Chapt	ter 5	Experimental validation and performance analysis	
	5.1.	Int	roduction	88
	5.2.	De	scription du banc d'essai	88
	5.	2.1.	dSPACE dS1104 Card	90
	5.	2.2.	SEMIKRON Converter	91
	5.	2.3.	Sensors	92
	5.3.	Ex	perimental validation	93
	5.	3.1.	Adaptive wavelet-based supervisor	93
	5.	3.2.	Adaptive Fuzzy Logic based K-Means-SVM Pattern Recognition	
			supervisor	104
	5.4.	Co	nclusion	115
6.	Chapt	ter 6	Conclusion and future work	
	6.1.	Co	nclusion	117
	6.2. Future work		ture work	119
	6.3.	Pu	blication	120
•				120

List of Tables

2.1.	Comparative Analysis of Hybrid Energy Storage System Topologies	17
3.1.	Li-ion battery types	32
3.2.	The Parameter Identification Results of supercapacitor	11
4.1.	A dynamic frequency cut-off operation6	52
4.2.	The characteristic criteria used for the recognition of patterns	72
4.3.	The coordinates of the centroid	74
4.4.	Membership symbols	77
4.5.	Fuzzy rules.	77
5.1.	Hardware characteristics	39
5.2.	Detailed evaluation of the suggested EMS, the standard wavelet approach, and the	
	adaptive filter compared to a fixed cut-off frequency	03
5.3.	Comparison of Frequency-Based EMS Performance for Both Classical and Adaptive	
	Versions10	04
5.4.	Accuracy comparison of diverse machine learning techniques in Driving state	
	recognition10	05
5.5.	Assessment criteria results1	08
5.6.	Reduction in AWT RMS battery current compared to fixed-WT	09
5.7.	Comparison of the proposed EMS to AWT-FL and AWT in terms of battery current	
	RMS and peak reduction	11

List of Figures

1.1.	Emissions of greenhouse gases from the transportation sector worldwide1
2.1.	The development of electric vehicles: (a) Robert Anderson Electric vehicle, (b) "La
	Jamais Contente" Electric vehicle, (c) Riker Electric Tricycle ,(d) Enfield
	80007
2.2.	Global inventory of electric cars, comprising plug-in hybrid and battery electric
	vehicles
2.3.	Types of Electric Vehicles: (a) Battery Electric Vehicles; (b) Hybrid Electric Vehicles;
	(c) Fuel Cell Electric Vehicles; (d) Plug-in hybrid electric vehicles10
2.4.	The qualitative indicators of batteries
2.5.	Evolution of Batteries for Electric Vehicle Use across Generations
2.6.	Global lithium-ion battery demand 2022-203014
2.7.	Lithium-ion Battery Market Size 2022 to 203214
2.8.	Comparison between batteries and supercapacitor
2.9.	Topologies of HESSs integrating battery and SC sources
2.10	. Classification of energy management strategies for hybrid electric vehicle19
2.11.	. Electrical diagram of a Battery/Ultracapacitor EMS utilizing an Adjustable
Banc	dwidth Filter and Sliding-Mode Control
2.12	Detailed control framework of hybrid energy storage system in this study21
2.13	The model diagram of the fuzzy control module
2.14	Flow chart of Genetic Algorithm24
2.15	Model predictive control block diagram26
2.16	A schematic of Reinforcement Learning concept
3.1.	Schematics of Li-ion battery32
3.2.	The equivalent models of Li-ion battery: (a) Rint model, (b)Thevenin model, (c) PNGV
	model, (d)DP model
3.3.	Schematic illustration of (a) electrical double-layer capacitor, (b)pseudocapacitor,
	(c)hybrid supercapacitor35

3.4. Sup	percapacitor equivalent circuit models: (a) simple model with equivalent se	eries
resi	stance, (b)simple model with equivalent parallel resistance, (c)multi-brance	ch
mod	del	36
3.5. The	e flowchart of the parameter estimation process	38
3.6. Bat	tery parameters under different state of charge	38
3.7. MA	AFF-RLS algorithm concept	40
3.8. Para	ameter identification results using the MAFF-RLS algorithm: (a) ohmic re-	sistance
R_0	0; (b) polarization resistor R_cp; (c) polarization capacitor C_cp; (d) Forg	etting
fact	tor variation	41
3.9. Equ	nivalent circuit of the dc bus	42
3.10.	Schematic circuit of the buck-boost converter	43
3.11.	Schematic representation of forces acting on a vehicle in motion	45
3.12.	Equivalent circuit of permanent magnet DC motor	46
3.13.	Open-loop PMDC block diagram	47
3.14.	Braking system model representation.	48
4.1. Top	pology Configuration of HEV	55
4.2. Sys	stem identification principle	58
4.3. A so	chematic representation of the adaptive frequency separation technique	61
4.4. Cor	ncept of Haar wavelet transform: (a)Decomposition phase ;(b) Reconstruct	tion
pha	ise	63
4.5. Slid	ding window concept	64
4.6. Wa	velet transform technique diagram	65
4.7. Sch	nematic representation of adaptive wavelet transform technique	66
4.8. Ada	aptive process flowchart	67
4.9. The	e concept of Adaptive Wavelet-Adaptive Fuzzy Logic based K-Means-SV	M Pattern
Rec	cognition EMS	68
4.10.	Driving pattern recognition framework	69
4.11.	Principal component eigenvalues and cumulative variance contribution	ı rate71
4.12.	Correlation of the characteristic features	72
4.13.	Cluster number determination using the Calinski-Harabasz index	73
4 14	Results of K-means clustering	74

List of Figures

4.15	Diagram of the voting procedure76
4.16	Fuzzy logic input membership functions
4.17	The output of adaptive fuzzy logic membership function79
4.18	Adaptive fuzzy logic controller process80
4.19	PI current control85
5.1.	Experimental bench89
5.2.	Structure of the dSPACE DS1104 controller board90
5.3.	The connector panel of DS1104 Card91
5.4.	Sensors:(a) Current sensor; (b) Voltage sensor; (c) A tachogenerator92
5.5.	Speed tracking performance :(a) Profile 1; (b) Profile 294
5.6.	Motor speed94
5.7.	Dc-bus voltage9
5.8.	Current of load99
5.9.	Load current FFT analysis: (a) Section 1 (green) load current during urban driving cycle
	(b) Section 2 (green) load current during high-speed driving cycle; (c) Section 3 (green)
	load current during suburban driving cycle90
5.10	Currents of batteries and supercapacitors using tested techniques: (a) Battery
	current over various cut-off frequencies; (b) Current of the supercapacitor with various
	cut-off frequencies; (c) Battery current with different wavelet levels and the adaptive
	method; (d) Current of the supercapacitor with different wavelet levels and the adaptive
	technique9
5.11	. State of charge of Battery and supercapacitor under validated techniques:(a)
	Variations in battery SoC at various cut-off frequencies;(b) Variations in supercapacitor
	SoC at various cut-off frequencies;(c) Battery SOC at various wavelet levels and
	adaptive method;(d) Supercapacitor SOc at varying wavelet levels and the adaptive
	technique9
5.12	Total RMS current across various techniques100
5.13	The total maximum current with different techniques10
5.14	Delta SOC with various techniques
5.15	Total Losses under different techniques implementation
5.16	

List of Figures

5.17.	The first motor speed
5.18.	The second motor Current
5.19.	Curent of load
5.20.	Results of experiments with wavelet transform, both fixed and adaptive: (a)
Curre	nt of battery; (b) Current of supercapacitor; (c) Battery state of charge; (d)
Super	reapacitor state of charge
5.21.	Results of experiments conducted with various adaptive techniques: (a) Current of
batter	y; (b) Current of supercapacitor; (c) Battery state of charge; (d) Supercapacitor
state	of charge
5.22.	The distribution of battery current peaks under adopted techniques111
5.23.	Battery current rate of change Distribution within tested strategies113
5.24.	Dc-bus voltage using adopted strategies

List of acronyms and symbols

EV Electric vehicles

BEV battery electric vehicle
HEV Hybrid Electric Vehicle
ESS Energy storage system

HESS Hybrid energy storage systems
EMS Energy Management Strategy

EPS Electrical power system

DS Driving system
SCs Supercapacitors
Soc State of charge
Li-ion lithium-ion

ECM Equivalent circuit model

SPET Simulink Parameter Estimation Toolbox

RLS Recursive Least Squares

MAFF-RLS Modified Adaptive Forgetting Factor-Based Recursive Least Square

PMDC Permanent magnet direct current

HWFET Highway Fuel Economy Test Driving cycle

WLTP Worldwide Harmonized Light Vehicles Test Procedure Driving cycle

FFT Fast Fourier transformation

WT Wavelet transform
HWT Haar wavelet transform
DPR Driving pattern recognition

FL Fuzzy logic

SVM Support Vector Machines
PCA Principal Component Analysis

RMS Root mean Square WT Wavelet transform

AWT Adaptive wavelet transform

AWT-FL Adaptive wavelet transform-Fuzzy logic

AWT-AFL Adaptive wavelet transform-Adaptive Fuzzy logic

SM Sliding Mode control
BS Backstepping control

FTP72 Federal Test Procedure Driving cycle

M1 The first motor
M2 The second motor P_m The mechanical power

η	The charging/discharging efficiency
$\mathit{fc}_{\mathrm{max}}$, $\mathit{fc}_{\mathit{nom}}$, $\mathit{fc}_{\mathrm{min}}$	Maximum, nominal, and minimum Cut-off frequency
\boldsymbol{n} , f_{s} , f_{c}	The number of decomposition levels, sampling frequency, and frequency of
	power demand on the battery pack
I_{RMS} , $i_{\mathit{rms}-b}$, $i_{\mathit{rms}-sc}$	The total RMS current, Battery RMS current, and Supercapacitor RMS current
N , i_{b-mes_i} , i_{sc-mes_i}	The number of data points in the signal, the individual data points of the
N , ι_{b-mes_i} , ι_{sc-mes_i}	measured battery, and the supercapacitor current signal
Δ SoC	Delta State of Charge
L_T , L_b , L_{sc}	Total losses, Battery losses, and supercapacitor losses
	Battery and Supercapacitor Internal Resistance
R_b , R_{sc}	Load current, Battery, and Supercapacitor controlled currents
$oldsymbol{i}_l$, $oldsymbol{i}_b$, $oldsymbol{i}_{sc}$	DC-link voltage and Reference DC-link voltage
v_{dc} , v_{dc-ref}	Measured Battery and Supercapacitor currents
i_{b-mes} , i_{sc-mes}	Battery and Supercapacitor currents references obtained from Wavelet transform
$oldsymbol{i}_b^*$, $oldsymbol{i}_{sc}^*$	Battery and Supercapacitor currents references obtained from Fuzzy logic
$oldsymbol{i}_{b-ref}$, $oldsymbol{i}_{sc-ref}$	Battery, Supercapacitor, and dc motors converter duty ratios
α_b , α_{sc} , α_{m1} , α_{m2}	Buck-Boost converter switches states
$S_{1,\dots,8}$	Low and high pass filter
Lo_D , Hi_D	Number of decomposition levels, Approximation and detail part of the wavelet
\boldsymbol{n} , $\boldsymbol{A}_{\!\scriptscriptstyle n}$, $\boldsymbol{D}_{\!\scriptscriptstyle n}$	decomposition
	Correlation coefficient matrix
R	The contribution rate of each sample principal component
Fi Fk	Cumulative contribution of principal component samples
$P(i_p)$	Peak current probability
$n(i_p)$	Number of favorable findings (events where the condition is satisfied)
n(s)	The total number of samples processed
$\frac{di_b}{dt}$	Rate of change of battery current
Fv_{dc}	Dc-link voltage fluctuations

Chapter 1

Introduction

1.1. Background and motivation

The rapid progress of urbanization has indeed led to an increase in environmental contaminants in urban areas, including sulfur dioxide, nitrogen oxides, carbon monoxide, and particulate matter [1]. This environmental burden is closely associated with the transport industry, which contributes over 22% to global energy usage and greenhouse gas emissions, with road transport alone responsible for more than 70% of total domestic and international transport greenhouse gas emissions As shown in Fig 1.1 [2]. This challenge is particularly heightened in urban settings, where cities consume 75-78% of global energy resources and generate 67-80% of worldwide greenhouse gas emissions. It is projected that by 2050, approximately 68% of the world's population will reside in cities [3] [4], the significance of this issue is set to escalate. Consequently, the increasing popularity of electric vehicles in recent years stems from their lower environmental impact and potential to mitigate greenhouse gas emissions, coupled with their superior efficiency compared to traditional gasoline-powered vehicles.

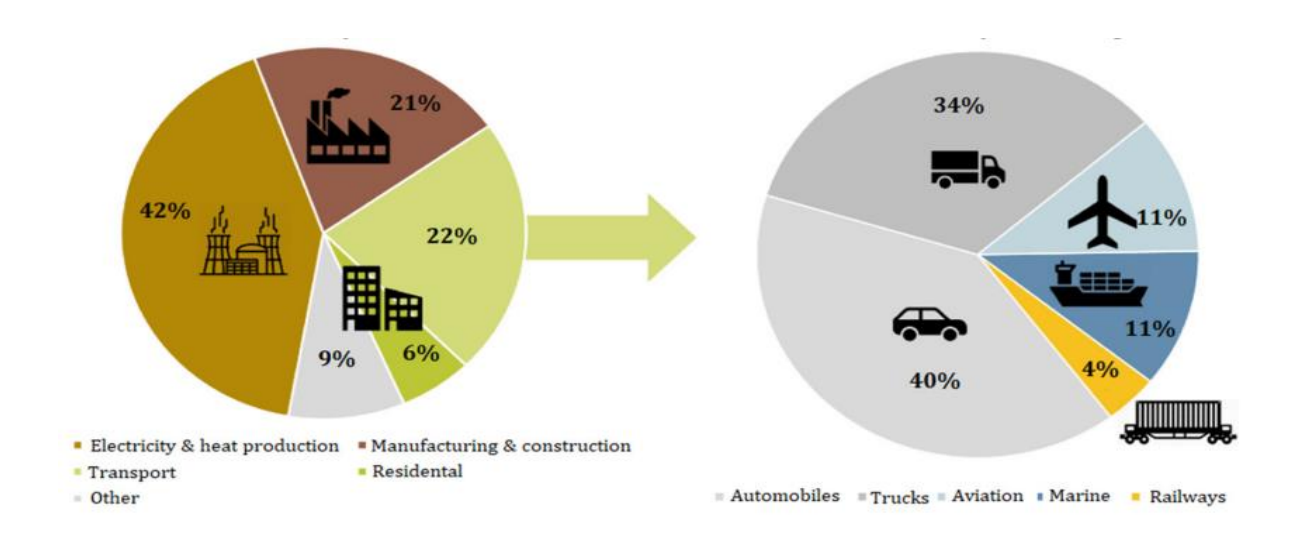


Fig 1.1: Emissions of greenhouse gases from the transportation sector worldwide

In the context of addressing these environmental concerns, The European Energy Mix estimates that CO2 emissions in 2010 were at 300 CO2 g/kWh. The deployment of sustainable energy sources and the potential retirement of nuclear power plants are expected to reduce CO2 emissions to below 200 g/kWh by 2030, and maybe even lower. The CO2 emissions per vehicle will drop

from 66 CO2 g/km in 2010 to under 30 CO2 g/km in 2030 when the consumption and emissions of the electric vehicles used to generate the electricity are taken into account [5]. This transition towards a cleaner energy mix aligns with the increasing trend of adopting electric vehicles, offering a promising solution to the environmental challenges associated with the rise in pollutants due to urbanization.

1.2.Contributions

This thesis aims to develop a modern real-time EMS based on the Adaptive wavelet technique within a hybrid storage system dedicated to the EV encompassing batteries and supercapacitors. This development allows for optimized energy assignment and prolongs the battery lifetime, thereby reducing EV expenses. This aim will be achieved through the following original contributions:

- A comprehensive review of EVs has been carried out, offering insights into both the current state of EMSs and potential avenues for future research.
- -A selection of methods blending wavelet techniques with artificial intelligence has been made to effectively manage the energy flow in the hybrid system and account for driving conditions. These EMSs are described as follows:
 - A novel AWT technique responsive to the supercapacitor state of charge is utilized to
 dynamically regulate the decomposition level. This innovative approach provides a fresh
 and streamlined method of adaptability in contrast to traditional pattern recognition drives.
 Particularly noteworthy is its ability to adjust the wavelet decomposition level during
 transient high peaks and when the supercapacitor holds ample reserves, thus easing the
 workload on the battery.
 - An improved AWT is presented integrating Dynamic Pattern Recognition principles, allowing for flexibility in addressing the dynamic complexities of various driving scenarios. Enhancement of the driving pattern recognition system's capabilities is accomplished through the fusion of k-means clustering and SVM classification techniques. Unsupervised classification of driving behaviors is facilitated by k-means clustering, establishing a basis for data-driven insights. Patterns are classified based on clusters

through the SVM classifier, thus enhancing real-time decision-making and substantially bolstering the adaptability of the EMS to driving conditions.

• A progressive approach to fuzzy logic is adopted over conventional methods, introducing adaptability into the FL architecture. Real-time adjustments are made to membership functions and rules to ensure harmonization with evolving driving conditions. This continuous adjustment guarantees the preservation of the supercapacitor at the desired level, acting as a preventive measure for the battery against occurrences of peak current.

-The experimental validation of the proposed strategies using real-world sources which faces challenges due to the offline methodology. This offline nature introduces complexities in implementing the strategy experimentally. However, the importance attached to rigorously testing and improving the viability of the strategy under realistic conditions is emphasized by the attempt to verify the proposed approach with real data sources.

1.3. Thesis plan

The organization of this thesis is outlined as follows:

Chapter 1: an overview of the context in which the research will take place, motivation, and thesis contributions are introduced.

Chapter 2: This chapter provides the fundamentals of HEVs, exploring the multifaceted dynamics influencing their adoption, including financial considerations. Various types and architectures of HEVs are identified and compared, with detailed explanations of the adoption of HESS incorporating batteries and supercapacitors. Furthermore, existing EMSs are categorized, and the strengths and limitations of each category are briefly reviewed.

Chapter 3: will focus on the modeling and sizing of the various components comprising the power supply and traction system of the EV. Accurate modeling of these components is essential for deriving suitable control laws, encompassing energy sources, associated converters, the dynamic vehicle model, and the motors utilized for simulating the traction system.

Chapter 4: a novel approach is introduced utilizing an AWT technique-based EMS. This technique customizes the wavelet decomposition level based on the supercapacitor's state of charge. In the

second part of this chapter, an adaptive wavelet-adaptive fuzzy logic technique (AWT-AFL) within an EMS is developed. This technique dynamically adjusts the wavelet transform levels and fuzzy logic outputs according to the k-means-SVM-driven pattern recognizer. where it focuses on achieving consistent maintenance of the supercapacitor around the desired level and protection of the battery from peak current surges.

Chapter 5: focuses on the experimental validation of the proposed strategies within a battery/supercapacitor HESS tested on a small-scale EV emulator where a detailed description of the experimental set-up is given. The practical aspects of numerical implementation and strategy calibration are discussed, and the performance of the various strategies is evaluated.

Chapter 6 serves as the conclusion of the thesis, delving into potential avenues for future research.

Chapter 2

Review of hybrid energy storage systems in the context of electric vehicles

2.1.Introduction

In this opening chapter, we place the research in a general context by briefly describing the various types and architectures of HEVs. Following a brief historical perspective, we delve into the complex dynamics influencing the adoption of EVs, considering both technological and financial aspects, with a particular focus on battery-related considerations. Additionally, we provide an examination of on-board energy sources, elucidating their characteristics and the criteria used to compare them. In the second part, we offer a succinct review of energy management techniques for hybrid systems. This understanding serves as a foundation for informed decisions regarding the strategy employed in this study.

2.2. Electric Vehicle

An electric vehicle is a vehicle that uses electric energy stored in a battery or other devices for energy storage and is operated by an electromotor. EVs have a higher degree of efficiency and better driving characteristics compared to vehicles powered by internal combustion engines of equal power. They do not emit gases and do not create noise, making them environmentally friendly and suitable for urban environments [6]. EVs typically consist of a frame, an electric powertrain, and a transmission system. The electric powertrain includes an electric motor that receives power from a battery module and transmits power to the wheels. The frame provides structural support and may also include storage units for auxiliary power sources [7]. However, they may also have higher upfront costs and limited driving range, depending on the model and battery capacity[8] where the main problem with EVs is their autonomy. Scientists are developing better battery technology to increase driving range while reducing weight, cost, and charging time. These factors will eventually determine the direction of EVs[9].

2.2.1. Historic

The first electric vehicle can be traced back to a Scottish man named Robert Anderson, who created a non-rechargeable battery-powered vehicle that ultimately failed[10]. However, the first successful EV was known as the 'Electro boat' and 'Ricker electric vehicle,' manufactured by the Electric Vehicle Company in the 1890s. There are numerous theories and opinions about the first electric vehicle, but it is believed that the first experiment on an electric vehicle was performed in the middle of the 1830s, just after the discovery of Faraday's law [11]. Greece is also considered the homeland of the first modern electrical car, with the Enfild 8000 being one of the first electric

cars in the world [12]. In the early 20th century, electric vehicles experienced waves of popularity. However, they were eventually overshadowed by gasoline-fueled vehicles, which were mass-produced and sold at low prices [13]. It was not until the 1990s when the harmful effects of fossil fuels on the environment became a concern, that electric vehicles resurfaced as a viable option [14]. Today, EVs are becoming more mainstream, with many major automakers producing fully electric and hybrid electric models. Governments around the world are also promoting the adoption of EVs through incentives and regulations, to reduce greenhouse gas emissions and improve air quality[8]. Fig 2.1 depicts some of the referenced cars.

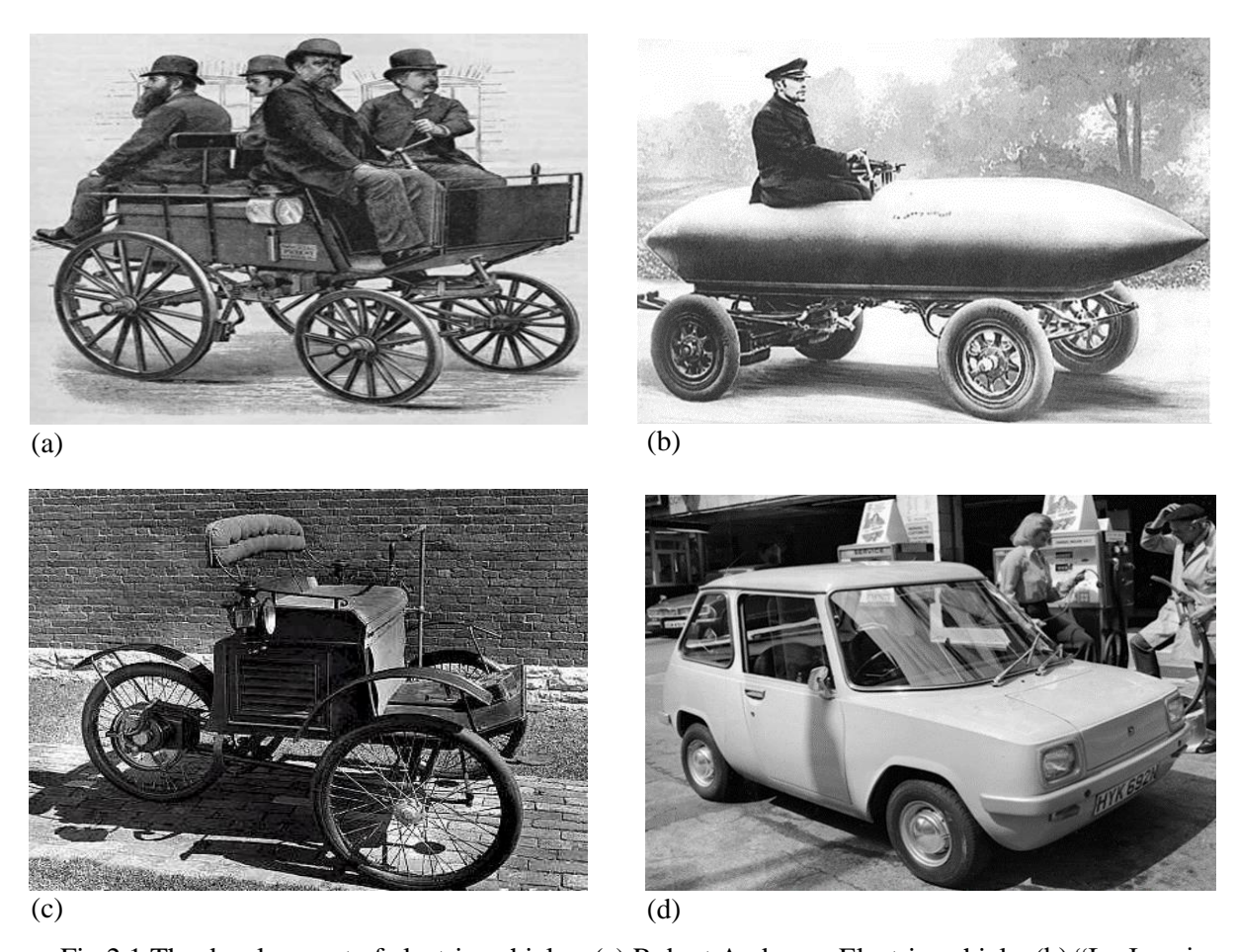


Fig 2.1 The development of electric vehicles: (a) Robert Anderson Electric vehicle, (b) "La Jamais Contente" Electric vehicle, (c) Riker Electric Tricycle, (d) Enfield 8000

2.2.2. Electric vehicle prices and sales

The price of EVs has been decreasing over time due to advancements in technology, economies of scale, and government incentives. According to a report by Bloomberg NEF, the average price is

expected to reach parity with traditional gas-powered vehicles by 2026. In 2021, the average price of a new EV in the US was around \$55,000, while the average price of a new gas-powered vehicle was around \$40,000 [15]. However, the total cost of ownership over the vehicle's lifespan, including fuel and maintenance, can be lower for EVs. In Europe and China, a similar trend is observed, with EVs often being more expensive upfront but potentially more cost-effective in the long run [16].

The EV market has witnessed substantial growth, with a projected threefold increase in EV users by 2030 compared to 2011, driven by advancements in battery technology improving vehicle autonomy[17]. Fig 2.2 illustrates the global electric car stock, including battery electric vehicles (BEVs) and plug-in hybrid electric vehicles (PHEVs), showing a consistent increase in market share over the past decade. In 2023, EV sales surged by 60%, resulting in 1 in 7 global automobiles being electric [9]. This growth not only led to a significant reduction in carbon emissions but also transformed the automotive landscape.

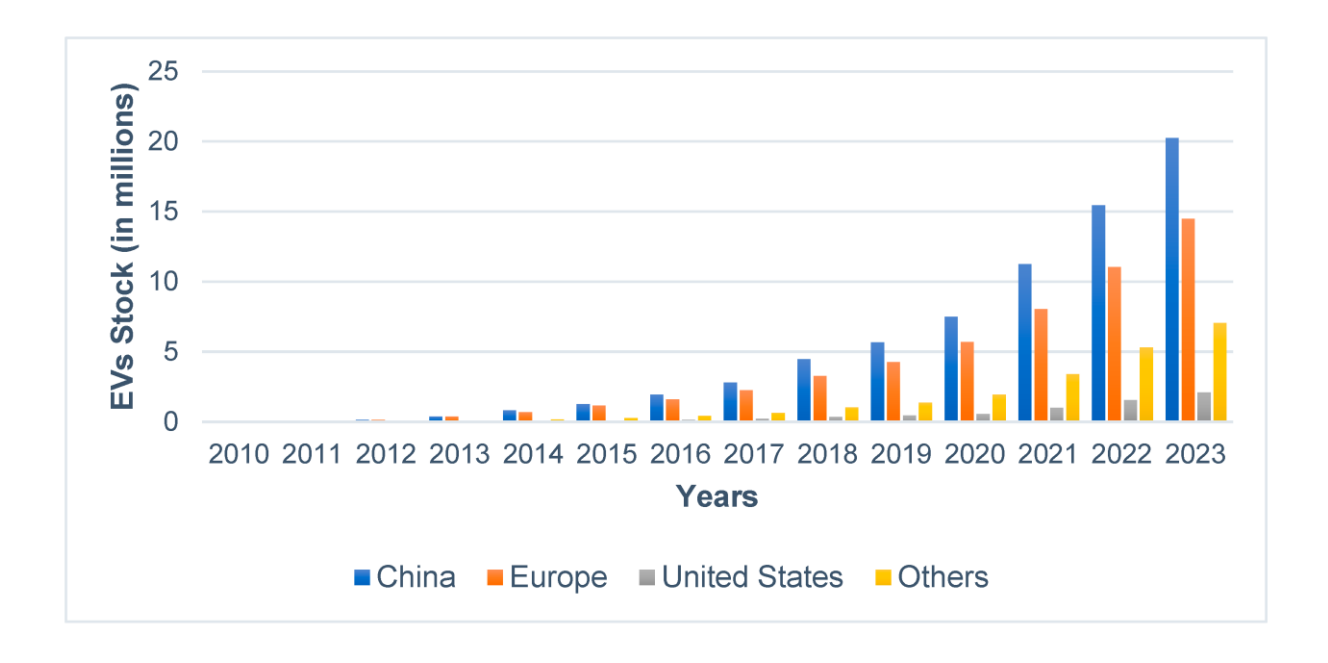


Fig 2.2: Global inventory of electric cars, comprising plug-in hybrid and battery electric vehicles.

China, the fastest-growing EV market, has set ambitious targets, where the global EV market surpassed 10 million sales in 2022, marking a 55% increase from the previous year, with China dominating by representing 59% of global EV sales. Europe emerged as the second-largest market,

accounting for 30% of the total EV population. The United States contributed 8% to global EV sales. This data suggests a promising future for the electric vehicle industry, with ongoing growth and increasing global adoption[18].

2.2.3. Types of EVs

EVs come in various types, including battery-electric vehicles, hybrid-electric vehicles, plug-in hybrid-electric vehicles, and fuel-cell electric vehicles as shown in Fig 2.3. They are classified based on their engine technology and configurations [18]:

- Battery Electric Vehicles: BEVs are powered solely by electricity stored in a rechargeable battery pack or supercapacitor. They produce zero tailpipe emissions, offering high efficiency and low maintenance costs. However, BEVs may suffer from range anxiety due to limited driving range per charge and the availability of charging infrastructure. Popular examples include the Tesla Model S, Nissan Leaf EV, and Tata Nexon EV.
- Hybrid Electric Vehicles: HEVs combine an internal combustion engine (ICE) with an electric motor, offering improved fuel efficiency and reduced emissions compared to traditional ICE vehicles. They utilize regenerative braking to recharge the battery and can operate in electric-only mode for short distances. HEVs like the Toyota Prius Hybrid, Honda Civic Hybrid, and Ford Escape. Hybrid provides a balance between electric power and fossil fuel reliance, making them a popular choice for drivers seeking increased efficiency without the range limitations of pure electric vehicles.
- Fuel Cell Electric Vehicles: FCEVs utilize hydrogen gas to produce electricity through a chemical reaction in fuel cells, powering an electric motor with zero tailpipe emissions. FCEVs offer high energy density and long-range capabilities, along with rapid refueling similar to conventional vehicles. However, their adoption is hindered by the limited availability of hydrogen refueling infrastructure and the high initial acquisition cost. Notable examples include the Toyota Mirai, Honda Clarity, and Hyundai Tucson Fuel Cell.
- Plug-in hybrid electric vehicles: These vehicles have both an electric motor and a gasoline engine. They can be charged by plugging them into an electric power source, and they can also run on gasoline when the battery is depleted. PHEVs have lower emissions than conventional gasoline vehicles, but they are not as clean as BEVs [8]. However, PHEVs also face challenges such as high initial vehicle costs due to high battery costs, limited

driving ranges caused by low battery energy density, and a lack of recharge infrastructure [19].

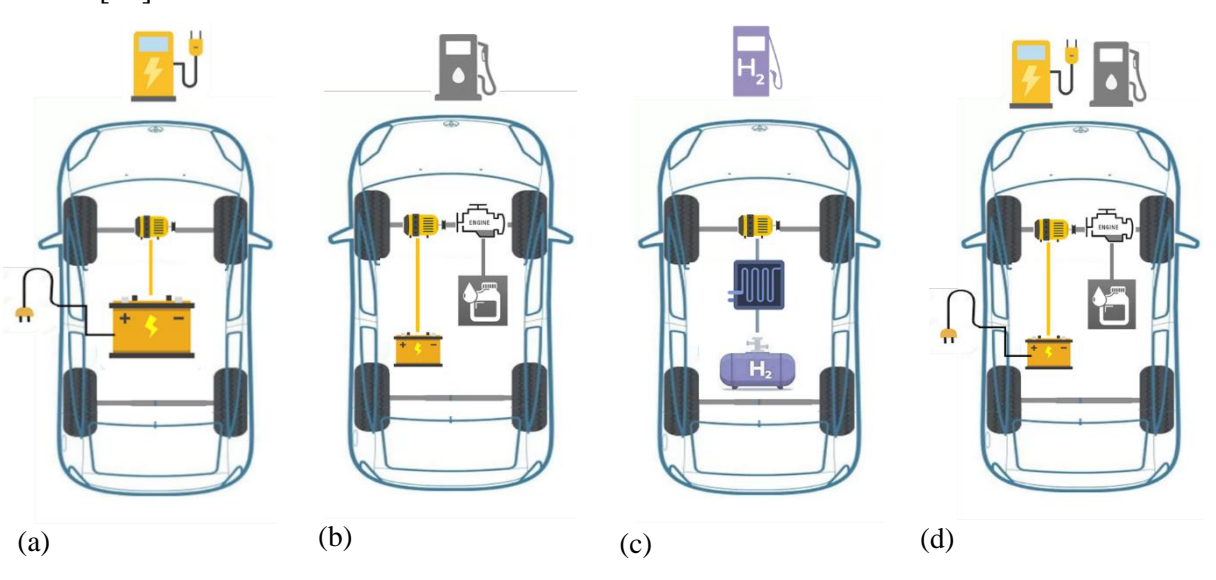


Fig 2.3: Types of Electric Vehicles: (a) Battery Electric Vehicles; (b) Hybrid Electric Vehicles; (c) Fuel Cell Electric Vehicles; (d) Plug-in hybrid electric vehicles.

2.2.4. The Multifaceted Dynamics of Electric Vehicle Adoption [20]

EV adoption is influenced by a spectrum of interconnected factors across political, economic, social, technological, legal, and environmental dimensions. Politically, governments implement measures such as purchase subsidies, tax reductions, and investments in charging infrastructure to stimulate EV uptake. These policies not only make EVs more financially viable but also signal a commitment to sustainability. Furthermore, information campaigns and green certifications raise awareness and promote eco-conscious choices among consumers. Economically, the attractiveness of EVs lies in their lower long-term costs, including reduced maintenance and operation expenses, coupled with potential future discounts due to anticipated depreciation rates. Sociodemographic factors, including social status, peer influence, and individual attitudes towards environmental concerns and new technologies, significantly impact adoption rates. Personal experiences with EVs and daily travel patterns also shape preferences.

Technologically, the availability and speed of charging infrastructure, along with factors such as vehicle range and smart functionalities like vehicle-to-grid connectivity, determine the practicality and convenience of EV ownership. Legal frameworks play a critical role in ensuring equitable

access to EVs, mandating charging infrastructure in new developments, and imposing restrictions on traditional car ownership or usage to incentivize electric alternatives. Moreover, the environmental benefits of EVs, including reduced greenhouse gas emissions and local air pollutants, are driving factors in their adoption. Effective recycling programs for lithium-ion batteries are essential for minimizing environmental impact and ensuring the sustainability of EVs throughout their lifecycle.

2.3. Energy sources in Electric Vehicles

In the context of vehicle hybridization, HESS must be used. It is composed of at least two energy sources. The advantage of hybridizing different storage elements is to take advantage of their complementarity in these properties. The main features that should be offered in the ESS are energy density, power density, lifespan, cost, and maintenance-free. Different types of energy storage devices are used in electric vehicles, such as batteries, supercapacitors, flywheels, and fuel cells.

2.3.1. Batteries

2.3.1.1 Choice of storage technology

Battery storage technologies are broadly categorized into three generations. The traditional generation, including lead-acid and Ni-based batteries, which predates the Lithium era, they both well-established and dominant before the advent of lithium-based technologies. Lead-acid batteries, originating in 1859, are renowned for their maturity and low cost, utilizing lead and lead dioxide electrodes with sulfuric acid electrolyte.

Similarly, nickel-based batteries, introduced in 1899, offer superior electrochemical properties but at a higher cost. Despite advancements like the nickel-metal-hydride (Ni-MH) battery, with better performance and environmental friendliness, both traditional battery types face limitations such as low energy density and lifespan. The current generation, dominated by Li-based batteries, has already outpaced the traditional one in terms of key qualitative indicators, especially the High storage density as shown in Fig 2.4, where Li-ion batteries have a high energy density, allowing them to store a large amount of energy in a compact size. This makes them suitable for use in electric vehicles, where space is limited[21]. Lithium-ion batteries (Li-ion) are particularly prominent, with variations like lithium-ion polymer batteries (Li-poly) offering higher specific

energy. Additionally, lithium-metal batteries present exciting possibilities for the future, albeit with challenges related to rechargeability.

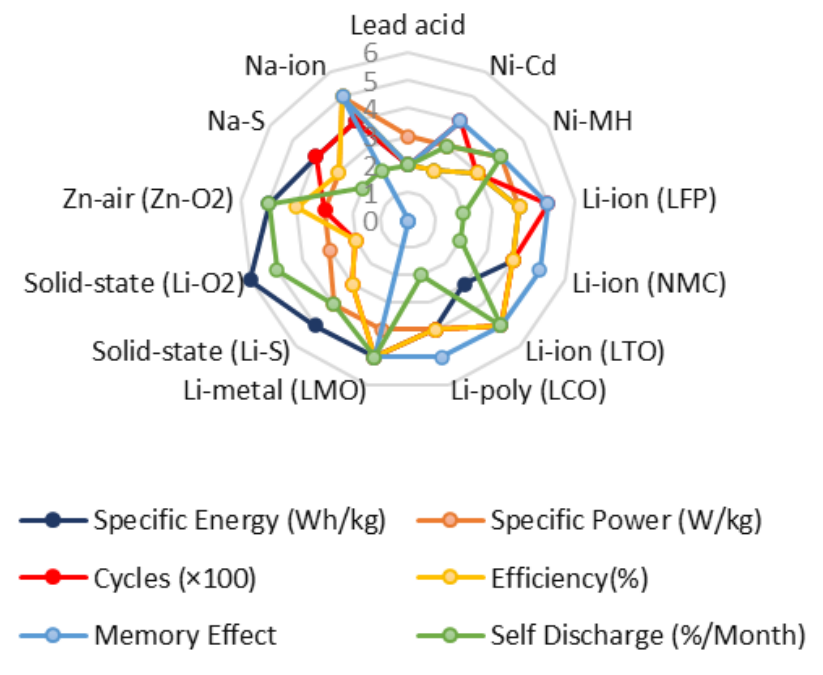


Fig 2.4: The qualitative indicators of batteries

Looking ahead to the future generation, diverse technologies such as sodium-beta, metal-ion, and metal-air batteries promise advancements in energy density, environmental sustainability, and cost-effectiveness. Among these, sodium-beta batteries stand out for their abundance and potential in stationary applications, while metal-air batteries offer exceptionally high theoretical energy densities, positioning them as prime candidates for electrified automobiles. Solid-state batteries, especially those based on lithium-sulfur chemistry, hold promise for overcoming existing challenges and ushering in a new era of high-performance energy storage for automotive applications. Fig 2.5 illustrates the graphical classification and generational evolution of battery types for EVs and portable applications [22].

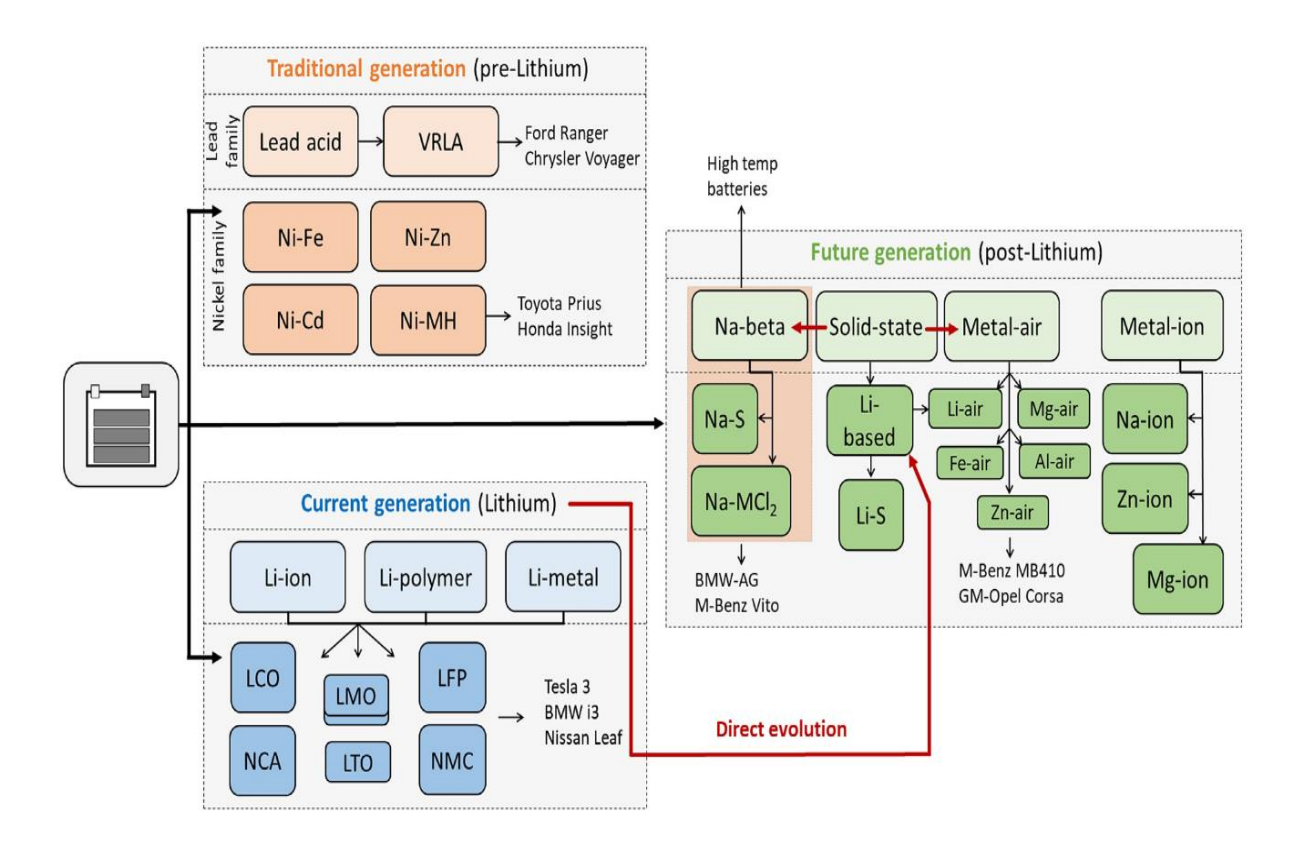


Fig 2.5: Evolution of Batteries for EV use across Generations

2.3.1.2 Battery price

The advancement of lithium-ion battery energy storage technology played a pivotal role in the mass marketing of EVs. Estimates have shown that global lithium-ion battery demand will rise over fivefold to 2000 gigawatt hours (GWh) between 2022 and 2030 as appears in Fig 2.6. The largest market for lithium-ion batteries is and will remain diverse EV application scenarios [23].

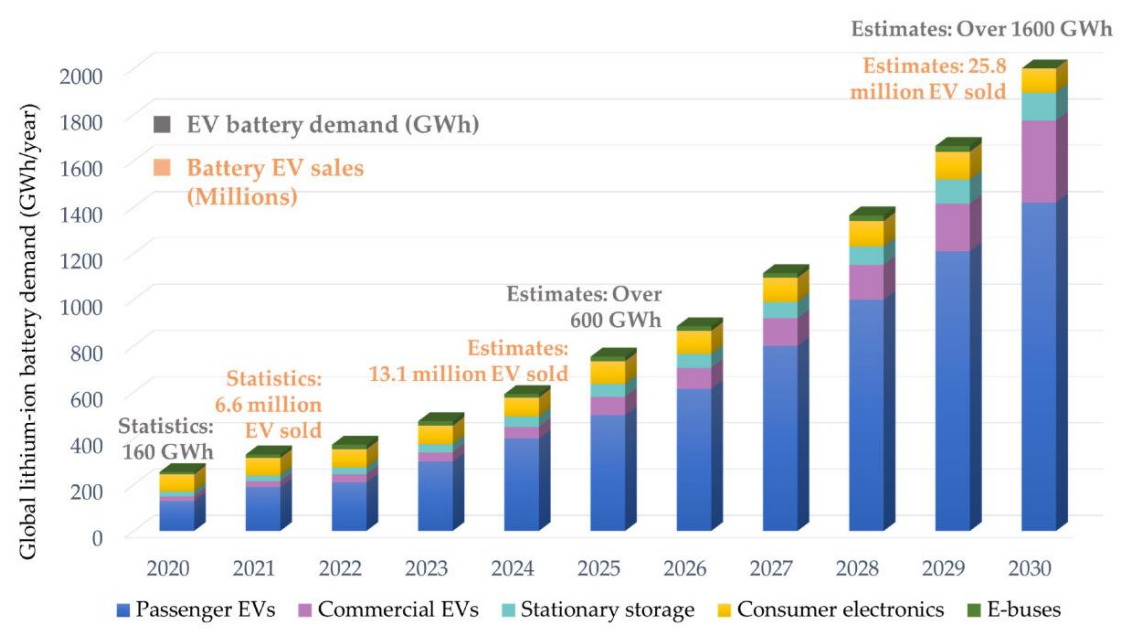


Fig 2.6: Global lithium-ion battery demand 2022-2030.

The battery pack is the most vital and most expensive component of an EV, constituting a significant portion, roughly 25%–50%, of their overall acquisition cost. Choosing the right battery technology for an EV is paramount, as it directly impacts various crucial factors such as cost, weight, capacity, efficiency, durability, and overall performance [18]. For instance, when the

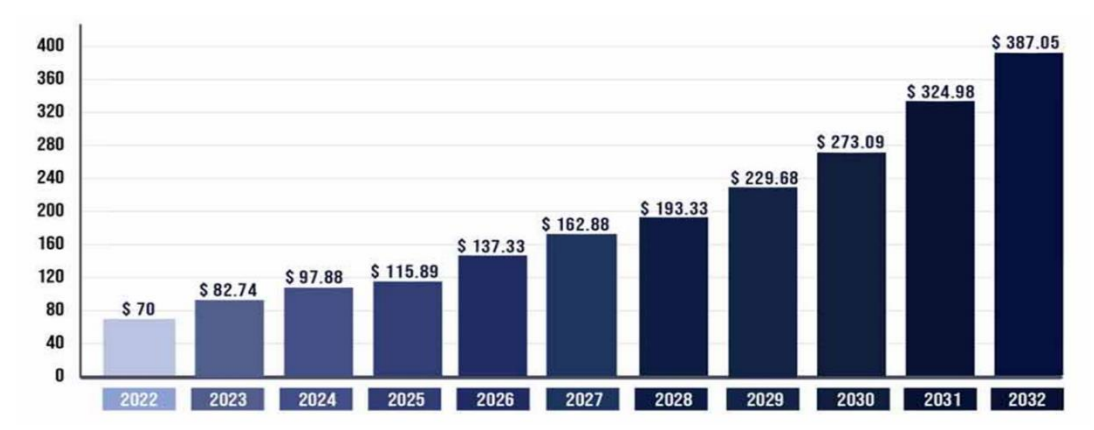


Fig 2.7: Lithium-ion Battery Market Size 2022 to 2032[24].

Nissan LEAF was introduced, its lithium-ion batteries accounted for approximately one-third of the vehicle's total cost. Over time, advancements in battery technology have led to a decline in battery prices. For instance, by the end of 2014, the cost per kilowatt-hour (kWh) had dropped to around \$500 from its 2009 price, and now it's anticipated to reach approximately \$100 by 2025,

indicating a significant downward trend. Tesla Motors' initiative to establish a "Mega factory" aimed at reducing manufacturing costs and increasing battery output further underscores this trend towards more affordable batteries [9]. As battery costs decrease, the price of EVs is expected to follow suit, enhancing their competitiveness against traditional combustion engine vehicles. This trend is supported by the expanding market opportunities for lithium-ion batteries, where the global lithium-ion battery market size, estimated at USD 70 billion in 2022, is expected to exceed USD 387.05 billion by 2032, showcasing a robust CAGR of 18.7% from 2022 to 2032 as shown in Fig 2.7. These projections are bolstered by advancements in battery technology, which have seen substantial increases in specific energy and energy density. For instance, from 2010 to 2020, specific energy rose from nearly 110 Wh/kg to 250 Wh/kg, with expectations of reaching up to 450 Wh/kg by 2030. Similarly, energy density increased from 300 Wh/L to 550 Wh/L over the same period, with predictions indicating a potential increase to 1100 Wh/L by 2030 [5].

2.3.2. Supercapacitor

ESS can be categorized based on their power and energy density. Batteries typically exhibit relatively high specific energy, while SCs demonstrate lower specific energy but substantially higher power density, as depicted in Fig 2.8. Which provides a concise comparison between batteries and SCs [25]. The superior power density of SCs enables them to deliver significantly higher power over shorter durations. This characteristic makes them well-suited for meeting the power demands of EV motors during urban driving scenarios characterized by frequent accelerations and decelerations, leading to large fluctuations in power requirements [26]. Moreover, supercapacitors are less susceptible to the effects of repeated deep charging and discharging, thus eliminating the need for regular replacement, unlike batteries. This feature also underscores their ecological friendliness, as they do not require frequent disposal. SCs can be rapidly recharged within seconds following deep discharge[27], with their internal resistance remaining almost constant throughout charging and discharging processes, and boasting a high cycle life [28]. Consequently, they find ideal applications in regenerative braking systems. While SCs cannot entirely supplant batteries, they can complement each other, enhancing the performance of the EV energy management system and reducing operational costs by mitigating the degradation of the EV battery and consequently decreasing the frequency of battery replacements.

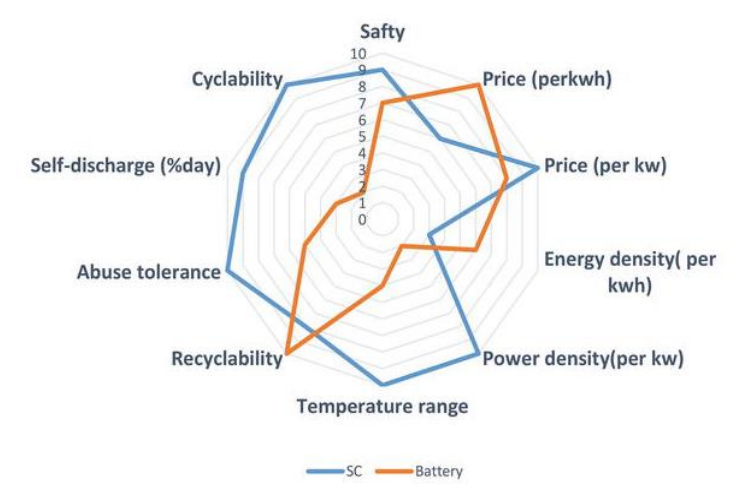
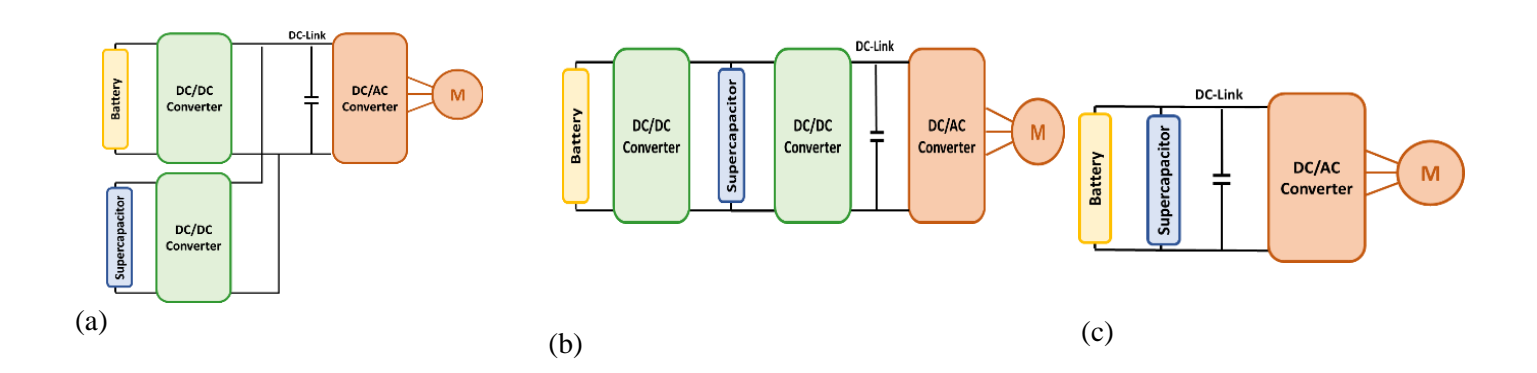


Fig 2.8: Comparison between batteries and supercapacitor.

2.4.1. Topologies

Investigating topology, control strategies, and optimal configurations for HESSs has consistently been a focal point in research. Various topologies are devised to harness the potential of both supercapacitors and batteries, ranging from passive and semi-active HESS configurations to full-active ones. Although these configurations entail increased complexity and cost, they offer enhanced operational flexibility and management capabilities. Fig 2.9 illustrates different hybrid topology approaches integrating battery and SC sources. More comprehensive insights into HESS for EV applications are encapsulated in Table 1 [29],[30], [31],[32],[33],[5].



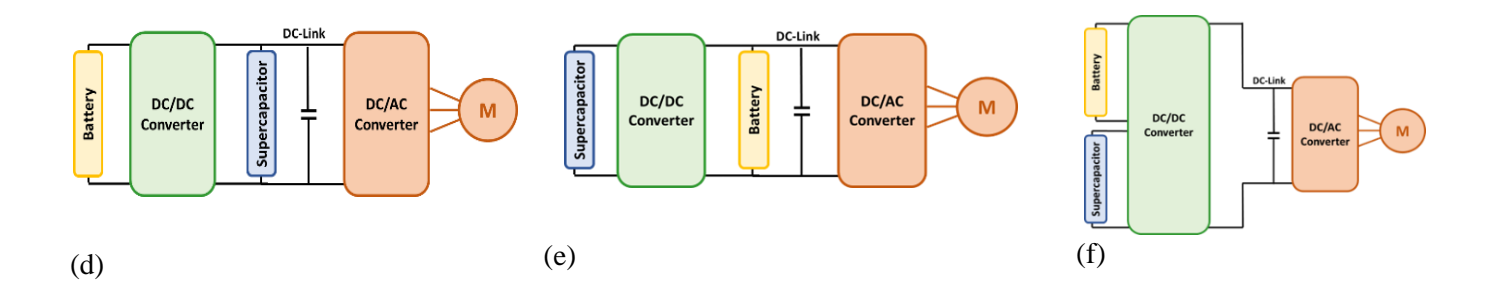


Fig 2.9: Topologies of HESSs integrating battery and SC sources: (a) Fully active topology with a parallel structure; (b) Fully active topology with a series structure; (c) Passive topology; (d) Battery semi-active topology; (e) Supercapacitor semi-active topology; (f) Multi-input converter topology.

Table 1: Comparative Analysis of Hybrid Energy Storage System Topologies

Topology	Types	Description	Advantages	Disadvantages
Active	Parallel, Serie (cascade)	In the parallel architecture, the ESS is connected parallelly to the DC bus through the use of two bidirectional DC-DC power converters. On the other hand, within the series architecture, these bidirectional DC-DC power converters link the ESS elements in series to the DC buss	 Parallel architecture eliminates ultracapacitor voltage fluctuations, making it highly favorable. Parallel architecture achieves steady battery current flow and voltage differences between load and battery. Series architecture isolates high power and energy storage from the DC bus. Enhanced energy management capabilities. Ensures optimal control for improved system efficiency. 	 High costs associated with implementation. Complex real-time interaction control required. In the case of a failure in any converter within the Series architecture, it will lead to a breakdown in the HESS
Passive		This topology directly connects the battery and SC to the DC bus, requiring no control for energy power-sharing.	 Simplicity in design Simplicity, cost- effectiveness, and reduced weight Provides high reliability Allows for direct integration of battery and SC Power power-sharing ratio depends on internal resistance, 	 Lack of controllability results in variable power-sharing dependent on source impedance, leading to susceptibility to cascading failures during emergencies. Limited utilization of SC due to uncontrollable power flow and lack of protection against faults.

Semi- active	Supercapac itor semi- active, Battery semi-active	This topology utilizes a single DC-DC converter connected to one of the individual ESSs, while the other ESS is directly connected to the DC bus.	offering simplicity in implementation - Reduced system cost and complexity - Most control strategies can be applied - Good trade-off between cost, weight, and control complexity - Adequate performance in meeting load requirements	 During regenerative braking, high current peaks may impact battery lifespan and efficiency Fluctuating DC bus voltage due to supercapacitor connection. Limited operating range of the supercapacitor in certain configurations. Cost and space requirements for the additional converter. Connecting the battery directly to
Multiple		This topology works	- It allows for bidirectional	the DC bus makes it susceptible to transient fluctuations - The complexity of the control
input converter		by integrating multiple ESSs into a single converter connected to a DC bus	power flow, enabling energy transfer between the battery and the output loads in both charging and discharging modes. - It mitigates voltage stress on semiconductors, resulting in decreased losses on switches	structure -Difficult in implementation

2.4. Energy Management Strategies

Developing an energy management strategy requires identifying the optimal power distribution between the two sources while accounting for their operational constraints, including storage capacities and frequency domain requirements. This distribution process must also address various performance factors, such as source longevity, driving comfort, autonomy, and other relevant considerations, as emphasized in the reference[34]. These energy management strategies are categorized into three main categories: rule-based, optimization-based, and learning-based strategy, as illustrated in Fig. 2.10.

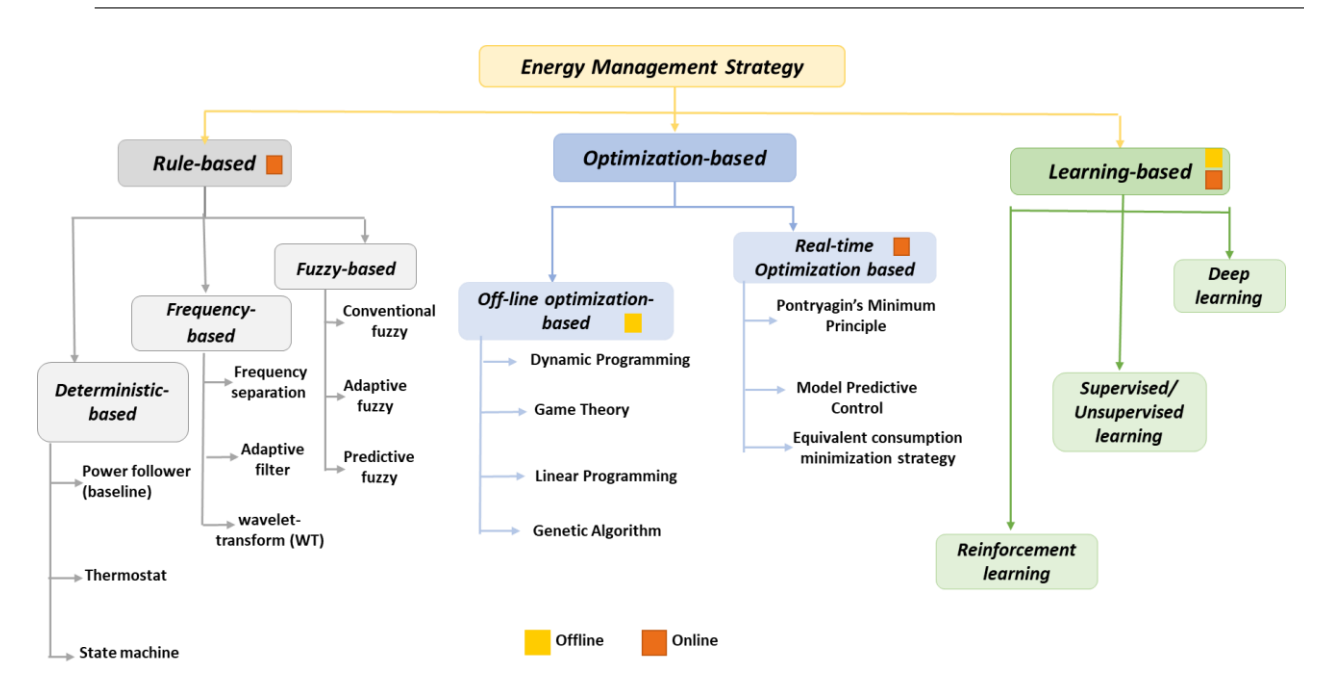


Fig 2.10: Classification of energy management strategies for hybrid electric vehicle.

2.4.1. Rule-Based Energy Management Strategies

This type of strategy is characterized by its simplicity and ease of real-time implementation. It typically operates based on a predefined set of rules that govern energy management according to the EV's current operating conditions. Typically, these regulations are enforced by employing either a lookup table or conditional expressions based on if-then rules. Nevertheless, its primary drawback lies in its inability to adapt to changing driving conditions over time, which arises from a deficiency in prior knowledge of driving information[35]. These strategies are computationally efficient and can be categorized into deterministic rule-based, frequency-based, fuzzy logic-based.

2.4.1.1. Deterministic rule-based:

A deterministic rule-based approach for EVs operates through predefined conditions and thresholds to regulate power distribution, thereby optimizing energy management. This method is favored for its straightforward implementation, reliability, and minimal computational overhead [36]. It effectively directs power within the vehicle's electrical system, ensuring safety functions and preventing voltage drops below critical levels[37]. Additionally, such strategies can curtail power consumption from comfort features, thus optimizing electrical energy utilization [38].

However, deterministic rule-based strategies have their limitations. They may not match the efficiency of other approaches, like deep reinforcement learning, in maximizing fuel-saving performance or profit [39] [40]. They might struggle to adapt to varying states of charge and battery capacities, thus hindering their integration with plug-in electric vehicles in power distribution networks.

Numerous studies have delved into deterministic rule-based strategies for EVs. For instance, Huang, Nguyen, and Chen devised a rule-based control strategy for a parallel HEV to enhance energy efficiency and mitigate carbon emissions. This strategy utilized the driver's power demands as input and determined power distribution among the generator, electric motor, and internal combustion engine based on predefined rules. Evaluation on the NEDC2000 driving cycle revealed significantly improved fuel efficiency in HEVs compared to ICE vehicles [37] . Shi, Guo, Liu, Cai, and Wang proposed an enhanced rule-based strategy by incorporating a reference SOC curve and SOC adaptive adjustment [41]. This ensured a linear decrease in state of charge with driving distance, reaching a minimum at the end of journey, akin to dynamic programming results. The improved rule-based strategy demonstrated a 7.87% reduction in fuel consumption compared to conventional rule-based approaches.

2.4.1.2. Frequency-based

EMSs based on frequency utilize the frequency attributes of power loads and energy sources to optimize energy distribution and usage. By scrutinizing the frequency components of power loads, advantageous frequency ranges conducive to efficient operation are pinpointed. This data is subsequently employed to distribute energy resources and enact customized control measures tailored to the specific frequency needs of the load. This approach results in minimized energy wastage and heightened overall efficiency. In this context, researchers have explored a variety of approaches. In [42], the authors introduce a frequency-based power-sharing technique utilizing a frequency splitter to direct low-frequency power demand to the battery and high-frequency demand to the SC. Their findings indicate that this method effectively reduces battery current and enhances battery lifespan. However, the predetermined threshold for frequency separation may not always optimize real-time power sharing because of variations in demanded power behavior across driving conditions. Therefore, [43] proposes an EMS that utilizes a variable bandwidth filter combined with sliding mode control for managing hybrid energy storage systems comprising

batteries and ultracapacitors as shown in Fig 2.11. Results demonstrate the system's ability to maintain battery soc within desired limits while ensuring stable ultracapacitor operation.

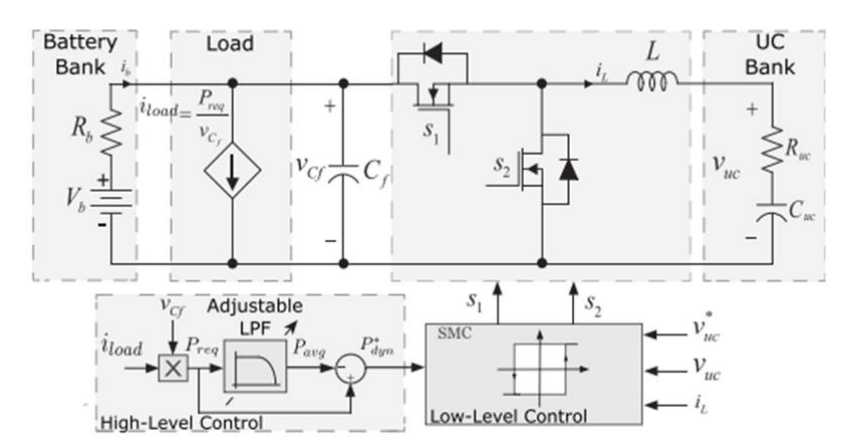


Fig 2.11: Electrical diagram of a Battery/Ultracapacitor EMS utilizing an Adjustable Bandwidth Filter and Sliding-Mode Control

On another front, WT has emerged as a formidable contender in frequency-based EMSs. In [44], the authors present a real-time energy management strategy for hybrid battery and supercapacitor ESSs that combines WT, neural networks, and FL as illustrated in Fig 2.12. The approach forecasts low-frequency power demand with neural networks, allocates high-frequency demand to the supercapacitor, and regulates supercapacitor voltage using FL. Outcomes showcase significant reductions in peak power supplied by the fuel cell and effective utilization of the supercapacitor and battery for energy management. The adaptability of wavelets enables superior signal analysis, enhancing the accuracy of EMSs.

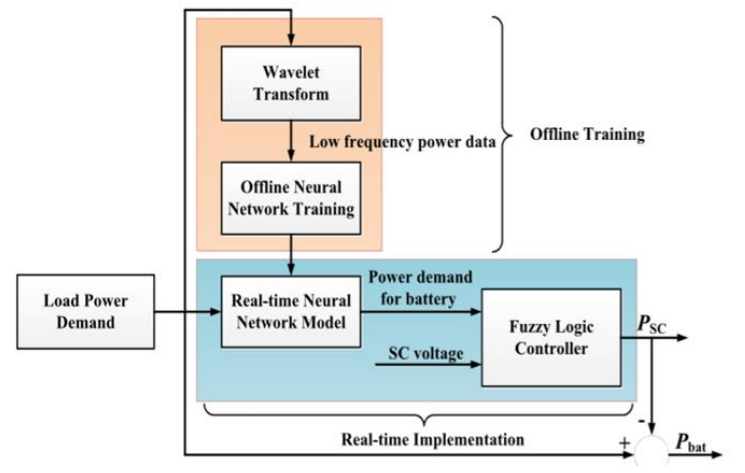


Fig 2.12: Detailed control framework of hybrid energy storage system in this study

2.4.1.3. Fuzzy based

The fuzzy-rule-based energy management control strategy, an extension of deterministic rulebased energy management control, operates by formulating a set of fuzzy rules (IF-THEN) derived from human knowledge and cognition, eliminating the need for a mathematical system model [45]. This approach offers numerous advantages, including robustness, ease of implementation and tuning, real-time control capability, sufficient human reasoning capacity, rapid calculation speed, and suitability for online use in embedded systems. However, conventional methods may lack adaptability due to challenges in selecting suitable membership functions for various inputs [35]. In [46], an energy management system was introduced for a hybrid energy storage system in an electric vehicle, integrating a rule-based fuzzy logic controller with power filtering. The results showed optimal energy distribution between the dual energy sources of the HESS model. Additionally, the analysis indicated lower voltage demand frequency for the battery compared to the SCs, leading to reduced battery degradation. In [47], the authors propose a hierarchical energy management strategy for fuel-cell hybrid electric vehicles, The HEMS optimizes power distribution among fuel cells, batteries, and ultracapacitors to enhance fuel economy. Energy storage systems simplify distribution, while fuzzy logic controllers efficiently distribute power. A status regulation module improves fuel cell life and battery state of charge. An adaptive low-pass filter maximizes ultracapacitor utilization as shown in Fig 2.13 Comparative simulations show reduced hydrogen consumption and enhanced vehicle energy efficiency under various cycle conditions, demonstrating the economic and dynamic benefits of the strategy.

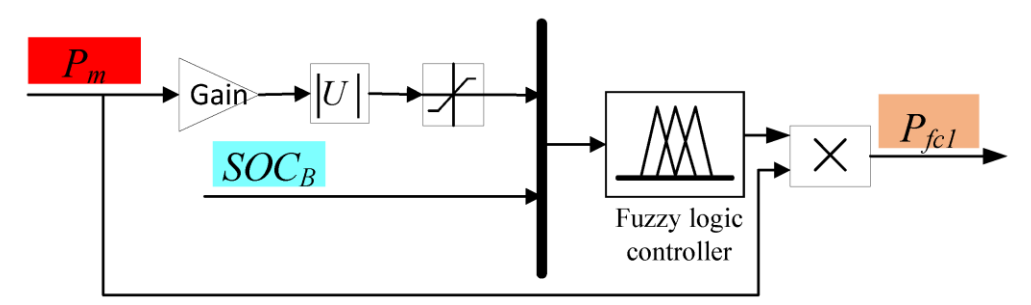


Fig 2.13: The model diagram of the fuzzy control module

2.4.2. Optimization-based

Optimization-based strategies use mathematical models and algorithms to determine the optimal energy management solution. They may consider driving cycle, battery characteristics, and environmental conditions. However, these methods demand significant computational resources and may necessitate high-performance hardware, leading to increased system cost and complexity. Optimization-based approaches can be categorized as either offline or real-time optimization.

2.4.2.1. Offline optimization-based

Global optimization-based strategies aim to find the optimal energy management strategy that minimizes energy consumption or maximizes the driving range of the electric vehicle over a longtime horizon. These strategies typically require the use of complex optimization algorithms and may take a longer computational time [48]. Dynamic Programming is proposed as a solution for tackling optimal control problems within nonlinear systems, dynamic programming stands out as a prominent mathematical technique derived from Bellman's optimality principle. Essentially, DP endeavors to simplify intricate multi-stage decision-making into a series of single-stage decisions, thus breaking down the problem into manageable sub-problems that can be addressed sequentially. However, when dealing with excessively large dimensions, the computational and analytical processes may face significant hindrances [49], [50]. In [51], the authors present a dynamic programming-based energy management strategy for fuel cell hybrid electric vehicles, which notably enhances fuel economy and system durability. Simulation results show a 6.46% reduction in hydrogen consumption per 100 km compared to previous methods. Additionally, by regulating power output changes, the strategy reduces large load fluctuations, demonstrating its advantages over alternative approaches. Game theory finds extensive application in addressing multi-objective optimization challenges by incorporating both anticipated and actual human behaviors. Employing a multi-agent game model to simulate the actions of diverse energy sources in HEVs aids in establishing a balanced power distribution. Compared to alternative methods, game theory's mathematical computations are less intricate. However, due to its dependence on human behavior predictions and the complexity of advanced powertrain models, its solution is less tied to specific drive cycles but may be less compatible with vehicular control techniques [52]. Q. Zhang and G. Li [53] employ game theory-based control to manage power flow in the FC + B configuration, tackling uncertainties in energy demand during driving cycles. This approach, combined with

fuzzy logic correction, effectively reduces fuel consumption and mitigates battery degradation. However, its applicability is limited to specific hybridization configurations due to the need for a deep understanding of each control method.

Genetic Algorithm (GA) is a metaheuristic approach inspired by the principles of evolution. It begins by generating an initial population of solutions (chromosomes), which are then evaluated using an objective fitness function. The best solutions typically require more time to evolve and develop, Fig 2.14 illustrates the flow chart of the GA [54],[55]. Genetic algorithms have found widespread application in devising energy management strategies for electric vehicles. These algorithms are instrumental in determining the optimal battery charge/discharge protocol in fuel cell hybrid electric vehicles, considering factors like minimizing hydrogen consumption rate, preserving battery charge rate, and maximizing fuel cell efficiency [56]. Moreover, genetic algorithms play a crucial role in the energy management control schemes for hybrid energy storage systems in EVs, which integrate photovoltaic, battery, and ultracapacitor systems. These algorithms contribute to efficient energy utilization, prolonging battery lifespan, and enhancing overall performance [57].

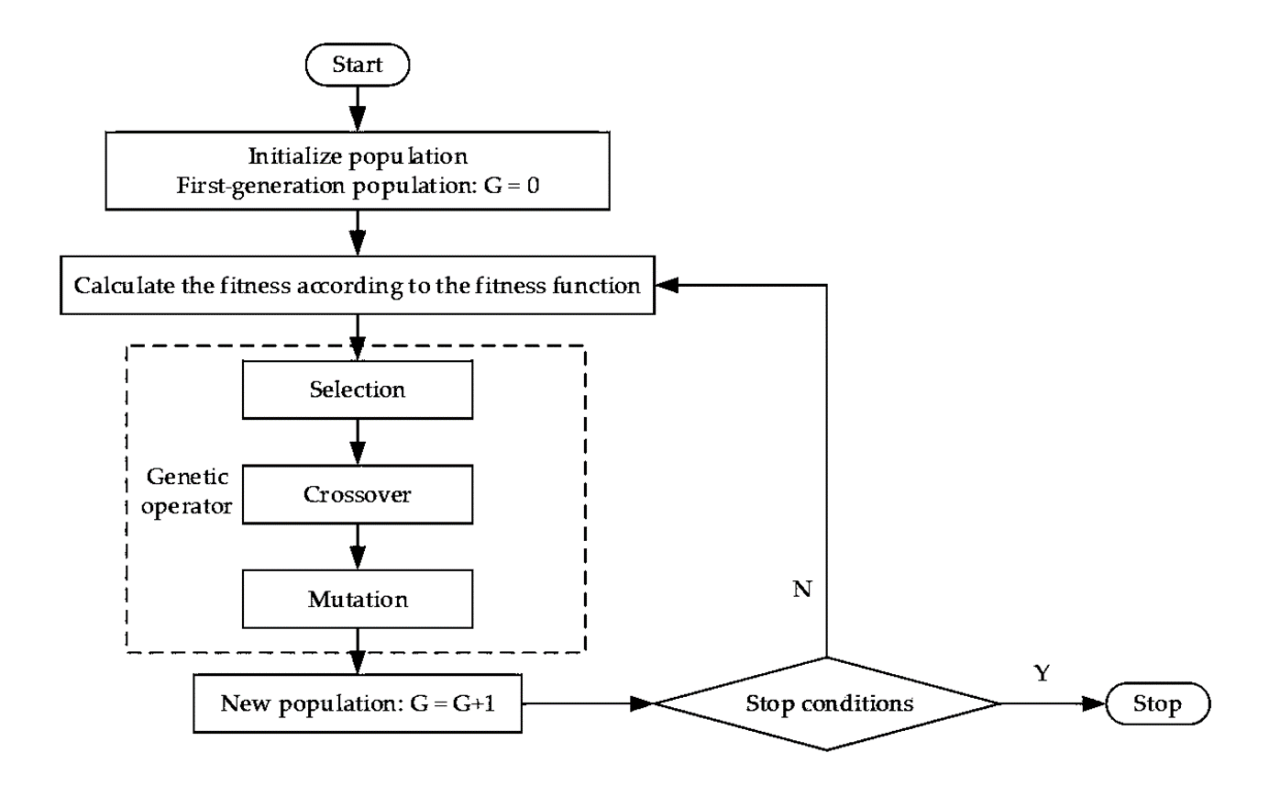


Fig 2.14: Flow chart of Genetic Algorithm

2.4.2.2. Real-time optimization

Real-time optimization aims to find an optimal energy management strategy for a specific driving cycle or specific operating conditions. These strategies are typically less intensive in terms of computational time and can be computed in real-time. A combination of both global and local optimal strategies may be used to balance the need of accuracy and computational efficiency [48].

The Pontryagin's Minimum Principle (PMP) serves as a fundamental mathematical tool within control systems for devising optimal control strategies. It entails establishing the requisite conditions for minimizing costs in optimization dilemmas. Assuming determinism in the trajectory computed via PMP and adherence to relevant constraints and boundaries, the resulting optimal trajectory is commonly regarded as globally optimal. Consequently, the Hamiltonian function can be formulated:

$$H(x(t), u(t), t) = m_f(x(t), u(t), t + \lambda(t) f(x(t), u(t), t)$$
(2.1)

with $\lambda(t)$ representing the co-state. Both the system's state and co-state must conform to the stipulated following conditions:[49]

$$\frac{\partial H}{\partial u} = 0 \tag{2.2}$$

$$\dot{\lambda}(t) = -\frac{\partial H}{\partial x} = -\lambda(t)\frac{\partial f}{\partial x} \tag{2.3}$$

Pontryagin's Minimum Principle (PMP) is employed in various energy management techniques for electric vehicles. An A-ECMS-based EMS for extended-range electric vehicles integrates PMP into its design, resulting in fuel consumption savings of 6.2% and 3.4% when compared to traditional strategies[58]. Similarly, a real-time adaptive EMS for vehicles equipped with hybrid energy storage systems (HESSs) utilizes PMP to minimize total electricity costs, leading to reductions in battery losses by 18.41%, 13.94%, and 20.37% [59].

MPC, an advanced control method, utilizes a model to predict future system behavior and determines optimal outputs by solving constrained optimization problems. It directly considers constraints and aims to track a predefined reference within a specified horizon (Fig 2.15). Only the initial output value from the optimized trajectory is implemented at each step [60] .A study implemented Model Predictive Control to enhance the energy efficiency of EVs by optimizing

their thermal management systems within power and thermal. This involved a control-oriented model that captured the dynamics of the EV's powertrain and thermal subsystems. Through sensitivity analysis, the study identified key traffic and speed variables influencing optimal EV performance and assessed the impact of predictive uncertainties [61]. Additionally, another study introduced a scenario-based MPC framework for Plug-In Hybrid Electric Vehicles (PHEVs), achieving comparable fuel consumption reductions to nominal MPC without full foresight of future driver behavior [62].

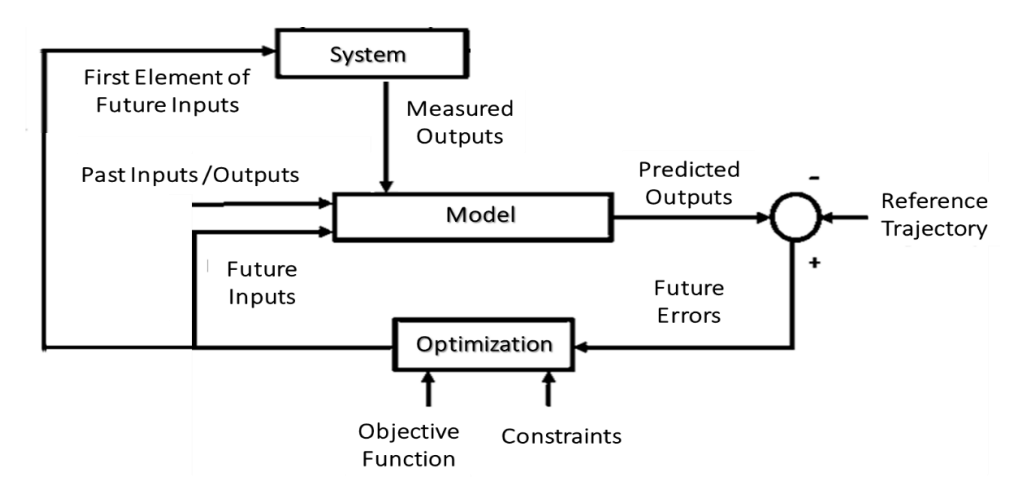


Fig 2.15: Model predictive control block diagram

The ECMS utilizes an optimization algorithm to dynamically compute the most efficient power distribution between the internal combustion engine and electric motor, taking into account present driving conditions and energy storage system status. This enables the vehicle to minimize fuel consumption, fulfill driver power requirements, and preserve the energy storage system's charge level. In [63] the authors proposed the environmental perceiver-based equivalent consumption minimization strategy (EP-ECMS) for parallel plug-in hybrid vehicles. It employs a precise environmental perceiver based on GCN and an attention mechanism for traffic state recognition. Furthermore, the Harris Hawk optimization algorithm determines the optimal factor offline. Simulation results demonstrate a notable 7.25% energy consumption improvement compared to the traditional ECMS.

2.4.3. Learning-Based Energy Management Strategies

Researchers have been exploring novel paradigms in pursuit of more adaptable and robust EMS solutions. Recently, machine learning has emerged as a promising alternative that employs software applications to enhance outcome predictions with increased accuracy, avoiding the necessity for explicit programming. ML algorithms utilize past data to anticipate new output data. There are three categories of ML methods based on what data types need to be predicted. These categories include reinforcement learning supervised/unsupervised learning, and Neural network learning [64].

Supervised learning trains a model using labeled data to predict outcomes. It utilizes labeled data pairs of input and correct output attached to it to teach the machine, acting as a guide for prediction[65]. supervised learning has been extensively utilized in HEV energy management for tasks like battery degradation mitigation, hierarchical energy management, and online control strategy development. In [66], a two-stage method is proposed. Firstly, a battery aging state calibration model is established using a semi-empirical method, followed by linearizing the mapping between aging features and battery life loss with a supervised learning method. Secondly, a neural hybrid optimization-based energy management method is employed to mitigate vehicle battery aging costs by simplifying model solving and reducing computation cost.

Contrary, in unsupervised learning, the data provided to learning algorithms consists solely of input values without any associated output labels. This means there is no predefined notion of what to predict. The primary goal of unsupervised learning is to uncover inherent structures within the input data. Algorithms in unsupervised learning can organize the available data in various manners. Unsupervised learning techniques could potentially be applied in HEV for tasks such as anomaly detection, clustering driving patterns, or identifying hidden patterns in vehicle data without the need for labeled information. In the study [67], the authors utilized the k-means clustering algorithm to classify derived profiles. They then devised a power distribution strategy, applying different co-state maps based on the classification of each driving profile

Reinforcement learning is a machine learning technique that involves training an agent to make decisions based on feedback from the environment [68]. Unlike supervised and unsupervised instructional methods, the RL approach iteratively enhances its understanding by incorporating feedback from previous experiences in a cycle. This prevents it from persisting indefinitely once

the model has been established through data gathered from trial and error attempts, a schematic of Reinforcement Learning is shown in Fig 2.16 [69]. Reinforcement learning has been utilized to improve energy management in hybrid electric vehicles by developing intelligent control strategies, In their study [70] by Yu Cheng, Ge Xu, and Qihong Chen, a Q-learning-based approach for dual-energy electric vehicle hybrid systems is proposed. It outperforms rule-based strategies, reducing losses and lithium battery current conversion rate by 0.43% and 35.17%, respectively. The effectiveness is demonstrated, updating control quantities through changes in the transition probability matrix under mixed working conditions

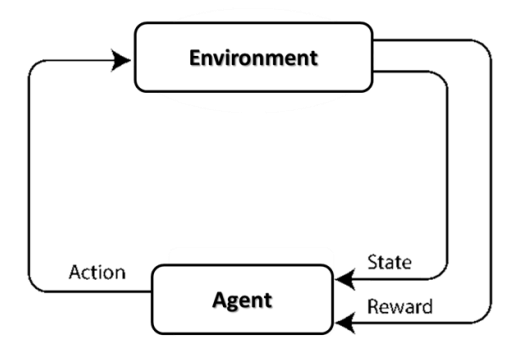


Fig 2.16. A schematic of Reinforcement Learning concept

2.5. Driving Pattern Recognition-Based Energy Management Strategies.

Energy Management Systems can make smart decisions regarding power distribution within HEVs. By optimizing the allocation of energy resources based on recognized driving patterns, artificial intelligence allows to examination of both historical data and real-time driver actions alongside road conditions. This enables Energy Management Systems to forecast energy requirements more accurately and fine-tune power distribution, ultimately enhancing the efficiency of HEVs.

Combining driving pattern recognition with optimization-based energy management strategies for electric vehicles has several potential benefits. It allows for real-time power allocation based on the driving patterns, resulting in improved system efficiency and energy loss reduction [71]. Additionally, the integration of predicted vehicle speed into the powertrain control strategy can lead to more optimal energy management and closer results to optimal than conventional strategies

[72]. Moreover, integrating driving behavior in energy management strategies can reduce fuel consumption and improve the lifespan of power sources [73].

Nevertheless, the complex merging of these techniques poses challenges, particularly due to the increased computational requirements. which could lead to system delays or bottlenecks in system performance. As a result, the system ability of the system to promptly respond and adapt to dynamic driving conditions might be compromised.

Fusing driving pattern recognition with rule-based energy management strategies is seen as a synergistic approach to enhance energy optimization in HEVs. Driving pattern recognition can dynamically modify the flexibility of different rules based on the recognition process results [11]. This resolves the constraints of traditional rule-based systems and improves entire vehicle performance and energy economy. Even so, much research hasn't been done on this strategy. In both [12] and [13], the authors present an energy management methodology for hybrid electric vehicles that incorporates driving pattern recognition alongside fuzzy logic control. Within the second strategy, labeled as 'NNF-EMS,' driving cycle recognition is merged with fuzzy logic control to adjust fuzzy controller parameters according to driving cycle characteristics, thereby improving fuel efficiency across scenarios

On the other hand, in [14], a flexible energy management system for electric vehicles is suggested, which combines driving cycle recognition with wavelet transform. Additionally, [15] presents a driving pattern recognition (DPR)-based intelligent energy management technique for a hybrid energy storage system (HESS) in electric cars. Simulations highlight its superiority over conventional methods, illustrating a 58.2% decrease in battery current, a 6.16% extension in battery lifespan, and an 11.06% enhancement in vehicle endurance

2.6.Conclusion

In response to the growing interest in electric vehicles, this chapter gives a detailed exploration of EVs. It delves into the intricate details of electric vehicle architecture, commonly utilized energy sources, and prevalent topological configurations. Then, a review of energy management techniques for hybrid systems has been briefly given. Knowledge of the principle of these strategies allows us to make well-reasoned choices regarding the strategy employed in this study.

Chapter 3

Modeling of hybrid energy storage systems and electric vehicles

3.1.Introduction

Modeling is crucial in understanding complex systems by providing a structured approach to analyze, manage, and improve them. As such, in this chapter, explicit models of the various subsystems are presented, together with the dimensioning of the constituent components. At the core of our discussion, the proposed hybrid system comprises three integral parts:

- an electrical power system: mainly consists of lithium-ion batteries as a primary source, supercapacitors as a secondary source, and two bidirectional DC/DC. These converters enable power flow in both directions, delivering energy from the sources to the load during discharge and returning energy from the load to the sources during charging.
- Driving system: contains Two DC motors which are individually controlled to emulate the traction side.
- DC link: serves as a centralized junction for all power connections, facilitating the interconnection between the electrical power system and the drive system. Its regulation around a reference value is imperative for ensuring smooth operation and optimal performance of the hybrid system.

3.2. Energy source modeling

3.2.2. Battery

A lithium-ion battery is an advanced battery technology that uses lithium ions as a key component of its electrochemistry. Li-ion battery consists of a positive electrode (cathode), a negative electrode (anode), an electrolyte, and two current collectors as shown in Fig 3.1. The cathode typically comprises lithium metal oxide, while the anode is commonly made of graphite or other carbon-based materials. The electrolyte in a Li-ion battery contains lithium salts and plays a crucial role in facilitating the movement of lithium ions between the cathode and anode during charge and discharge cycles[74]. During a discharge cycle in Li-ion batteries, lithium atoms in the anode undergo ionization, separating from their electrons. These lithium ions then traverse through the electrolyte towards the cathode, where they recombine with electrons to neutralize electrically. The small size of lithium ions enables their movement through a micro-permeable separator between the anode and cathode, facilitating high voltage and charge storage capabilities per unit mass and volume in Li-ion batteries[75].

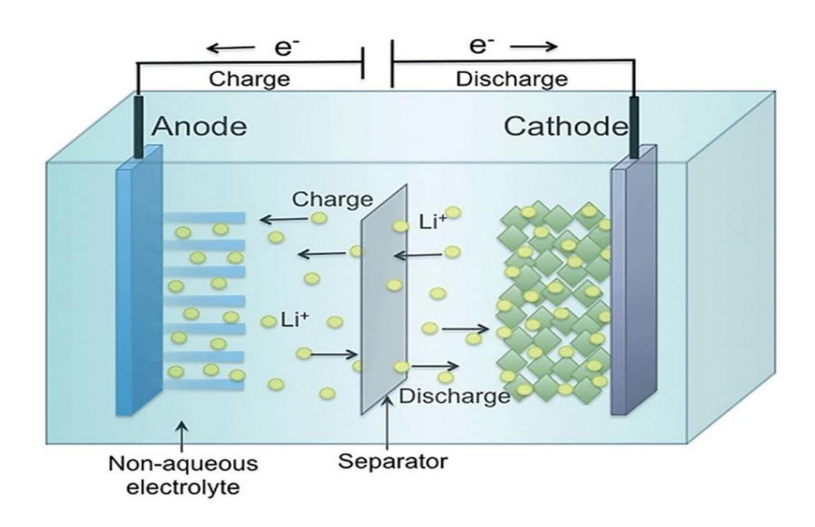


Fig 3.1: Schematics of Li-ion battery

Li-ion batteries can be categorized based on the electrode materials utilized, as detailed in Table 3.1:

Table 3.1: Li-ion battery types.

Type	LCO	LMO	NCA	NMC	LFP	LTO
Cathode	Lithium	Lithium	Lithium	Lithium	Lithium	Lithium
Material	cobalt	manganese	nickel cobalt	Nickel	Iron	manganese
	oxide	oxide	aluminium	Manganese	Phosphate	oxide
			oxide	Cobalt Oxide		
Anode	Graphite	Graphite	Graphite	Graphite	Graphite	Li-titanate
Material						

LiFePO4 batteries are set from other lithium batteries by their exceptional thermal stability and safety profile. Unlike conventional Li-ion batteries, which can undergo thermal runaway under certain conditions. Moreover, LiFePO4 batteries offer long life with minimal capacity degradation during repeated charge-discharge cycles, making them preferred for EVs [76]. The oxidation-reduction reaction of LiFePO4 batteries taking place at both the positive and negative electrodes is expressed as follows:

Cathode Reaction:

$$FePo_{A} + Li^{+} + e^{-} = LiFePo_{A} \tag{3.1}$$

Anode Reaction:

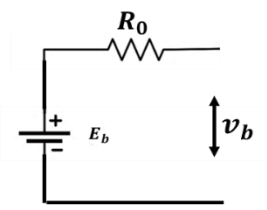
$$LiC_6 = C_6 + Li^+ + e^- (3.2)$$

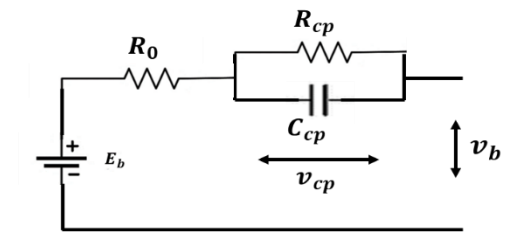
Overall Reaction:

$$C_6 + LiFePo_4 = LiC_6 + FePo_4 \tag{3.3}$$

Electrochemical models, illustrated in Fig. 3.2, provide a simple and widely used method to simulate battery dynamics without accounting for internal phenomena.

The Rint model is the most basic ECM, containing a voltage source in series with internal resistance. It accounts for ohmic resistance from contacts, electrodes, and electrolytes, offering a basic approximation of battery voltage behavior. By connecting a resistor and capacitor in parallel to the Rint model, the Thevenin model, also known as the 1 RC model, is created. This model represents ohmic losses and concentration polarizations. Increasing the number of RC networks can be included to enhance the model's complexity and accuracy. Therefore, the Partnership for a New Generation of Vehicles (PNGV) model, developed by the US Department of Energy for Power-Assist Hybrid Electric Vehicles, simulates battery voltage behavior using an internal resistance element, an RC element, and a series-connected capacitance, known as bulk capacitance, to calculate variation in open circuit voltage. The Dual Polarization (DP) model builds on the Thevenin model by introducing activation polarization with the addition of a second RC element. It captures the total internal resistance, encompassing ohmic resistance, including ohmic resistance, concentration polarization resistance, and activation polarization resistance. [77]





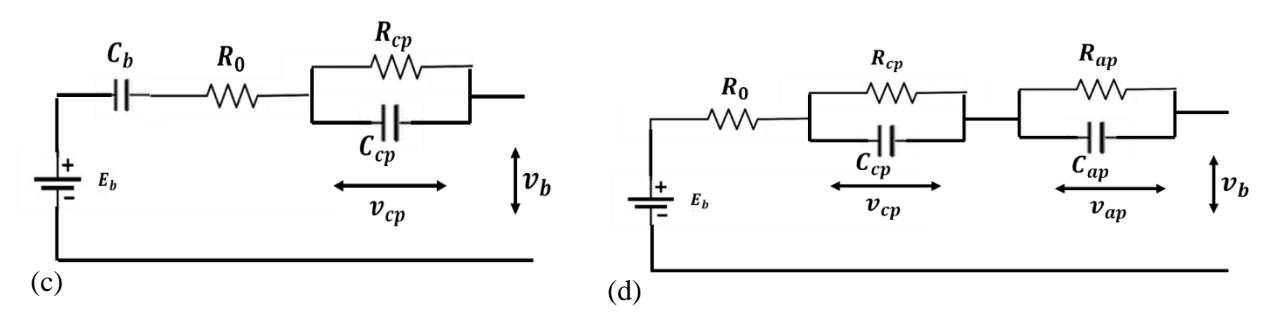


Fig 3.2. The equivalent models of Li-ion battery: (a) Rint model, (b)Thevenin model, (c) PNGV model, (d)DP model.

This work employs the first-order ECM as the circuit model for Li-ion batteries. This model was chosen to balance the ability to fit experimental data with the complexity of the equivalent circuit[78]. The equations for the model are as follows:

$$V_{b}(t) = E_{b}(t) - R_{0}(t) \times i_{b}(t) - V_{cp}$$
(3.4)

In addition to building an accurate battery model that involves constructing and parameterizing an equivalent circuit that captures the nonlinear characteristics of the battery, this model must account for dependencies on temperature, state of charge, and state of health. These dependencies are unique to the electrochemical characteristics of each cell and must be determined based on measurements of the battery cell [79].

Battery soc is typically defined as the remaining capacity of a battery compared to its total rated capacity under a specific discharge rate[80]. It can be expressed as:

$$soc = \frac{Q}{C_N} \times 100\% \tag{3.5}$$

Where Q is the current remaining battery capacity, and C_N is the rated battery capacity

The Coulomb counting method is utilized in this work as a straightforward approach for estimating the Soc. It is commonly used in online applications due to its simplicity and real-time capability, avoiding the complexity of EMS implementation proposed in subsequent chapters. This method involves calculating the extracted capacity of the cell by integrating the current over time, and it can be defined as follows:

$$soc(k+1) = soc(k) - \frac{\eta \Delta t}{C_N} i(k)$$
(3.6)

3.2.2. Supercapacitor

Supercapacitors are electrochemical capacitors with significantly higher energy density than traditional electrolytic capacitors, owing to the charge accumulation via electrostatic double-layer capacitance (EDLC) and electrochemical pseudocapacitance interactions. These interactions occur at the electrode/electrolyte interface, emphasizing the importance of a high specific surface area for enhanced charge storage. SC system consists of two electrodes (anode and cathode), an electrolyte, and a separator, with charge mainly stored at the electrode in the case of EDLC, where ions from the electrolyte are adsorbed at the interface. The separator serves as a semipermeable membrane, allowing ion transport while preventing short circuits. The electrode incorporates a current collector to ensure efficient electron transfer to external devices.[81].

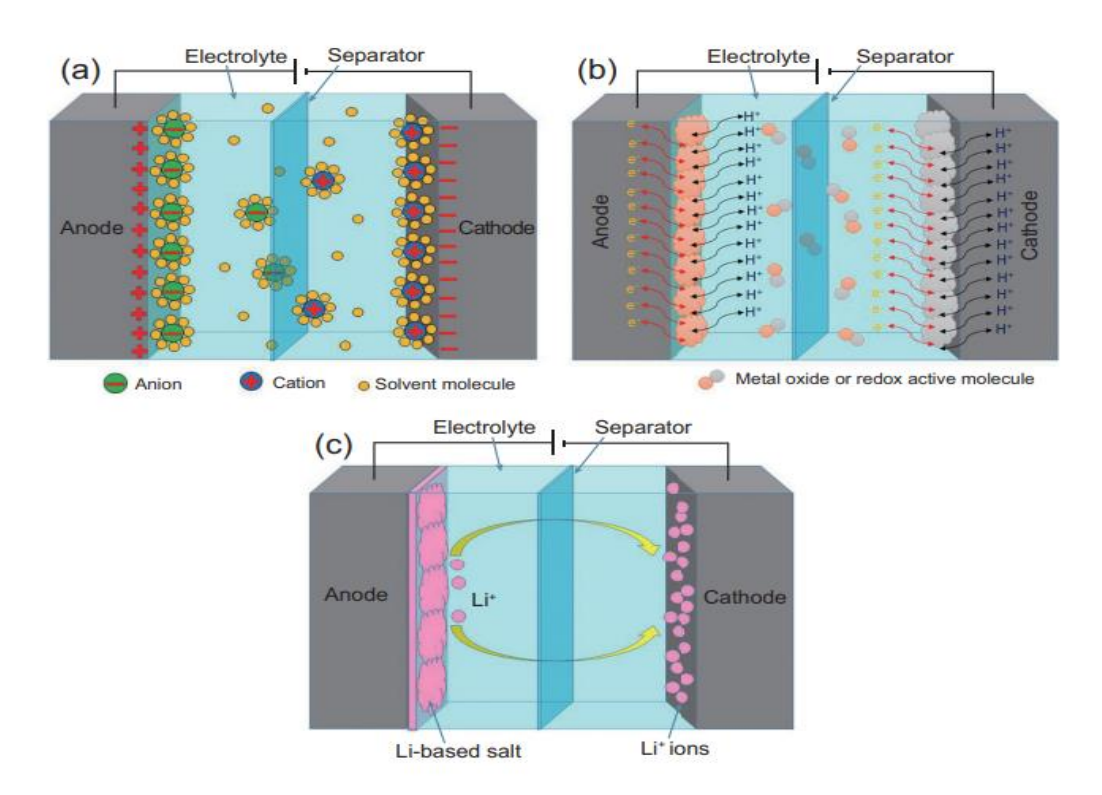


Fig 3.3: Schematic illustration of (a) electrical double-layer capacitor, (b)pseudocapacitor, (c)hybrid supercapacitor

Supercapacitors can be categorized into electric double-layer capacitors (Fig 3.3a) and pseudocapacitors (PCs) (Fig 3.3b) based on their energy storage mechanisms, with EDLCs storing charges at the electrolyte-electrode interfaces and PCs involving reversible Faradaic redox reactions. When a supercapacitor combines a capacitive carbon electrode with either a pseudocapacitive or lithium-insertion electrode, it transforms into a hybrid supercapacitor (HSC)(Fig 3.3c). HSCs offer a unique energy storage approach by leveraging the benefits of both EDLCs and PCs, providing high power densities from EDLCs and high energy densities from PCs[82].

The simplest ECMs, shown in Fig 3.4, have been widely used to describe the overall behavior of SCs. The model in Fig 3. 4(a) features a capacitance and an equivalent series resistance that represents the charging and discharging resistance. In contrast, Fig 3. 4(b) includes an equivalent parallel resistance connected in parallel with the capacitance to account for self-discharging losses. These two equivalent circuits are valuable for initial power system sizing and for simulating low-rate and stationary charging and discharging processes[83]. More detailed models, such as the multibranch models in Fig 3. 4(c), are not considered, as the dynamic behavior of the RC model is sufficient for this case.

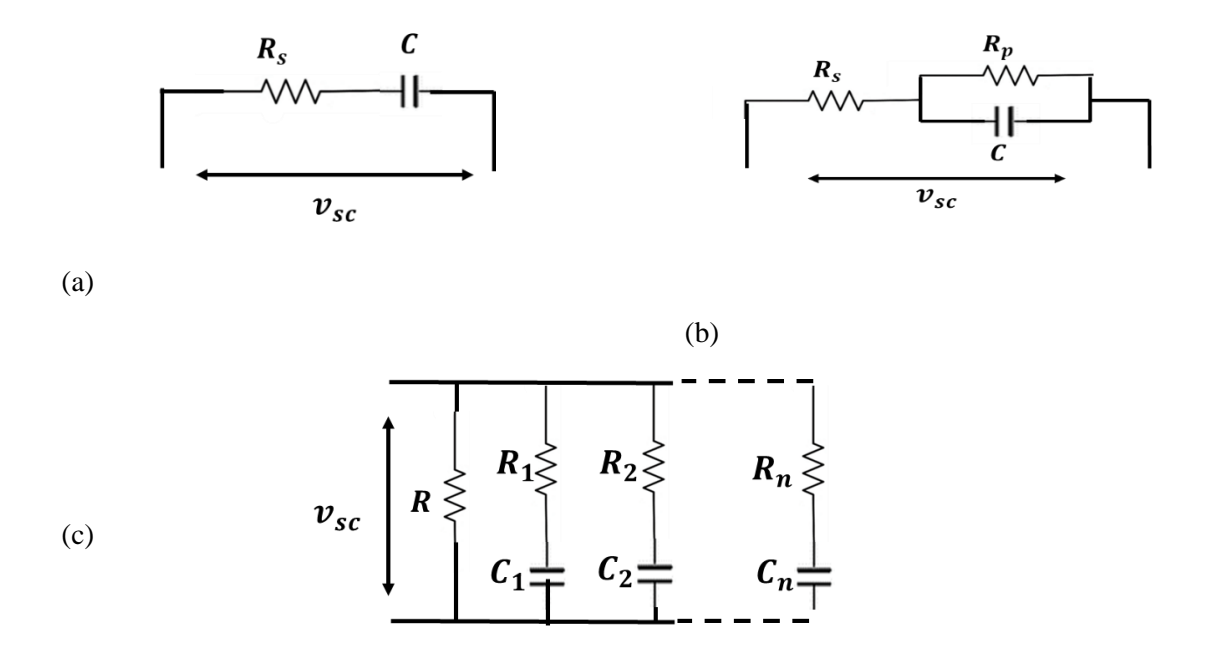


Fig 3.4: Supercapacitor ECMs: (a) simple model with equivalent series resistance, (b)simple model with equivalent parallel resistance, (c)multi-branch model

The following equation mathematically describes the electrical behavior of the SC [84]:

$$v_{sc} = R_s i_{sc} + \frac{1}{c} \int i_{sc} dt \tag{3.7}$$

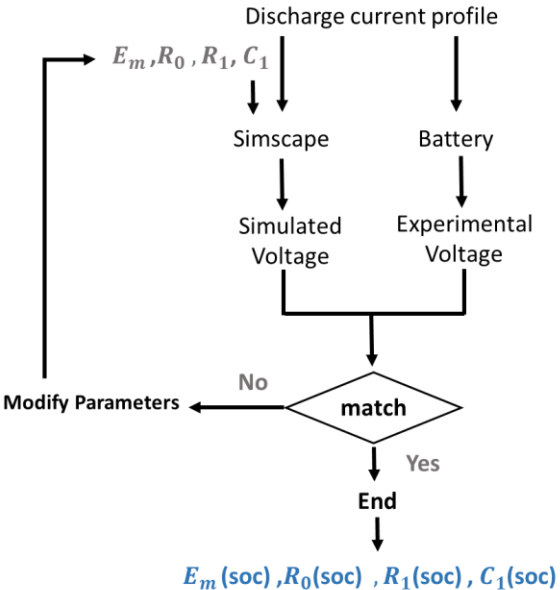
Unlike other types of batteries, SCs exhibit a more linear relationship between their remaining capacity and terminal voltage. Consequently, the SOC is frequently employed to estimate the remaining capacity of SC. The SOC of a supercapacitor can be mathematically expressed as [85]:

$$soc_{sc} = \frac{v_{sc} - v_{sc-\min}}{v_{sc-\max} - v_{sc-\min}}$$
(3.8)

 v_{sc} corresponds to the terminal voltage of the supercapacitor, while v_{sc-min} and v_{sc-max} indicate the minimum and maximum cut-off voltage of the supercapacitor, respectively.

3.2.3. Parameters identification

A detailed numerical parameter estimation scheme was implemented using pulse current discharge tests on LiFeYPO4 lithium-ion cells under various operating conditions with MATLAB®, Simulink®, and SimscapeTM. The tests, conducted at a single ambient temperature, ensured that parameters depended solely on the State of Charge. Data on voltage, current, and SoC were collected and used to calculate parameters through interpolation, stored in 1-D look-up tables with ten distinct SoC points. Parameter estimations of models were done in Simulink Parameter Estimation Toolbox (SPET), where initial values and constraints for each parameter were defined in the SPET, the constraints ensure the estimated parameters remain within realistic bounds. A Non-linear Least Squares was chosen as the solver method and the Trust-Region-Reflective algorithm was employed to solve non-linear equations, this algorithm iteratively adjusts the parameters to minimize the difference between the simulated and experimental data. A discharge profile was iteratively simulated, with results compared to experimental data to refine parameters and minimize errors. Final parameters, dependent on SoC, were integrated into the model using "From" blocks, ensuring accurate reflection of cell behavior across the entire SoC range. The model's accuracy was validated by comparing its output with experimental results, ensuring reliable predictions of cell behavior under various scenarios The flow diagram in Fig 3.5 outlines the steps involved in the parameter estimation process, while Fig 3.6 presents the results of this procedure[77] [78].



 E_m (SOC), κ_0 (SOC), κ_1 (SOC), ϵ_1 (SOC)

Fig 3.5: The flowchart of the parameter estimation process.

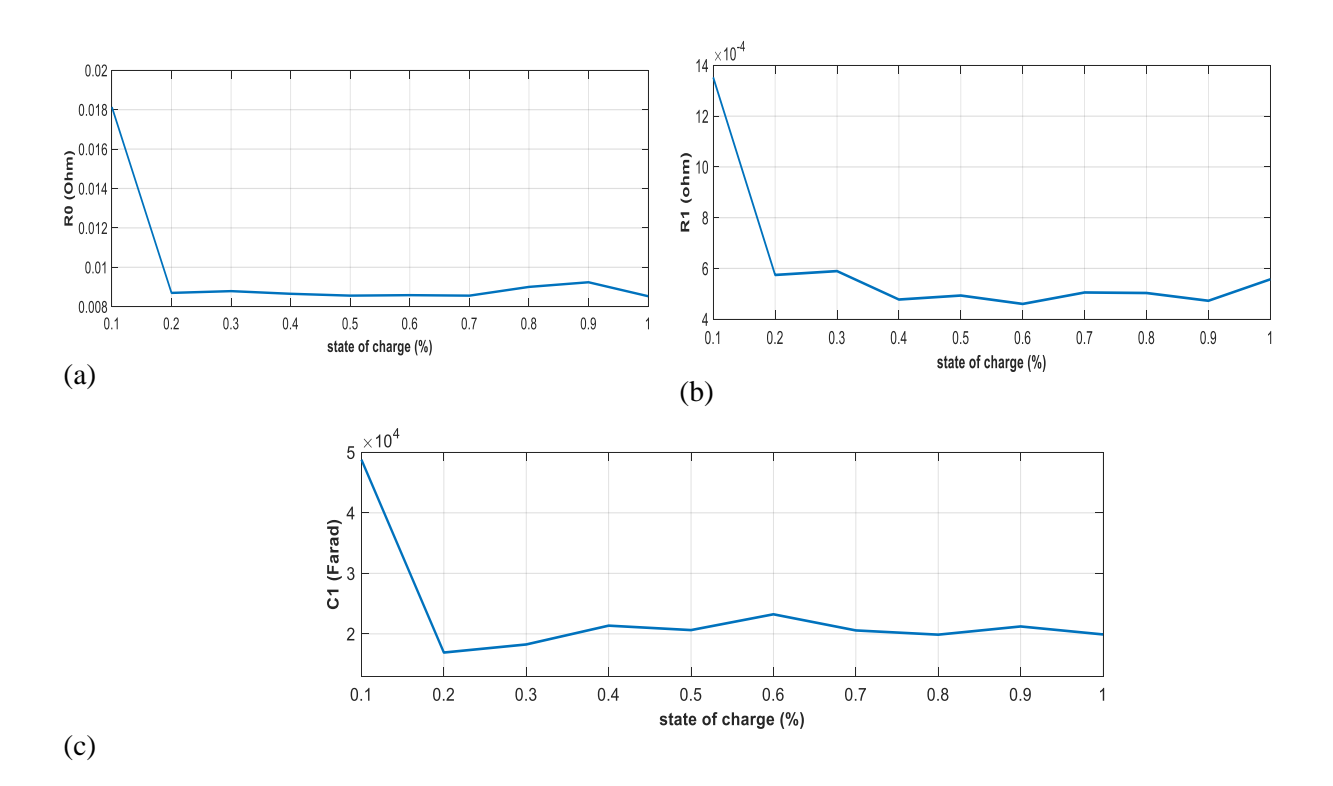


Fig 3.6. Battery parameters under different states of charge.

In the realm of battery model parameter identification, Recursive Least Squares algorithms are deduced in equation (3.9) play a crucial role by integrating the concept of the forgetting factor (λ) to assign more weight to recent data over past data.

$$\begin{cases} \hat{\theta}(k) = \hat{\theta}(k-1) + K(k) \left[y(k) - \hat{\phi}^T(k) \hat{\theta}(k-1) \right] \\ K(k) = \left(P(k-1)\theta(k) / (\lambda + \phi^T(k)P(k-1)\theta(k)) \right. \\ P(k) = \left[(1 - K(k)\phi^T(k))P(k-1) \right] / \lambda \end{cases}$$
(3.9)

Aiming to strike a balance between stability and accuracy, the optimal selection of forgetting factors is always needed to balance stability and accuracy. Therefore, in this work, the MAFF-RLS algorithm is adopted, which is described in [86], where the optimal value of the forgetting factor $\lambda(k)$ is computed based on the value of model voltage error. The experimental analysis shows that the relation between the model voltage error and the forgetting factor is non-linear. To solve this non-linear relationship, the standard half-parabola curve equation is considered as presented in Fig 3.7, for error values between 0.05 < |e(k)| < 0.005, the optimal value of $\lambda(k)$ is evaluated using the standard parabola equation. For e(k) values from 0 to 0.005, $\lambda(k)$ equals λ_{\max} , and for e(k) values greater than 0.05, e(k) equals λ_{\min} . The value of $\lambda(k)$ is determined based on the error value as follows:

$$\lambda(k) = \begin{cases} \lambda_{\text{max}} = 0.99; & for 0 < |e(k)| < 0.005 \\ \lambda_{\text{max}} - (\lambda_{\text{max}} - \lambda_{\text{min}}) \cdot (|e(k)| / e_{\text{max}})^2; & for 0.05 < |e(k)| < 0.005 \\ \lambda_{\text{min}} = 0.95; & for |e(k)| \ge 0.05 \end{cases}$$
(3.10)

According to the Thevenin model given in Fig 3.2(b), the transfer function of the battery impedance is obtained by its electrical equation in the Laplace domain and is expressed in the s-domain as follows:

$$E_b = (\frac{R_1}{R_1 C_1} + R_0)i_b + v_b \tag{3.11}$$

By using the bilinear transformation method, the (3.11) can be written as (3.12) and the coefficients can be expressed as below:

$$\frac{V_{b,k}}{I_k} = \frac{a_2 + a_3 z^{-1}}{1 - a_1 z^{-1}} \tag{3.12}$$

$$\begin{bmatrix} a_1 \\ a_2 \\ a_3 \end{bmatrix} = \begin{bmatrix} (\Delta T - 2R_1C_1)/(\Delta T + 2R_1C_1) \\ (R_0\Delta T + R_1\Delta T + 2R_0R_1\Delta T)/(\Delta T + 2R_1C_1) \\ (R_0\Delta T + R_1\Delta T - 2R_0R_1\Delta T)/(\Delta T + 2R_1C_1) \end{bmatrix}$$
(3.13)

where ΔT refers to the sampling time interval.

by using (3.11), the recursive equation in discrete time form can be expressed as:

$$v_{b,k} = (1 - a_1)E_{b,k} + a_1E_{b,k-1} + a_2I_k + a_3I_{k-1}$$
(3.14)

The discrete-time form (3.14) can be rewritten as:

$$V_{b,k} = \theta_k^T \varphi_k \tag{3.15}$$

Where,

$$\begin{cases} \theta_{k} = \left[(1 - a_{1}) E_{b,k} & a_{1} & a_{2} & a_{3} \right] \\ \varphi_{k} = \left[1 & E_{b,k-1} & I_{k} & I_{k-1} \right] \end{cases}$$
(3.16)

Now, the battery model parameters can be identified by using the expression (3.17)[86], and the results of the process are depicted in Fig 3.8.

$$\begin{bmatrix} E_{b,k} \\ R_0 \\ R_1 \\ C_1 \end{bmatrix} = \begin{bmatrix} a_1/(1-a_2) \\ -(a_2-a_3)/(1+a_1) \\ 2(a_1a_2+a_3)/(1+a_1^2) \\ \Delta T(1+a_1)^2/4(a_1a_2+a_3) \end{bmatrix}$$
(3.17)

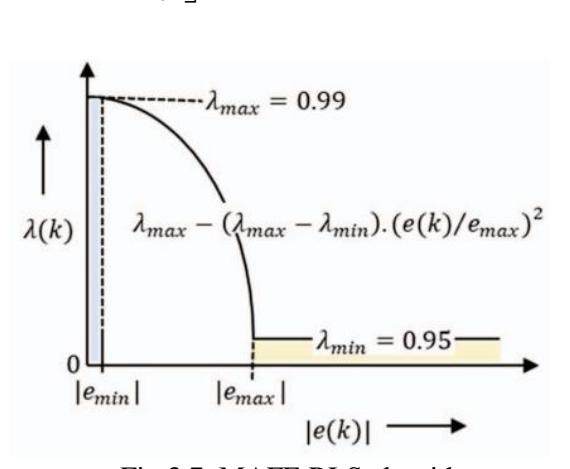


Fig 3.7: MAFF-RLS algorithm concept

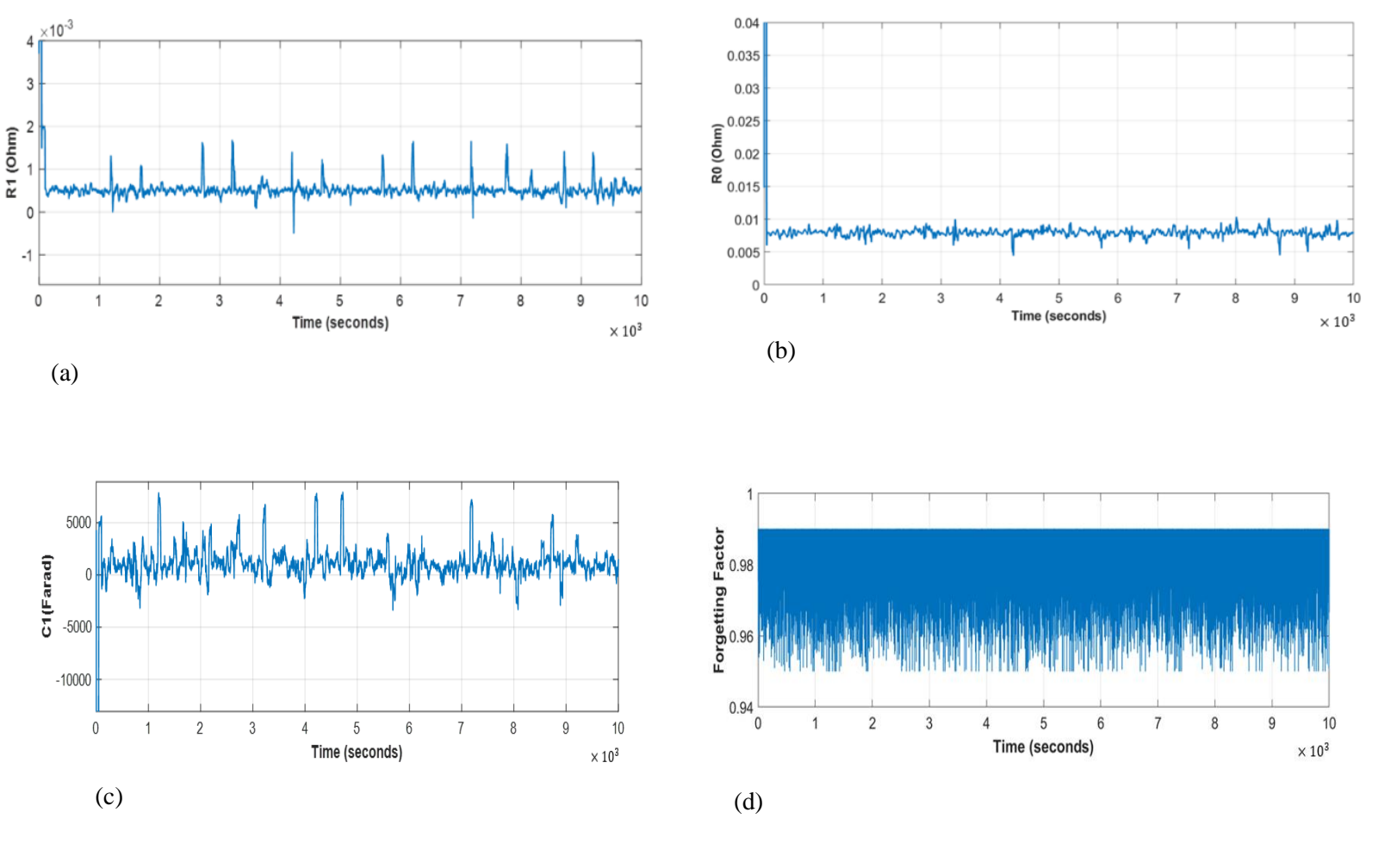


Fig 3.8: Parameter identification results using the MAFF-RLS algorithm: (a) Ohmic resistance R_0 ; (b) Polarization resistor R_{cp} ; (c) Polarization capacitor C_{cp} ; (d) Forgetting factor variation λ .

The identification of supercapacitor parameters involves conducting constant-current discharge tests on the Maxwell module to collect voltage and current data, which are then utilized in the parameter estimation process [87] mentioned above to obtain the real SC parameters, the results are summarized in Table 3.2.

Table 3. 2: The Parameter Identification Results of supercapacitor

Parameter	R_s	С
Value	$7.2~(\mathrm{m}\Omega)$	159 (F)

3.3.DC bus modeling

To ensure smooth and reliable power flow from various sources to the load, the sources are interconnected via a DC bus. The voltage on this bus must be regulated around a reference value, which depends on the transformation ratio of the DC/DC converters connected to the bus. Proper regulation of this voltage allows for efficient collection and routing of energy from the sources to the traction motor. The capacitor on the DC bus helps maintain voltage stability by absorbing or supplying charge as needed. In the circuit diagram shown in Fig 3.9, the DC bus capacitor is depicted with various currents flowing through it, connecting to components such as a traction motor, a battery, and a supercapacitor. The mathematical model of the DC bus captures these interactions can written as:

$$C_{dc} \cdot \frac{dv_{dc}}{dt} = i_b + i_{sc} - \frac{v_{dc}}{R_{dc}} - i_l$$

$$(3.18)$$

$$i_b \qquad \qquad i_l$$

$$c_{dc} \qquad \geqslant R_{dc}$$

Fig 3.9: Equivalent circuit of the dc bus.

The resistor R_{dc} connected in parallel with the capacitor C_{dc} provides a safe discharge path when the system is turned off, preventing residual voltage buildup. It also emulates the leakage current of real capacitors and helps slightly dampen voltage fluctuations.

3.4.DC/DC converter modeling

The modeling of the DC-DC converter behavior is crucial for designing the HESS controller, as it aims to control the energy flow to DS efficiently. By regulating the DC-DC converter output voltage and current through Pulse Width Modulation (PWM) applied to the IGBT. This research contains a battery as the main source and a supercapacitor as the auxiliary source connected to the DC bus via a single-layer bidirectional DC-DC converter to ensure bidirectional energy transfer

between sources and the DC bus (the secondary source being reversible in current). The boost mode discharges sources, while the buck mode charges the supercapacitor to maintain the DC bus voltage at a set reference value.

The state-space average model is employed to represent the DC-DC converter illustrated in Fig 3.10, considering the ON and OFF states of the IGBT. The average model of the buck-boost converter on the battery side is expressed as:

$$L_b \cdot \frac{di_{b-mes}}{dt} = v_b - v_{dc} \cdot (1 - \alpha_b) \tag{3.19}$$

Similarly, the average model of the buck-boost converter on the supercapacitor side is given by:

$$L_{sc} \cdot \frac{di_{sc-mes}}{dt} = v_{sc} - v_{dc} \cdot (1 - \alpha_{sc}) \tag{3.20}$$

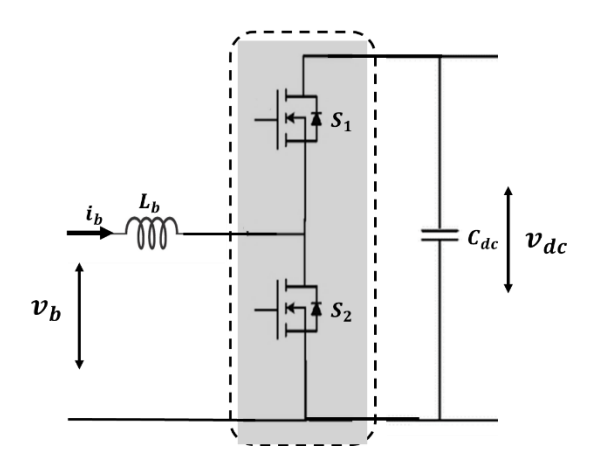


Fig 3.10: Schematic circuit of the buck-boost converter

3.5. Traction chain modeling

3.5.1. Vehicle Dynamics model

The behavior of a moving vehicle is influenced by all the forces acting on it in a given direction as shown in Fig 3.11. The tractive force F_{i} at the contact area between the drive wheels' tires and the road surface propels the vehicle forward. This force is generated by the torque from the power plant, which is then transmitted through the drivetrain to the driving wheels. As the vehicle moves, it encounters resistance that opposes its motion. To determine the power needed to propel the vehicle forward, the fundamental principle of dynamics is applied [88]:

$$\begin{cases}
 m_{v} \frac{\overrightarrow{dv}}{dt} = \sum \overrightarrow{F_{ext}} \\
 \overrightarrow{F_{ext}} = \overrightarrow{F}_{t} - (\overrightarrow{F_{rf}} + \overrightarrow{F_{slope}} + \overrightarrow{F_{aero}})
\end{cases}$$
(3.21)

 F_{aero} represents the aerodynamic drag force and is given by:

$$F_{aero} = \frac{1}{2} \rho_{air} v^2 A_f C_d \tag{3.22}$$

where ρ_{air} is the air density, ν is the vehicle speed, A_f is the frontal area of the vehicle, and C_d is the aerodynamic drag coefficient.

The rolling resistance force of the wheels on the ground, F_{rf} is determined by the formula:

$$F_{rf} = C_r m_v g \cos(\alpha) \tag{3.23}$$

where C_r is the rolling resistance coefficient, g is the acceleration due to gravity, α is the angle, and m_v is the vehicle mass.

The gravitational force F_{slope} , which depends on the slope of the road, is calculated as:

$$F_{slope} = m_{\nu} g \sin(\alpha) \tag{3.24}$$

The tractive force F_t can be expressed as:

$$F_{t} = m_{v} \frac{dv}{dt} + F_{rf} + F_{slope} + F_{aero}$$
(3.25)

$$F_{t} = m_{v} \frac{dv}{dt} + C_{r} m_{v} g \cos(\alpha) + m_{v} g \sin(\alpha) + \frac{1}{2} \rho_{air} v^{2} A_{f} C_{d}$$

$$(3.26)$$

The mechanical power P_m required to propel the vehicle forward is:

$$P_m = F_t.v \tag{3.27}$$

$$P_{m} = v(m_{v}\frac{dv}{dt} + C_{r}m_{v}g\cos(\alpha) + m_{v}g\sin(\alpha) + \frac{1}{2}\rho_{air}v^{2}A_{f}C_{d})$$
(3.28)

According to the previous equation, the load torque T_L is given by:

$$T_L = F_T . r ag{3.29}$$

With r is the tire radius

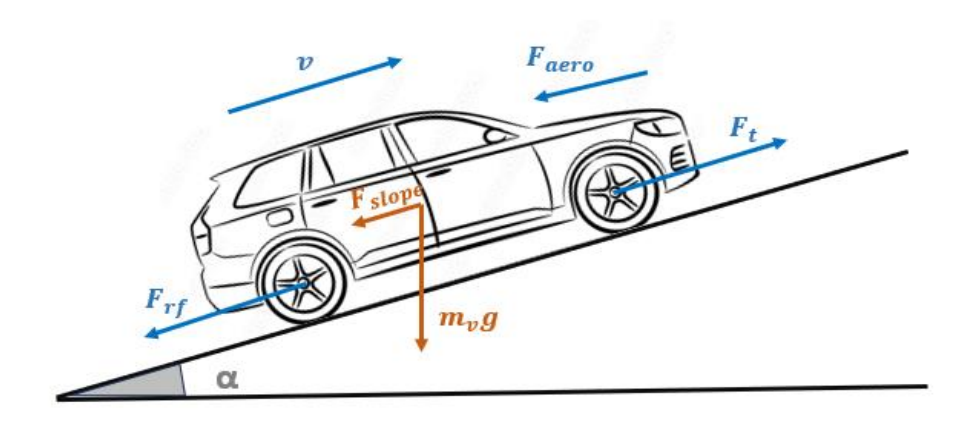


Fig 3.11: Schematic representation of forces acting on a vehicle in motion

3.5.3. Traction motor

Motors are a key component of the drivetrain in EVs. For an electric motor to be effective in driving an EV, it must be highly efficient, have a high-power density, and be cost-effective. Unlike industrial motors or conveyors, EV motor drives require frequent starts and stops, rapid acceleration and deceleration, high torque at low speeds, low torque at high speeds, and a wide range of operating speeds. DC motors are the oldest type of motors used in electric vehicles for their simplicity, cost-effectiveness, and durability. Especially, permanent magnet DC motors which eliminate the energy losses associated with field windings by using permanent magnets to create a consistent magnetic field without additional electrical power. This efficiency is complemented by the motor's compact size and lighter weight, which are crucial for EV design where space and weight are critical considerations. Additionally, PMDC motors provide a higher power density, meaning they can generate more power relative to their size, making them ideal for maximizing performance in EVs.[89],[90].

To simplify and focus on our main objective, which is validating energy management techniques, our choice was directed towards a PMDC, therefore two PMDC motors were adopted, the first one is subject to speed control to simulate the traction aspect of an electric vehicle, while the second DC motor is controlled to emulate the road driving conditions. The characteristics of the vehicle considered are given in the table.

To determine the maximum power required by the motor, the formula (3.30) is used. Assuming flat terrain and the vehicle maintaining a constant maximum speed, the motor power is calculated to be 200W. This is the power that must be supplied by the motor, which operates with an efficiency ranging from 70% to 90%, depending on the technology used:

$$P_{mot} = \frac{P_m}{\eta_{mot}} \tag{3.30}$$

Consequently, a PMDC motor with a nominal voltage of 24V and a power rating of 250W has been selected.

Since the motor being used is a PMDC motor, the inductor component is negligible, and the motor can be represented by the diagram in Fig 3.12[91]:

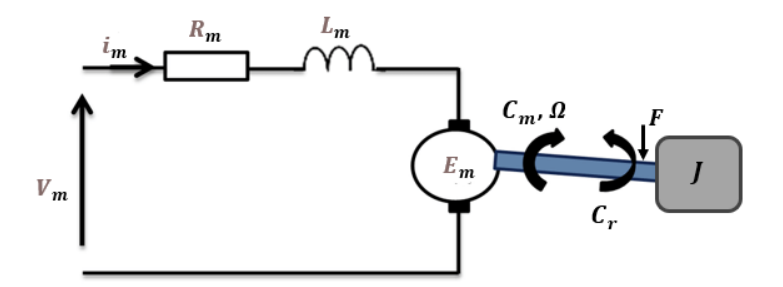


Fig 3.12: Equivalent circuit of permanent magnet DC motor.

From the previous figure, the electrical and mechanical equations of the motor are written as:

$$V(t) - E(t) = L\frac{dI(t)}{dt} + R.I(t) \quad \text{with } E(t) = K_b.\Omega(t)$$
(3.31)

$$C_m = J \frac{d\Omega(t)}{dt} + F\Omega(t) + C_r \quad \text{with } C_m = K_t.I(t)$$
(3.32)

Moving from the time domain to the Laplacian domain gives us the following current and velocity equations:

$$I(s) = \frac{V(s) - E(s)}{L \cdot S + R}$$

$$(3.33)$$

We have: τ_{ele} electrical time constant. With:

$$\tau_{ele} = \frac{L}{R} \rightarrow I(s) = \frac{V(s) - E(s)}{R(1 + \tau_{ele}.S)}$$
(3.34)

$$\Omega(S) = \frac{C_m - C_r}{J.S + F} \tag{3.35}$$

 τ_{mec} mechanical time constant. With:

$$\tau_{mec} = \frac{J}{F} \to \Omega(S) = \frac{C_m - C_r}{F(1 + \tau_{mec} S)}$$
(3.36)

In practical systems, the friction coefficient F is never zero due to losses like mechanical friction and air resistance. In high-efficiency or simplified models, F may be negligible. Here, the mechanical time constant becomes undefined as $F \to 0$. To prevent mathematical singularity in simulations or control design, a small positive value ε is assigned to F, ensuring numerical stability while approximating nearly lossless behavior.

From relations (33) and (35), a block diagram that represents the motor is obtained in Fig 3.13:

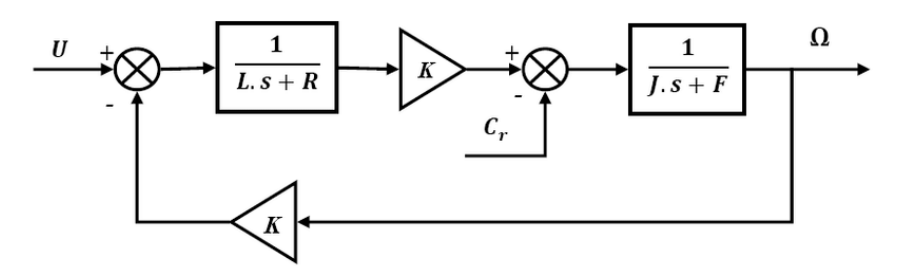


Fig 3.13: Open-loop PMDC block diagram.

3.5.3. Regeneration

Considering driving patterns and road traffic conditions, a vehicle frequently needs to decelerate, which typically requires braking. During this process, the vehicle's kinetic energy can be converted into heat or electricity. In conventional friction brake systems, this excess kinetic energy is transformed into unwanted and wasted heat due to friction. In contrast, regenerative braking allows the vehicle to slow down by converting its kinetic energy into electricity, which can be stored or

used immediately. Regenerative braking works on the principle that the traction motor generates negative electromagnetic torque, effectively functioning as a generator. For regeneration to occur, the propulsion powertrain system spanning from the energy source to the traction wheels must support bidirectional energy flow, and the energy source itself must be capable of receiving power. In practice, only 30% to 50% of this energy can be recovered due to conversion losses. However, the amount of energy that can be regenerated depends on various factors, mainly the motor, deceleration rate, and the receptiveness of the ESS.

The braking controller is the main part of the braking system, responsible for executing the necessary braking scenarios to decelerate a vehicle and manage its energy. Its primary goal is to stop the vehicle at the desired rate. This is typically achieved using a traditional closed-loop circuit, as shown in Fig 3.14, where the controller (C) compares the reference speed with the actual speed of the EV and generates a torque reference for the brakes, producing the required braking torque. [92],[93].

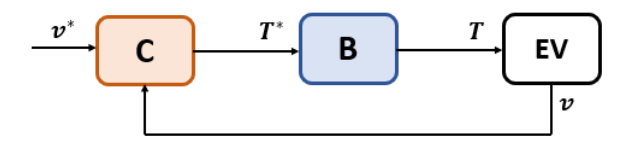


Fig 3.14: Braking system model representation.

3.6. Sizing of sources

The dimensioning of energy sources in a vehicle depends on the dynamic performance requirements of DS, particularly the vehicle's maximum speed and acceleration times. Maximum speed requirements influence the power demand on the energy sources, necessitating a powertrain capable of delivering sufficient continuous power to achieve and sustain high speeds without efficiency losses or overheating. While acceleration performance dictates the peak power requirements, requiring energy sources to handle significant bursts of power over short periods.

To calculate the size limit of the hybrid power supply i.e. the battery and the supercapacitor, a power requirements analysis is conducted to determine the power needed for maximum speed and

acceleration, the total energy needed for typical driving cycles, factoring in regenerative braking and other energy recovery mechanisms.

The energy consumption is calculated based on the road loads, and the total power is calculated as the product between the total road forces and the vehicle speed as previously mentioned in equation (3.27). By integrating the total power over time (for the whole duration of the cycle), we get the total energy consumption [94],[95]:

$$E_{total} = \int P_m . dt \tag{3.37}$$

The energy consumption varies depending on the driving force as shown in Fig 3.11 where two cases are distinguished:

During Acceleration $(F_t \ge 0)$:

$$E_{acc} = \int P_m dt \tag{3.38}$$

This integral represents the total energy consumed when the driving force is positive (i.e., during acceleration).

During Deceleration $(F_t < 0)$

$$E_{acc} = \int P_m . dt. \phi \tag{3.39}$$

This formula includes a recovery efficiency factor ϕ to account for the energy recovered during regeneration (regenerative braking).

The battery pack is considered the main power source and is designed to handle 300 watts. It consists of a specific number of cells, determined as follows[96]:

The number of battery cells connected in series N_{cs} is calculated by dividing the nominal battery pack voltage U_{bp} by the voltage of each battery cell U_{bc} . Since the number of strings must be an integer, the result is rounded up to the nearest whole number.

$$N_{cs} = \frac{U_{bp}}{U_{bc}} \tag{3.40}$$

The nominal battery pack voltage $U_{\it bp}$ is calculated using:

$$U_{bp} = \frac{V_{dc}}{\Upsilon} \tag{3.41}$$

where Υ is the boost ratio. The maximum output voltage is about 2-3 times the input voltage. Exceeding this ratio can cause input currents to become large and expensive, including the switching devices, and significantly decrease efficiency[97].

The energy content of a string E_{bs} in watt-hours is equal to the product of the number of battery cells connected in series and the energy of a battery cell E_{bc}

$$E_{bs} = N_{cs} \cdot E_{bc} \tag{3.42}$$

The total number of strings in the battery pack N_{sp} is calculated by dividing the battery pack's total energy E_{bp} by the energy content of a string. The result is rounded up to the nearest whole number

$$N_{sp} = \frac{E_{bp}}{E_{bs}} \tag{3.43}$$

The total energy of the battery pack E_{bp} can then be recalculated as the product of the number of strings and the energy content of each string.

$$E_{bp} = N_{sb}.E_{bs} \tag{3.44}$$

The battery pack capacity C_{bp} in ampere-hours is calculated as the product of the number of strings and the capacity of a battery cell C_{bc} .

$$C_{bp} = N_{sb}.C_{bc} \tag{3.45}$$

The batteries available in the lab have a nominal voltage of 3.3V. To ensure a stable operation of the associated buck-boost converter considering the boost ratio, five of these batteries are connected in series, resulting in a total voltage of 16.5V. Each battery has a capacity of 100 Ah, meaning it can deliver a current of 100A for one hour or a lower current for a proportionally longer duration. The minimum recharging capacity of these batteries is denoted as C1, corresponding to a recharging current of 100A, enabling the battery to be fully recharged in one hour. However, due to the unavailability of a source capable of supplying such a high current, a more practical

recharging method known as C10 is often used. This means the battery is recharged at a current of 10A, taking 10 hours to fully recharge.

SCs serve as an auxiliary energy source that engages during the acceleration and braking phases of a vehicle. The sizing of SC is determined based on the specific power requirements of their intended application.

Let W_{sc} denote the energy stored in the supercapacitor at a given moment, which can be expressed as [98]:

$$W_{sc} = \frac{1}{2} C_{sc} V_{sc}^2 \tag{3.46}$$

If the allowable voltage limits for the discharge process are considered, the energy variation can be expressed as:

$$\Delta W_{sc} = \frac{1}{2} C_{sc} (V_{sc-\text{max}}^2 - V_{sc-\text{min}}^2)$$
 (3.47)

Typically, $V_{sc-\min}$ is set to $V_{sc-\max}/2$, leading to an energy variation of:

$$\Delta W_{sc} = \frac{3}{8} C_{sc} V_{sc-\text{max}}^2 \tag{3.48}$$

which accounts for 75% of the stored energy. Given the energy needs of the system to which SC must deliver its charge, defined ΔW_{need} , some simple calculations lead to the capacity sizing as:

$$C_{sc} = \frac{8}{3} \frac{\Delta W_{need}}{V_{sc-max}^2} \tag{3.49}$$

To find the number of serial cells needed N_{s-sc} based on the individual cell voltage V_{sc-c} and the required maximum voltage V_{\max} , you can use the following formula:

$$N_{s-sc} = \frac{V_{\text{max}}}{V_{sc-c}} \tag{3.50}$$

In this case, the Maxwell BMOD0165 module is used, which has a nominal voltage of 48 V, a capacity of 165 F, and contains 18 cells

3.7.conclusion

This chapter provides a detailed description and explicit modeling of the various components of the HEV chosen for tests which consists of a hybrid electric system (battery/SC) and a PMDC for the traction part. The storage sources have been sized and their parameters identified. Furthermore, the dynamic model of the vehicle is discussed. Before exploring different EMSs in the next chapter, it is necessary to establish models of the various subsystems. This modeling enables us to predict system performance once the proposed control strategies are implemented.

Chapter 4

Description of proposed strategies

4.1.Introduction

The problem of energy flow management is to find the best power distribution. Thus, developing an EMS is crucial to ensure optimal power distribution within a HESS, while also addressing operational constraints such as storage capacities and frequency domain specifications. Choosing the right distribution requires evaluating various performance criteria, including the source lifespan, driving comfort, autonomy, and other relevant factors[34].

This chapter introduces a set of frequency-based energy management systems designed to optimize energy allocation, extend battery life, and lower EV-related costs. The content is structured into two parts and focuses on distributing energy among sources according to their performance across different frequency ranges.

- The first part introduces a new adaptive wavelet approach that dynamically adjusts the decomposition level in response to the supercapacitor's soc. It also evaluates this approach against three alternative frequency-based approaches.
- The second part presents an innovative adaptive wavelet approach based on Dynamic Pattern Recognition. This involves developing a driving pattern recognition system that integrates kmeans clustering with SVM classification techniques and adapting fuzzy logic using the output from the driving pattern recognizer.

To achieve the intended goals, these strategies consider:

- Precise control of static converters to ensure smooth energy flow to the load
- Designing a driving system that emulates real electric vehicle driving conditions

4.2.HEV emulator

4.2.1. Description

HEV topological architecture typically consists of an electrical power system and a driving system, as illustrated in Fig 4.1. EPS is mainly made up of Li-ion batteries, SCs, and two bidirectional DC/DC converters that allow power to flow from sources to loads during discharging mode and back into sources during charging mode. Depending on the control mode, the HESS topology can be defined as passive, semi-active, or active. The ability of the active structure for the HESS to

regulate the power distribution between the battery and SC makes it an attractive option. This structure not only increases power transfer efficiency but also protects the battery by reducing the effects of high peak currents during cycles of charging and discharging in EVs[99]. On the other hand, the DS combines electromechanical drive with vehicle dynamics, which renders it susceptible to outside interference such as changing road conditions and driver-initiated speed adjustments.

Two PMDC motors were regulated in terms of speed and torque, respectively, to emulate the traction aspect and improve vehicle efficiency. To deliver accurate speed and torque control, a motor controller manages the motor's voltage and current in response to sensor inputs and driver inputs. Through regenerative braking, which converts the energy of motion from the vehicle into electrical energy and feeds it back into the electrical power supply, the motor controller can switch the motor into generator mode when on the brakes. Via the DC link, the DS interacts with the EPS to obtain electricity.

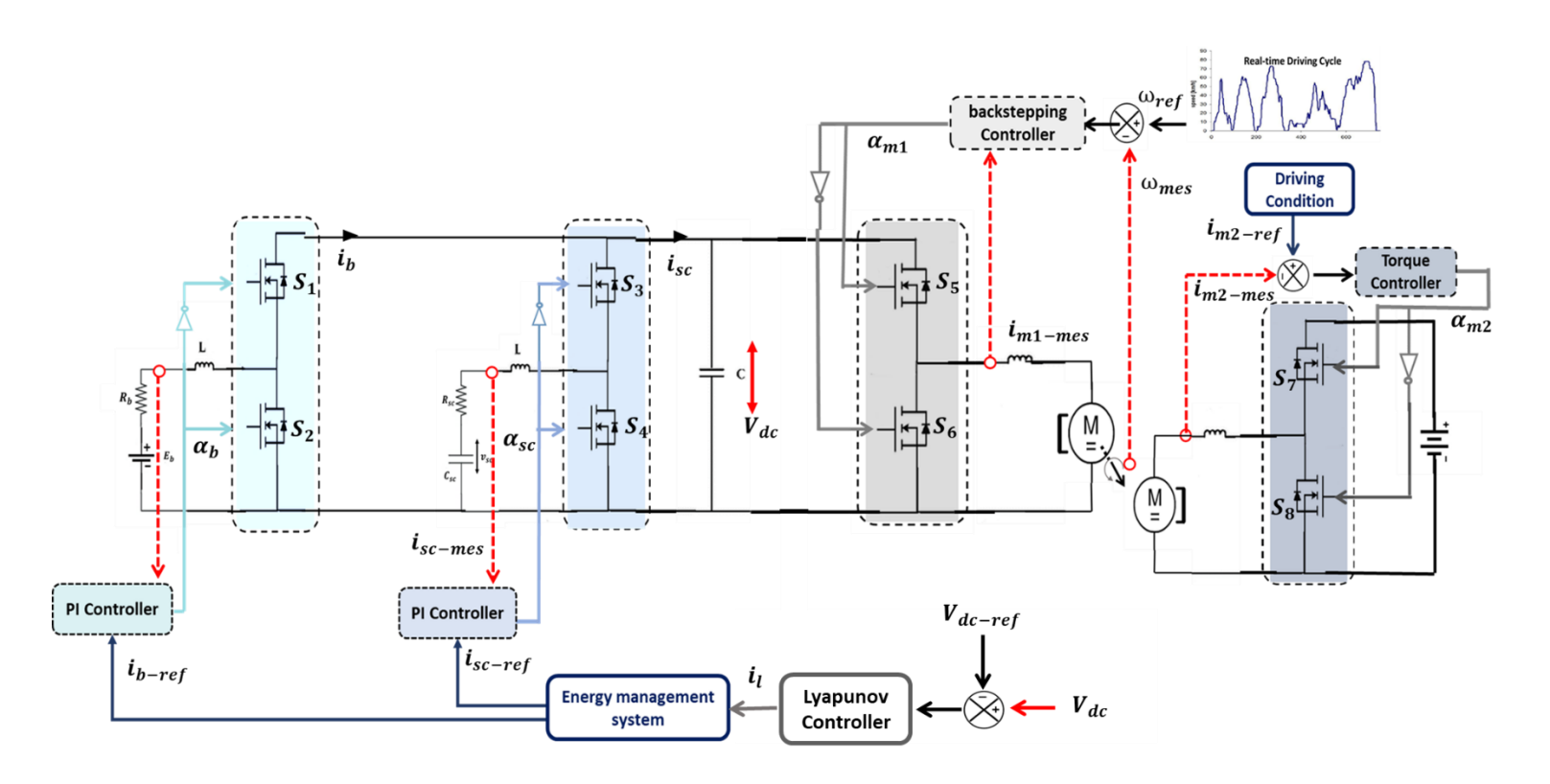


Fig 4.1. Topology Configuration of HEV.

4.2.2. System modeling

In the process of developing the mathematical model for the power system shown in Fig 4.1, it will be assumed that the converters function in a continuous, lossless conduction mode and that their switching frequency is higher than that of the passive components. Therefore, Equation (4.1) can be used to define the relationship between input and output power, where P_{in} and P_{out} represent the corresponding input and output powers:

$$p_{in}(t) = p_{out}(t) \tag{4.1}$$

$$p_{b}(t) + p_{sc}(t) = p_{dc}(t) \tag{4.2}$$

Equation (4.2) can be expressed in terms of source voltages and currents as follows:

$$v_b(t) \cdot i_{b-mes}(t) + v_{sc}(t) \cdot i_{sc-mes}(t) = v_{dc}(t) \cdot i_l(t)$$

$$(4.3)$$

The importance of keeping the DC-link voltage constant is emphasized by equation (4.3) and is represented as

$$i_{l}(t) = \frac{p_{dc}(t)}{v_{dc}(t)} \tag{4.4}$$

Considering the previous equation, the output current will be treated as an image of the output power if the DC-link voltage is kept constant

The dynamic equations of the HESS can be written by taking into account the average model of the converters [100]:

$$\begin{cases} L_{b} \cdot \frac{di_{b-mes}}{dt} = v_{b} - v_{dc} \cdot \alpha_{b} - R_{b} \cdot i_{b-mes} \\ L_{sc} \cdot \frac{di_{sc-mes}}{dt} = v_{sc} - v_{dc} \cdot \alpha_{sc} - R_{sc} \cdot i_{sc-mes} \\ C_{dc} \cdot \frac{dv_{dc}}{dt} = i_{b-mes} \cdot \alpha_{b} + i_{sc-mes} \cdot \alpha_{sc} - \frac{v_{dc}}{R_{dc}} - i_{l} \end{cases}$$

$$(4.5)$$

where $\begin{bmatrix} i_b & i_{sc} & v_{dc} \end{bmatrix}$ represents the state vector and $\begin{bmatrix} \alpha_b & \alpha_{sc} \end{bmatrix}$ are the duty ratios that act as control inputs.

It's worth noting that Control structures significantly impact system dynamics because they directly affect stability and convergence. Dynamic stability, a fundamental property of well-designed systems, emphasizes their quick ability to recover equilibrium during disruptions. Consequently, a hierarchical control structure was adopted to manage the suggested system dynamics, the lower level was assigned to the current control loops, and the upper level to the DC-link voltage control loop. This setup requires that the closed-loop dynamics of the current control loop should be about five times quicker than those of the external loop regulating the DC link.

4.2.3. Converters control approaches

Despite the wide range and variety of current control systems in power electronics converters, they all acknowledge the significance of accuracy and simplification during the modeling stage. To properly model power electronic converters, one must have an in-depth knowledge of several aspects of the converter, such as its physical architecture, the complex models of the different voltage/current control loops, the protection strategy used, etc. Although the control architecture is known, the parameters and control settings differ greatly between manufacturers. This might cause faulty modeling and simulation of the power system, resulting in incorrect findings and analysis[101].

These difficulties can be more easily resolved by employing data-driven control approaches, which can be developed with minimal or no prior knowledge of the converter's control system or topology. Additionally, data-driven models typically demand less computational power compared to more intricate component-level models. These models are often created using system identification tools, such as those available in MATLAB [101]. Fig 4.2 exhibits the core concepts of a system identification procedure. To identify an unknown dynamic process, the input signal u(t) and output signal y(t) are first recorded. The dataset is subsequently fed into a system identification algorithm, that generally minimizes a predetermined cost function to estimate the system model.

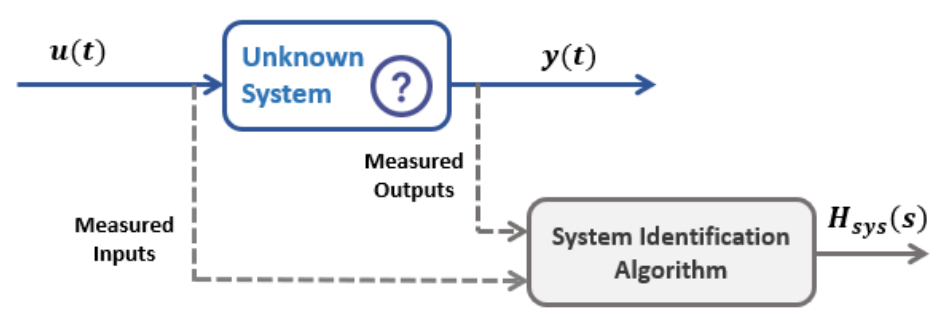


Fig 4.2. System identification principle

The same converter structure is used for both the battery and the supercapacitor, and it can be modeled with a second-order transfer function model with two poles and no zeros, providing that the DC-link voltage is maintained at its setpoint. The transfer function of the system is given by the equation below:

$$H_{sys}(s) = \frac{b_0}{s^2 + a_1 s + a_0} \tag{4.6}$$

For adjusting sources currents according to their references obtained by the proposed EMSs, the control system utilizes internal closed loops using a PI controller as a predefined fixed controller structure within a data-driven approach due to its popularity in industry, durability, low design complexity, and simplicity of implementation [102]. The PI controllers were fine-tuned using the previously specified transfer functions based on the needed performance, such as desired response time and overshoot. The PI controller's transfer function can be defined as follows:

$$H_{pi}(s) = k_p + \frac{k_i}{s} \tag{4.7}$$

Both the SC and battery error signals are indicated by:

$$\begin{cases} e_b = i_{b-ref} - i_{b-mes} \\ e_{sc} = i_{sc-ref} - i_{sc-mes} \end{cases}$$

$$(4.8)$$

The current control loops regulate the battery and SC output currents using equations (4.9) and (4.10):

$$\begin{cases} \alpha_b = H_{pi,b} \cdot e_b \\ \alpha_{sc} = H_{pi,sc} \cdot e_{sc} \end{cases}$$

$$\tag{4.9}$$

$$\begin{cases} i_b = \alpha_b \cdot i_{b-mes} \\ i_{sc} = \alpha_{sc} \cdot i_{sc-mes} \end{cases}$$
 (4.10)

 α_b and α_{sc} are the buck-boost converter's common control input variables, which can be set as follows [103]:

$$\alpha_b(s_1) + (1 - \alpha_b(s_2)) = 1 \tag{4.11}$$

$$\alpha_{sc}(s_3) + (1 - \alpha_{sc}(s_4)) = 1 \tag{4.12}$$

4.2.4. DC- link voltage control

To guarantee that both power sources contribute optimally to the traction portion, the DC-link voltage must be controlled to a specific value. The controller uses a Lyapunov function to derive an energy function that includes the regulation error [104]. This error can be defined as the difference between the desired reference voltage and the actual DC-link voltage. By adjusting the error voltage and guiding it towards zero, the controller efficiently maintains the DC-link voltage. The following equations provide the DC-link's current equilibrium:

$$c\frac{dv_{dc}}{dt} = i_b + i_{sc} - i_l \tag{4.13}$$

For a finite time, convergence of the tracking error of the DC-link voltage to zero, a positive definite candidate Lyapunov function and its targeted gradient are selected as:

$$v = \frac{1}{2}e^2 \tag{4.14}$$

$$v = e e = -k_{dc}e^2 \tag{4.15}$$

here denotes e the error voltage, which is the difference between the required reference voltage V_{dc-ref} and the real DC-link voltage V_{dc} . The system energy will gradually decrease as a result of the negative sign $(-k_{dc}e^2)$ in equation (4.15), leading the system towards stability and convergence to its targeted reference voltage.

The rate of change of the error voltage over time can be determined by:

$$\dot{e} = \dot{v}_{dc} - \dot{v}_{dc-ref} = \frac{1}{c} (i_b + i_{sc}) - \frac{1}{c} i_l = -k_{dc} e$$
(4.16)

$$-k_{dc} \times c \times e + i_l = i_b + i_{sc} \tag{4.17}$$

From equations (4.16) and (4.17), the controller outcome gives $(i_b + i_{sc})$ as joint reference amounts, the reference current is allocated to each source based on the EMS chosen. It is worth mentioning that the good choice of the constant k_{sc} enhances the dynamic state.

4.3. Frequency-based energy management strategies

Frequency-based energy management strategies distribute energy among sources based on their performances within different frequency ranges. Such methods take advantage of the unique strengths of each energy source, with batteries performing better at low frequencies and supercapacitors excelling at high frequencies. Therefore, before delving into the proposed energy management strategies, we will first review traditional strategies to enable an analytical comparison.

4.3.1. Fixed frequency-based energy management system:

In a frequency-based EMS, the load current is split into low-frequency components, which reflect steady and slowly changing power demands, and high-frequency components, associated with rapid or transient power fluctuations. This separation is achieved using a low-pass filter, indicated in the following equation [105]:

$$\begin{cases}
H_{Lo-D} = \frac{1}{\tau \cdot s + 1} \\
\tau = \frac{1}{2\pi f_c}
\end{cases}$$
(4.18)

Wherein τ is the cut-off period. The following equations provide the references for the currents at the filter output that relate to the supercapacitor and battery:

$$I_{b-ref} = I_L \cdot \frac{1}{\frac{1}{(2\pi f_c) \cdot s} + 1} \tag{4.19}$$

$$I_{sc-ref} = I_L - I_{b-ref} \tag{4.20}$$

Although the technical capability of this technique, selecting the optimal cut-off frequency for the filters used remains a major limitation. Putting the cut-off frequency too low may overload the supercapacitor, resulting in loss of energy, whereas setting it too high could stress the battery, thus limiting its life. The optimal cut-off frequency is determined by finding the dominant frequency components obtained from Fourier analysis of the load current.

4.3.2. Adaptive frequency-based energy management system

In EMSs, Load current fluctuations varied according to driving conditions, keeping fixed cut-off frequencies insufficient for effective energy distribution. Therefore, adaptive filters adjust the cut-off frequencies based on driving conditions, optimizing power distribution between energy sources. This approach continuously monitors the load current and the supercapacitor soc, as seen in Fig 4.3.

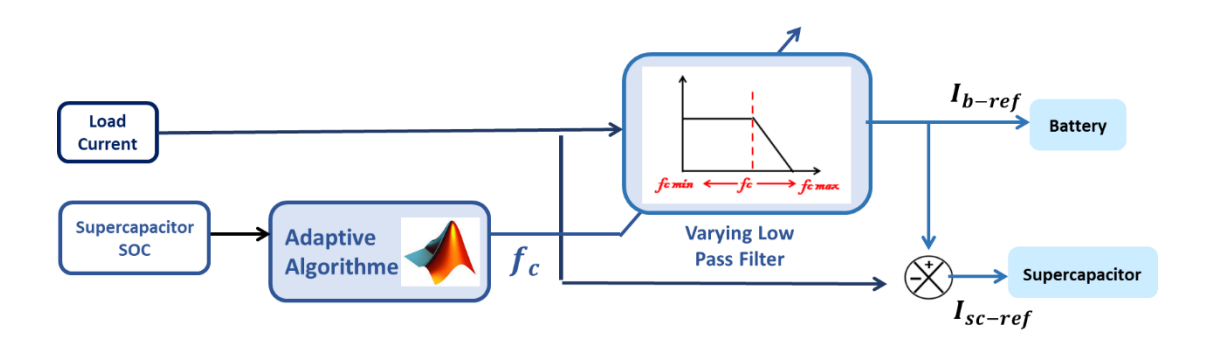


Fig 4.3. A schematic representation of the adaptive frequency separation technique

In this study, the adaptive filter utilizes three distinct cut-off frequencies: $fc_{\rm max}$, $fc_{\rm min}$, and $fc_{\rm nom}$, as outlined in Table 4.1. The frequency $fc_{\rm max}$ is employed when the supercapacitor's soc is low, necessitating greater energy contribution from the battery. Conversely, $fc_{\rm min}$ is used when the supercapacitor's soc is high, indicating substantial energy reserves, which allows the supercapacitor to efficiently manage high-frequency load components, thereby reducing the strain on the battery and extending its lifespan. The nominal cut-off frequency, $fc_{\rm nom}$ is applied under normal operating conditions with moderate power demands, enabling both the battery and supercapacitor to contribute according to their capabilities. By dynamically adjusting the cut-off

frequency, the adaptive filter ensures effective power distribution between the energy sources, taking into account the system's specific energy requirements across varying operating conditions.

Table 4.1: A dynamic frequency cut-off operation

Frequency symbol	fc_{\min}	fc_{nom}	$fc_{ m max}$
Frequency value (HZ)	0.06	0.03	0.01
Sc state of charge (%)	$soc_{sc} \ge 70$	$70 \ge soc_{sc} \ge 50$	$soc_{sc} \leq 50$

4.4. Wavelet-based energy management system

4.4.1. Conventional Wavelet-based energy management system

Vehicle power demand often exhibits sudden peaks and transient variations, which may adversely affect battery longevity. These brief transients are especially important in power analysis. WT is a robust mathematical technique that can analyze transient phenomena by decomposing a signal into components across different positions and scales in both time and frequency domains. WT has gained attention for its exceptional ability to differentiate transient power demands from the base power load. This capability is particularly useful in HESSs. As illustrated in Fig 4.6, this strategy allocates the detected transients to the supercapacitor, which is well-suited to managing the rapid variations associated with such phenomena.

Mathematically, the WT is performed by convolving the power signal with a set of functions known as wavelets, which are compact, oscillatory patterns and localized in both time and frequency. Their scale and position can be adjusted, enabling the examination of different frequency components of a signal across varying time intervals. The wavelet transform of a signal X(t) is expressed by [106]:

$$w(\lambda, u) = \int_{R} x(t) \frac{1}{\sqrt{\lambda}} \psi\left(\frac{t - u}{\lambda}\right) dt$$
(4.21)

The original signal can be identified as X(t), while its wavelet coefficients are represented as $W(\lambda, u)$.

Here, λ represents the scale factor, while u refers to the position factor in the wavelet transform procedure. Additionally, $\psi(t)$ signifies the mother wavelet.

The Haar wavelet, characterized by its simplicity in mathematical design and short filter length, is a commonly utilized wavelet function. In this research, the HWT was selected for energy management in EVs, particularly for real-time algorithm applications. It offers advantages such as efficient real-time signal processing and identical forward and inverse transforms. The HWT is noted as [107]:

$$\psi(t) = \begin{cases} 1 & t \in [0, 0.5] \\ -1 & t \in [0.5, 1] \\ 0 & otherwise \end{cases}$$
 (4.22)

The wavelet filtering process involves two main phases: decomposition (Fig 4.4a) and reconstruction (Fig 4.4b). During decomposition, the signal $\mathcal{X}(t)$ is divided into two components using a low-pass filter L_{O_D} and a high-pass filter H_{i_D} , producing the approximation (low-frequency component) A_n and the detail (high-frequency component) D_n . This procedure is repeated iteratively for each chosen level n. Supercapacitor, battery, and load current are defined as follows:

$$i_{b-ref} = A_n \tag{4.23}$$

$$i_{sc-ref} = D_1 + D_2 + \dots + D_n$$
 (4.24)

$$i_1 = D_1 + D_2 + \ldots + D_n + A_n \tag{4.25}$$

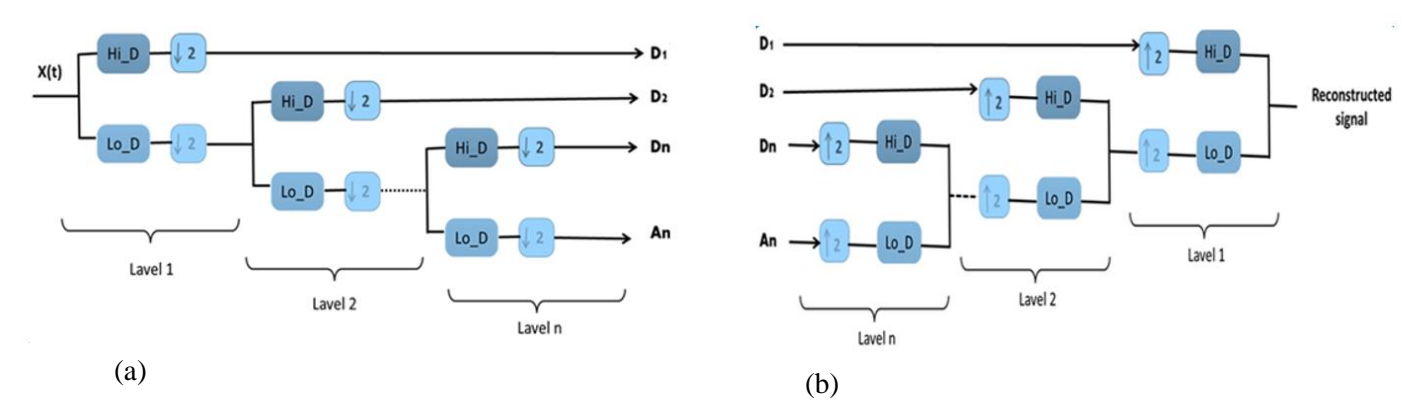


Fig 4.4. Concept of Haar wavelet transform: (a)Decomposition phase ;(b) Reconstruction phase.

The choice of wavelet decomposition levels is crucial because power demand varies significantly across different decomposition levels. Generally, the frequency range impacting batteries is within Hz, whereas the load power demand signal is sampled at 1 Hz [108]. The resulting decomposition level, calculated using Equation (30), typically falls within the range of [2, 5], taking into account the sampling frequency f_s , the power demand frequency on the battery pack f_c , and the relationship between signal frequency and decomposition level.

$$n = \left| \frac{\log(f_s / f_c)}{\log(2)} - 1 \right| \tag{4.26}$$

Real-time signal processing using WT is achieved by incorporating a fixed-length sliding window, which enables the extraction of characteristic parameters from driving cycles in real time [109]. A specified number of samples are taken from the signal, processed, and then output after filtering. The window then shifts forward, adding a new sample to the dataset while discarding the first one. This process repeats until the entire signal has been processed. Fig 4.5 illustrates the sliding window process. It is worth noting that the equilibrium between sliding window length W and decomposition level n is critical for improved filter reconstruction. For optimal results, the relationship between W and n should meet the inequality $w \ge 2*2^n$ [110].

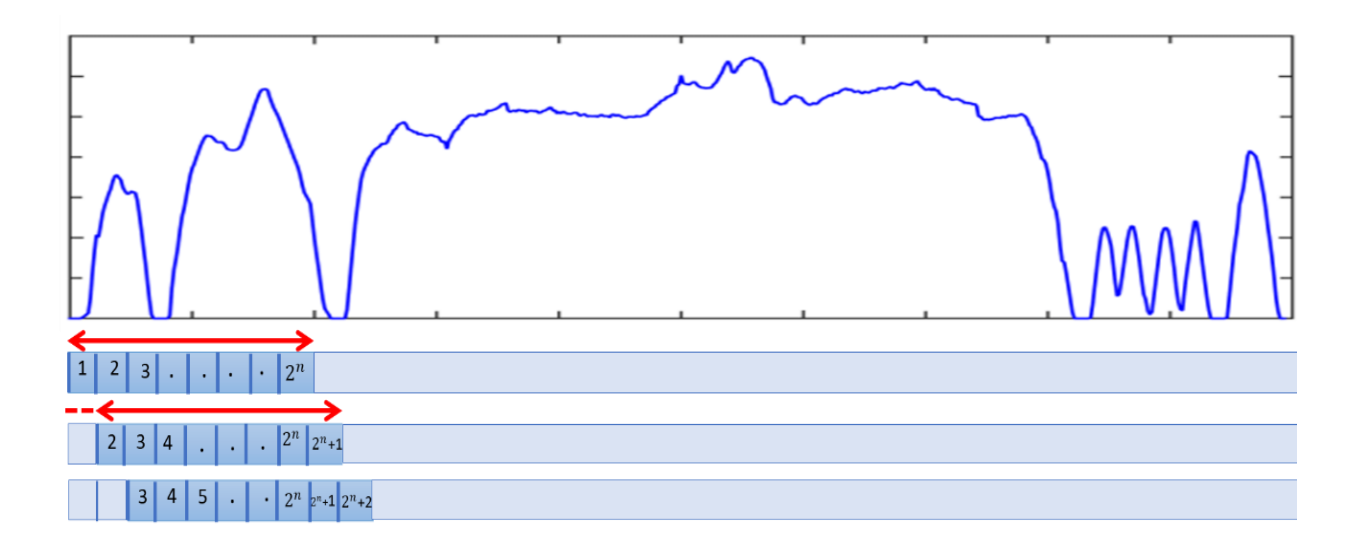


Fig 4.5. Sliding window concept.

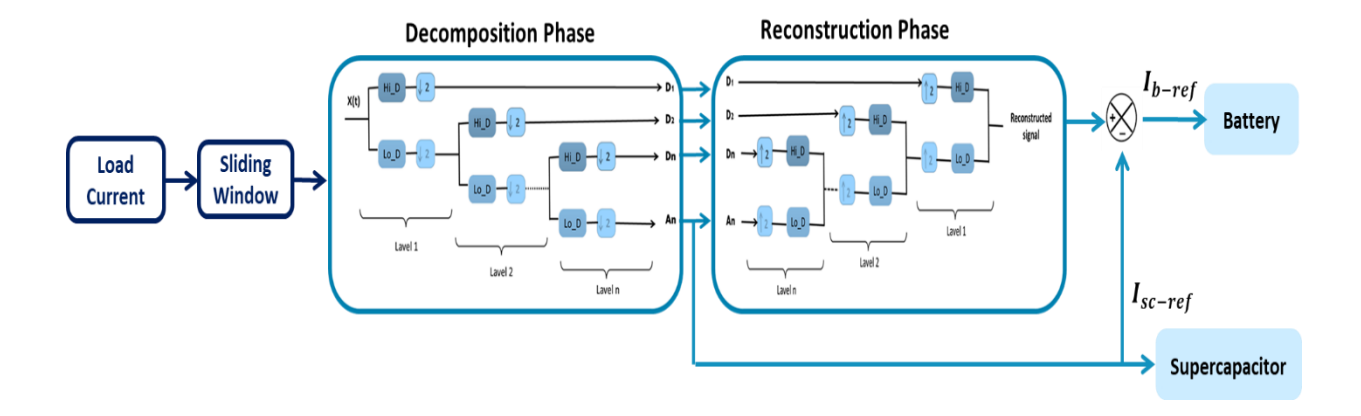


Fig 4.6. Wavelet transform technique diagram.

4.4.2. Adaptive wavelet-based energy management system

Due to the limitations of conventional WT-based EMS systems, which usually rely on a fixed decomposition level linked to a single frequency decomposition, an innovative Adaptive Wavelet Transform based on Supercapacitor soc is suggested. This advanced system intelligently adjusts the decomposition level in real-time by analyzing the supercapacitor SoC, as illustrated in Fig 4.7.

The AWT adjusts the decomposition level to suit varying power needs and driving conditions. When the supercapacitor's SOC is high, indicating high energy reserves, the approach intelligently selects a higher decomposition level, such as the fifth level. This strategic selection is crucial for accurately and efficiently managing sudden power variations and transients, making full use of the supercapacitor strengths. By assigning the SC the responsibility of handling these power surges, the system reduces the battery workload during such periods, thereby extending its lifespan and improving the overall efficiency of the system.

Conversely, when the supercapacitor's SOC is low or nearly depleted, the approach conservatively lowers the decomposition level, such as to the 2nd level. This adjustment is intended to conserve the supercapacitor's remaining energy, resulting in the battery taking on the majority of the load's power demands. Additionally, during operation when the SoC is within an optimal range, which is common during normal system performance, the methodology strategically selects intermediate decomposition levels, such as the 3rd or 4th. These choices are influenced by the discharge rate of the supercapacitor, as shown in the flowchart in Fig 4.8.

The fifth level operates when the supercapacitor's energy storage surpasses 80%, thereby decreasing the sudden demand for the batteries. In contrast, levels 3 and 4 become operational when the charge state falls between 40% and 80%, taking into account the rate of supercapacitor discharge. Level 4 is selected when the discharge rate exceeds 5%, while Level 3 is preferred when it falls below this threshold. However, if the supercapacitor's SoC drops below 40%, the system switches to the 2nd level to preserve a minimum amount of stored energy, ensuring the supercapacitor contributes at the lowest possible rate.

This adaptive approach ensures that the SC operates within an optimal SoC range while considering the unique characteristics of the energy source, allowing power allocation to be perfectly aligned with the system's needs. As a result, it not only improves the SC's performance but also reduces the strain on the battery, promoting a longer lifespan and reliable functionality over time.

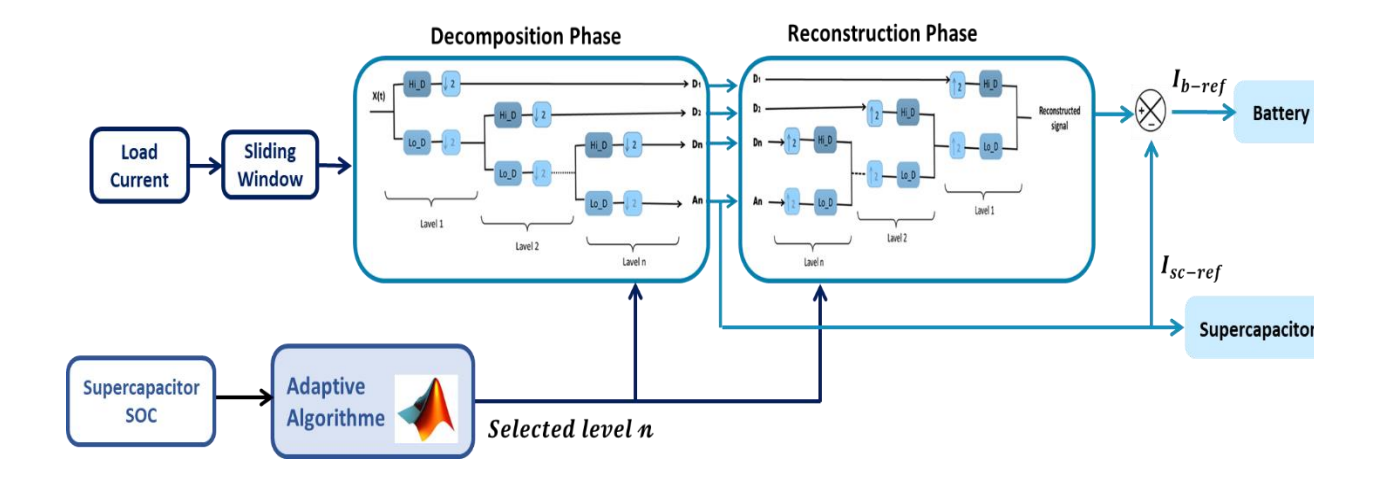


Fig 4.7. Schematic representation of adaptive wavelet transform technique

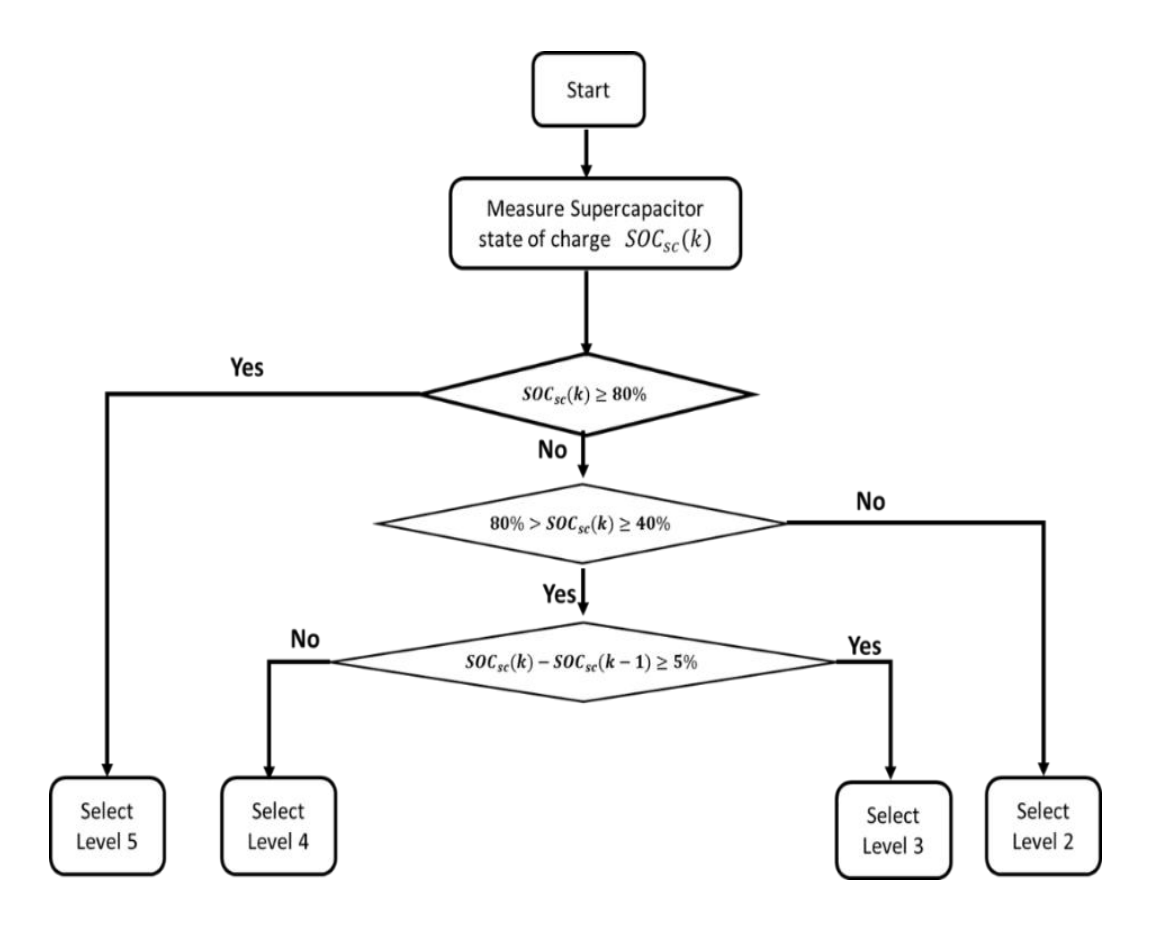


Fig 4.8. Adaptive process flowchart

4.5. Adaptive Wavelet-Adaptive Fuzzy Logic based K-Means-SVM Pattern Recognition

This strategy is an improved version of the previous, where some aspects have been improved through these contributions:

- Introduction of an adaptive wavelet-based on Dynamic Pattern Recognition, providing versatile adaptation to various driving scenarios.
- Enhancement of DPR using k-means clustering for unsupervised categorization and SVM classification for improved real-time decision-making.

Adoption of adaptive fuzzy logic, allowing real-time adjustments of membership functions
and rules to align with changing driving conditions, ensuring optimal supercapacitor
maintenance and protecting the battery from peak current stress.

A schematic overview of this strategy is illustrated in Fig 4.9. It comprises an offline-trained SVM classifier and the real-time operation of three key components: an online recognition process for identifying driving patterns, an AWT algorithm that decomposes load power demand based on the recognized pattern, and AFL, which ensures maintaining the SC at the optimal level while safeguarding the battery from high peak current.

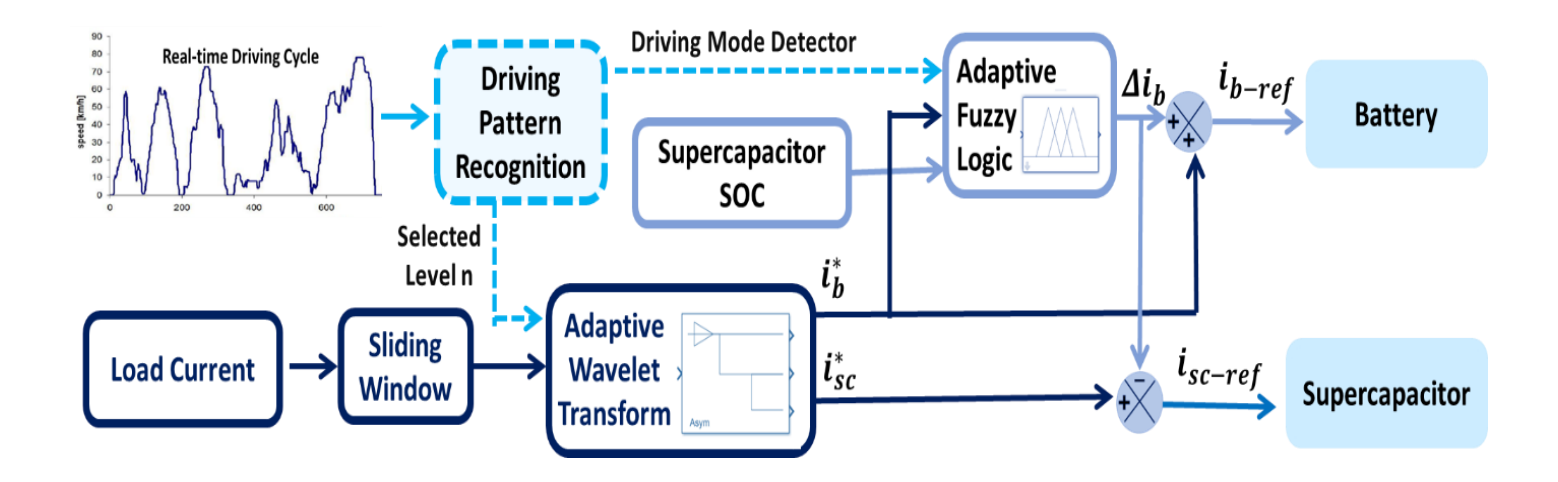


Fig 4.9. The concept of Adaptive Wavelet-Adaptive Fuzzy Logic based K-Means-SVM Pattern Recognition EMS.

4.5.1. Driving Pattern Recognition

In the field of DPR, two main approaches are commonly used. The first, Predictive Driving Pattern Recognition, relies on data from connected vehicles, geographic information systems (GIS), and vehicle navigation systems. While this method is highly accurate, it demands a large amount of data and significant computational resources. On the other hand, Identification Driving Pattern Recognition analyzes historical and real-time route data to identify key factors defining the current driving pattern. The current driving behavior can be recognized by comparing these factors with known patterns. Although this retrospective method is simpler and more user-friendly, it may not be as accurate as the predictive approach. Choosing a DPR algorithm greatly influences the

accuracy of condition recognition. However, accuracy is also shaped by other factors, such as the complexity of the driving environment, the quantity and quality of training data, and the diversity of driver behaviors.

The operational process of the DPR system is depicted in the graphic in Fig 4.10 and involves two primary steps.

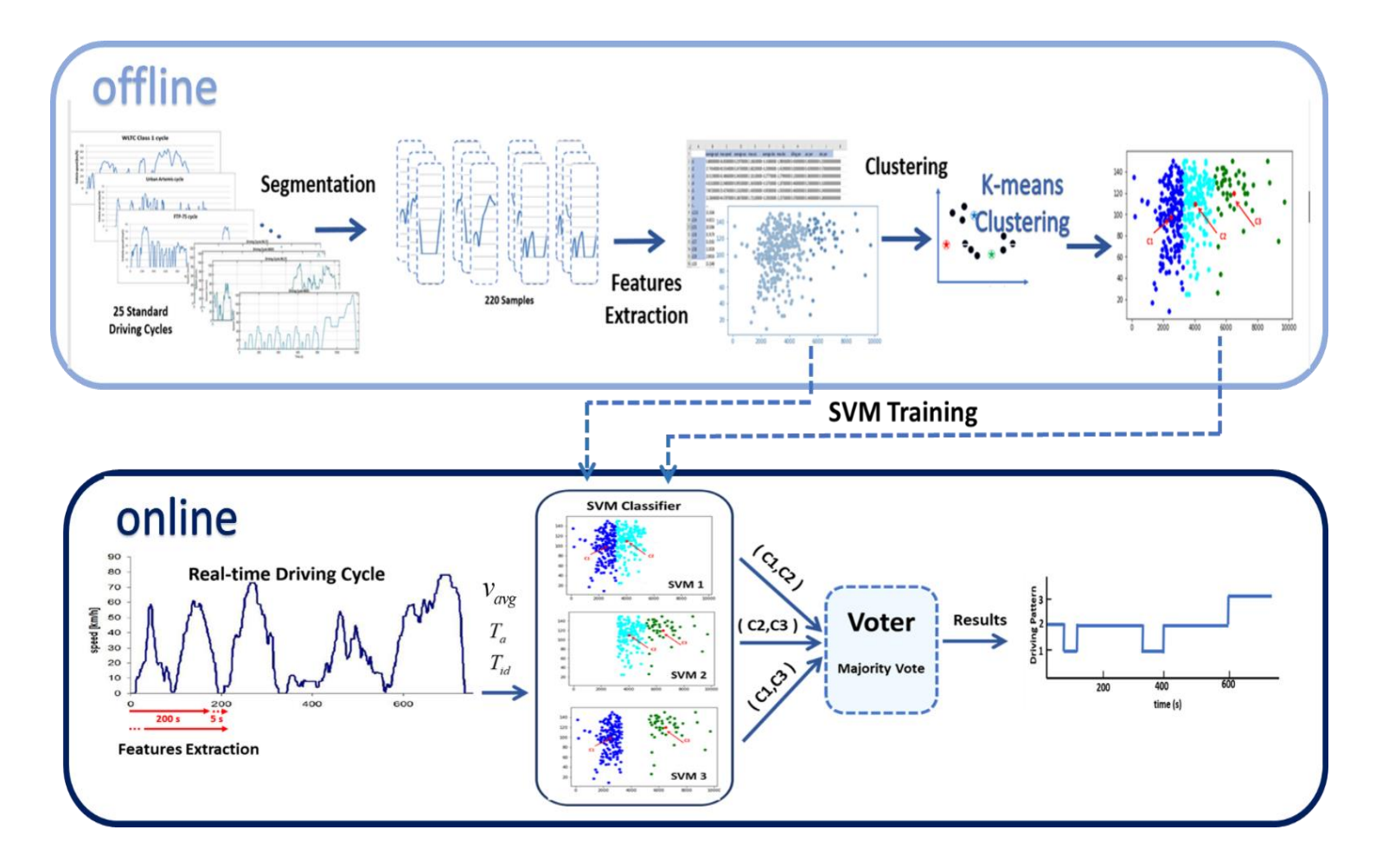


Fig 4.10. Driving pattern recognition framework

The DPR system begins with an Offline Training phase, where 25 driving cycles with various patterns are segmented, and distinctive features are extracted from 220 samples. Principal Component Analysis is used to simplify the data, cluster centers are formed using the k-means method, and the Support Vector Machine is trained on this data. In the Online Recognition phase, real-time speed data is collected to derive feature values from the most recent 200 seconds, with

samples taken every 5 seconds. These features are then fed into the SVM classifier, which produces three possible outcomes, and the final driving pattern is identified through a voting mechanism.

4.5.1.1. Extraction of the driving patterns characteristic parameters

Typical driving patterns must

accurately represent real-world driving behaviors and exhibit distinct feature vector values, making it easier to categorize actual driving patterns into predefined groups [111]. In this study, 25 driving cycles are included in the training dataset, with each cycle segmented into 100-second intervals. Nine key parameters, detailed in Table 4.2, are selected as characteristic features to represent these patterns. Due to the high dimensionality of these features, which can limit real-time driving pattern recognition, PCA is employed to reduce the complexity of the data. PCA simplifies the dataset by transforming it into a lower-dimensional space, making it more manageable

keeping the fundamental properties required for pattern recognition. The procedural steps of PCA involve processing a dataset with n samples, each described by p variables, arranged in $n \times p$ matrix [112].

$$x = \begin{bmatrix} x_{11} & x_{12} & \cdots & x_{1p} \\ x_{21} & x_{22} & \cdots & x_{2p} \\ \vdots & \vdots & & \vdots \\ x_{n1} & x_{n2} & \cdots & x_{np} \end{bmatrix}$$
(4.27)

The correlation coefficient matrix is first computed, which includes deriving the correlation coefficient.

$$R = \begin{bmatrix} r_{11} & r_{12} & \cdots & r_{1p} \\ r_{21} & r_{22} & \cdots & r_{2p} \\ \vdots & \vdots & & \vdots \\ r_{n1} & r_{n2} & \cdots & r_{np} \end{bmatrix}$$
(4.28)

$$r_{ij} = \frac{\sum_{k=1}^{n} (x_{ki} - \overline{x_i})(x_{kj} - \overline{x_j})}{\sqrt{\sum_{k=1}^{n} (x_{ki} - \overline{x_i})^2 \sum_{k=1}^{n} (x_{kj} - \overline{x_j})^2}}$$
(4.29)

By resolving the eigenvalue equations $|\lambda i - R| = 0$, the eigenvalues can be obtained and then arranged in descending order as $\lambda_1 \geq \lambda_2 \geq \cdots \geq \lambda_p \geq 0$. The corresponding eigenvectors are then calculated $e_i(i=1,2,\ldots,p)$, satisfying the condition $\sum_{i=1}^p e_{ij}^2 = 1$

The principal component contribution rate of each sample, F_i , is calculated as $\lambda_i / \sum_{k=1}^p \lambda_k$, with $(i=1,2,\ldots,p)$. Furthermore, the cumulative contribution from principal components F_1 through F_k is determined by the following expression:

$$\sum_{k=1}^{i} \lambda_{k} / \sum_{k=1}^{p} \lambda_{k} \ (i = 1, 2, \dots, p)$$
(4.30)

The PCA results focus on principal components with eigenvalues greater than or near 1, ensuring that the cumulative variance contribution exceeds 80%. The number of principal components selected is determined by identifying the point at which the eigenvalues experience a significant drop [113], as illustrated in Fig 4.11, the eigenvalues drop below 1 after the third component.

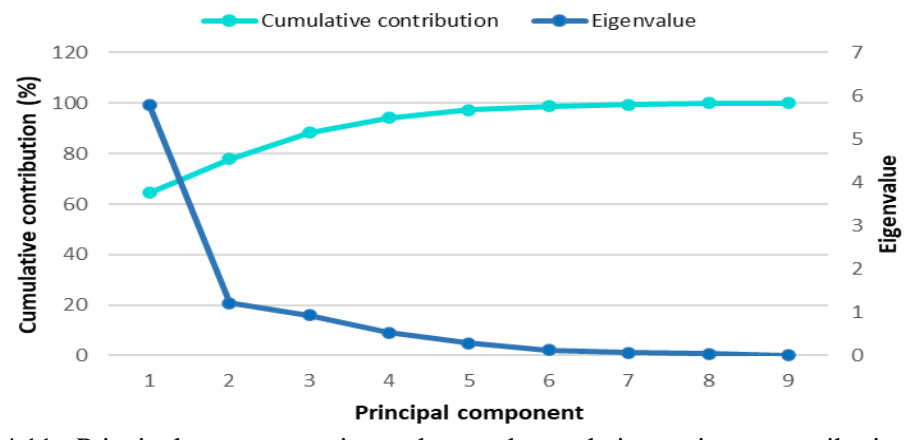


Fig 4.11: Principal component eigenvalues and cumulative variance contribution rate

When reducing the original dimensional training dataset to more manageable dimensions. These parameters are chosen based on their correlation with the original dataset, with a strong correlation

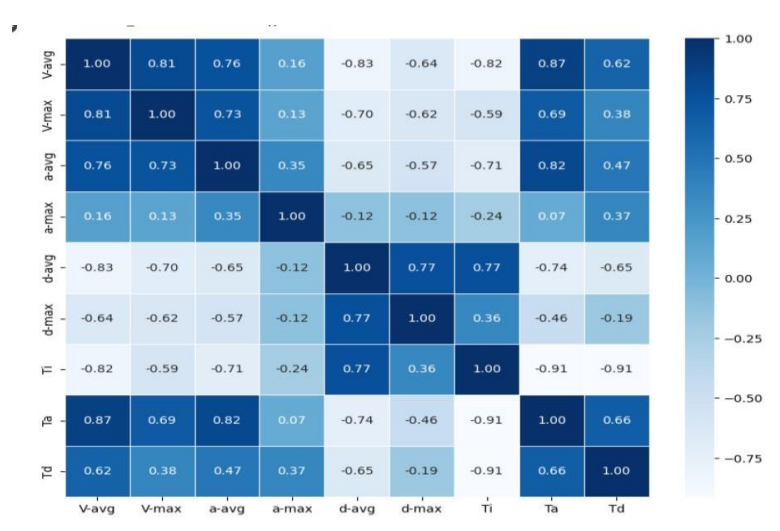


Fig 4.12. Correlation of the characteristic features

indicating the presence of shared dominant factors among the components of the driving feature vector [114], based on Fig 4.12, these characteristic parameters are Average velocity, Time ratio of idling and Time ratio of acceleration.

Table 4.2: The characteristic criteria used for the recognition of patterns

			-
Symbol	Parameter	Unit	Mathematical description[115]
V_{avg}	Average velocity	m/s	$v_{avg} = \frac{\int v dt}{t}$
$v_{ m max}$	Maximum velocity	m/s	$v_{\max} = \max\left(v_i, i = 1, 2, \dots, k\right)$
a_{avg}	Average acceleration	m/s^2	$a_{avg} = \frac{\int a dt}{t}, (a > 0)$
a_{max}	Maximum acceleration	m/s^2	$a_{\max} = \max\left(a_{\max}, i = 1, 2, \dots, k\right)$
$d_{\scriptscriptstyle avg}$	Average deceleration	m/s^2	$d_{avg} = \frac{\int a dt}{t}, (a < 0)$
$d_{ m max}$	Maximum deceleration	m/s^2	$d_{\max} = \max\left(d_{\max}, i = 1, 2, \dots, k\right)$
T_{id}	Time ratio of idling	%	$T_{id} = \frac{t_{id}}{t} \cdot 100$
T_a	Time ratio of acceleration	%	$T_a = \frac{t_a}{t} \cdot 100$
T_d	Time ratio of deceleration	%	$T_d = \frac{t_d}{t} \cdot 100$

4.5.1.2. K-means cluster

The K-means algorithm is a popular choice for handling datasets that have features but no labels. This classic unsupervised learning method has been used for a long time because it is easy to understand and works well [116]. Two important things affect how well the K-means algorithm works. First, the type of distance measurement you choose can greatly influence the clustering results. Second, you need to decide how many clusters you want before using the K-means algorithm [117].

To determine the optimal number of clusters, a combination of evaluation criteria is employed. These criteria include the Calinski-Harabasz index, Davies-Bouldin index, Dunn index, gap index, and silhouette index, each providing a distinct approach to evaluating cluster quality. The Calinski-Harabasz index, in particular, is often favored as it serves as the foundation for many clustering algorithms. This index is a widely accepted measure of cluster validity that calculates the ratio of the between-cluster variance to the within-cluster variance. In simpler terms, it evaluates how well-separated the clusters are from one another compared to how tightly grouped the points are within each cluster [118], A higher Calinski-Harabasz index suggests that the clusters in the model are more distinct and clearly defined [119]. Therefore, the Calinski-Harabasz index is selected as the primary performance metric for evaluation in this context. According to Fig 4.13, the optimal number of clusters for the dataset studied is set as 3.

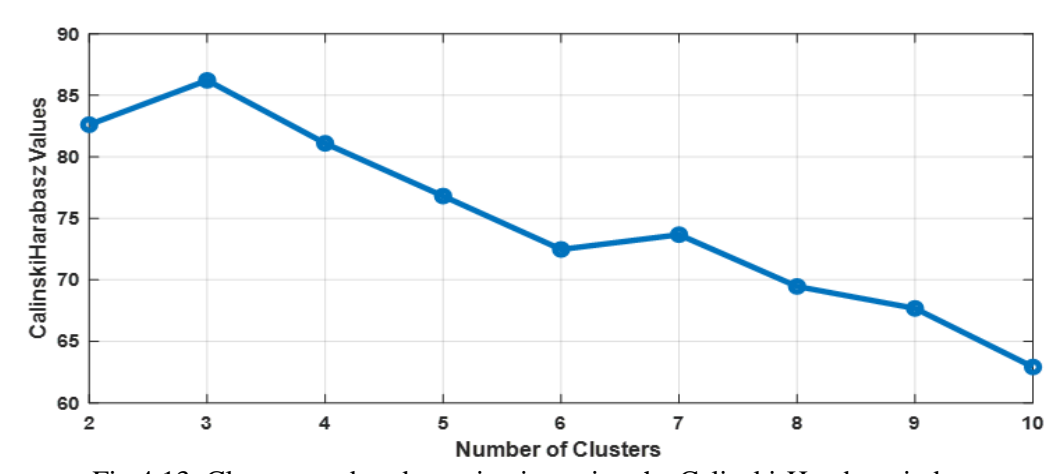


Fig 4.13: Cluster number determination using the Calinski-Harabasz index

With three clusters specified, we applied the k-means clustering algorithm using Cosine distance metrics. This produced the cluster center coordinates, which are summarized in Table 4.3, and the k-means clustering results are shown in Fig 4.14.

Table 4.3: The coordinates of the centroid.

Classes	C1	C2	C3
Centroid	(92.3786, 0.0247, 0.6433)	(42.1502, 0.110, 0.5532)	(15.4591, 0.3412, 0.3840)
coordinates			

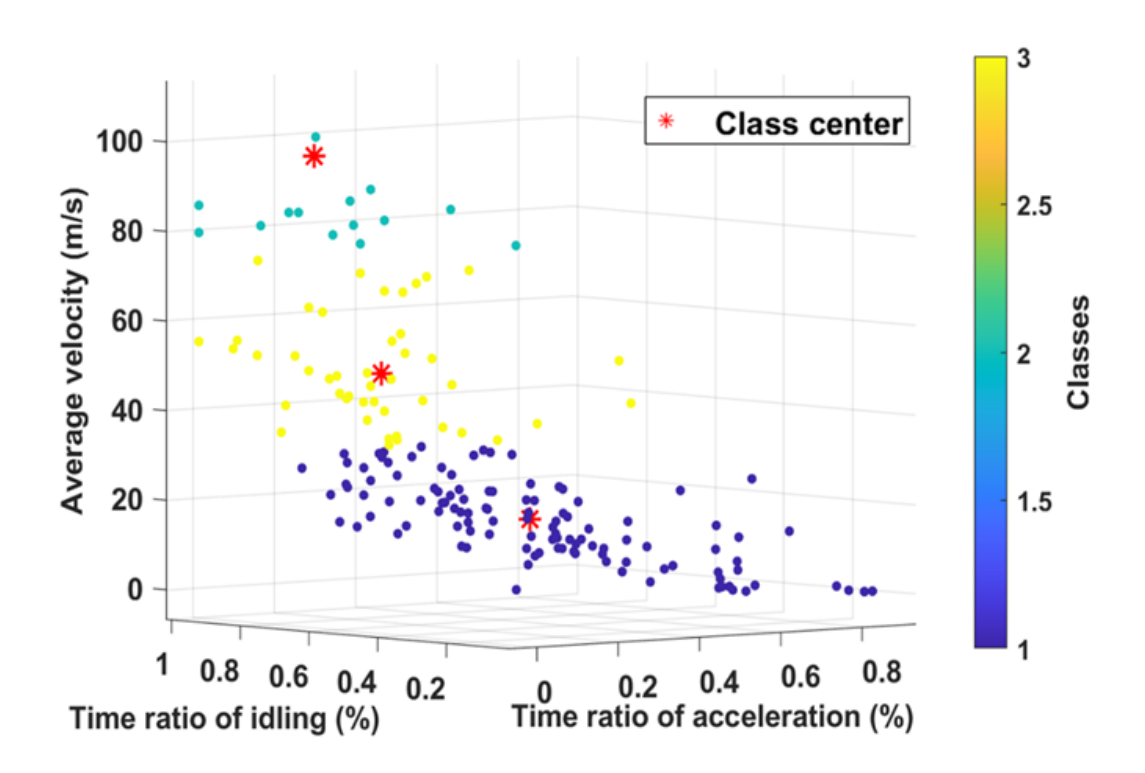


Fig 4.14. Results of K-means clustering.

4.5.1.3. SVM classifier

When dealing with classification problems, Support Vector Machines, a widely recognized supervised machine learning algorithm, are known for their robustness, strong learning abilities, and excellent generalization capabilities [120]. For these reasons, SVM has been chosen in this work as the method to solve classification problems.

SVM uses kernel functions based on input space variables, including linear, polynomial, Gaussian, or radial basis functions, to perform classification. The dataset consists of N-labeled training samples noted as (y_i, χ_i) , where χ_i represents the d-dimensional feature vector of the i^{th} training sample, and y_i takes values within the set (-1,+1) to represent the assigned labels

[121]. The discriminant function $g(\chi)$ of the SVM for the observed data is defined by a mapping $\phi(\chi)$ that corresponds to the chosen kernel function. $g(\chi)$ is provided as:

$$g(\gamma) = w^T \phi(\gamma) + b \tag{4.31}$$

This work deals with a ternary classification task, whereas SVM was originally created for binary classification. Therefore, a One-on-one approach is used [122], which involves training three SVMs to distinguish between each pair of patterns (cl and c2, cland c3, c2 and c3) [123]. Afterward, a majority voting strategy is adopted.

Voting mechanism

The main idea of this voting is to solve an n-class $(C_j, j=1,2,...,n)$ classification problem using m different data sources. For a given sample β , its classification result, denoted as $y_i(\beta) = \{y_{i1}(\beta), y_{i2}(\beta), ..., y_{in}(\beta)\}$ from source $S_i(i=1,2,...,m,j=1,2,...,n)$, is determined by a binary-valued function $y_{ij}(\beta)$.

Let denote $V_j(\beta)$ the number of votes that sample β received for class $(C_j, j = 1, 2, ..., n)$ from the m data sources. Therefore, $V_j(\beta)$ can be computed as follows [124]:

$$V_{j}(\beta) = \sum_{i=1}^{m} y_{ij}(\beta)$$
 (4.32)

Following the majority voting principle, sample β is assigned to the class C_k that receives the highest number of votes, as determined by the equation:

$$C_k = \arg_j \left\{ \max \left\{ V_j(\beta) \right\} \right\}, \quad j = 1, 2, ..., n.$$
 (4.33)

The classification result is determined by the pattern with the highest number of votes. The voter diagram, illustrated in Fig 4.15, uses numerical labels to denote specific driving patterns: 1 represents urban driving patterns, 2 denotes suburban driving patterns, and 3 indicates highway driving patterns.

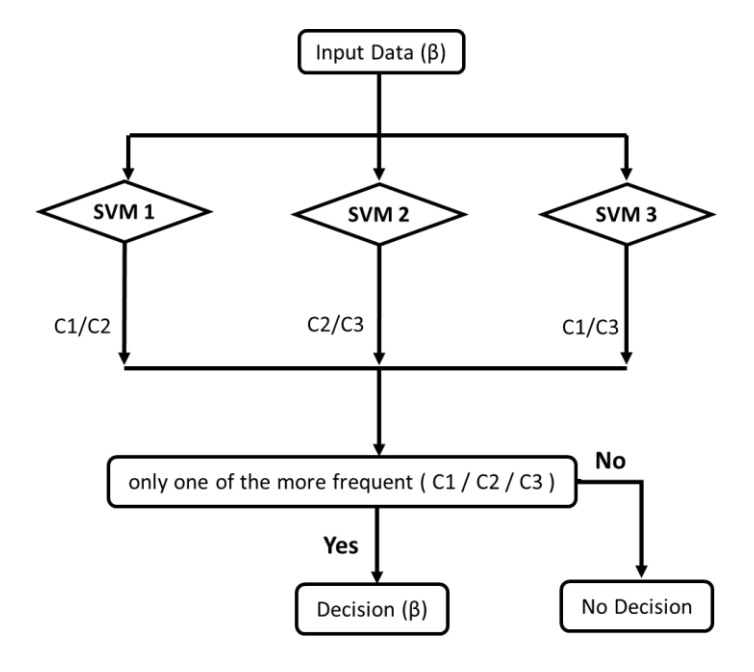


Fig 4.15: Diagram of the voting procedure.

4.5.2. Adaptive wavelet transform

This adaptive approach dynamically adjusts the decomposition level based on the DPR results through an algorithm. Specifically, the decomposition levels correspond to different driving conditions:

- Level 2: This level is applied to urban cycles, where driving is characterized by frequent stops, starts, and lower power requirements. In urban settings, energy demands fluctuate less, and the system adjusts to manage power efficiently with minimal stress on the battery.
- Level 3: This level is suited for suburban driving conditions, which involve moderate speeds
 and fewer stops compared to urban driving. Suburban driving typically requires more
 consistent power delivery, and this level ensures that energy allocation is optimized for these
 mid-range power demands.
- Level 4: This level is used for highway driving, where high-speed travel leads to significant power fluctuations. Highway driving demands more power and results in larger variations in

energy requirements. The system at this level adjusts to accommodate these rapid changes, ensuring efficient power distribution while preventing excessive strain on the battery.

By adapting the decomposition level to the specific driving pattern, the approach not only optimizes energy management but also protects the battery by reducing stress, particularly during high-demand scenarios like highway driving. This dynamic adjustment helps to extend the battery's lifespan by preventing it from undergoing unnecessary strain, thereby contributing to overall system efficiency and longevity.

Table 4.4: Membership symbols

Fuzzy Inputs	Battery current	NB	NM	NS	PS	PM	PB
	Supercapacitor Soc	L		M		Н	
Fuzzy Outputs	change ratio in battery current	NB	NM	NS	PS	PM	PB

NB (negative big), NM (negative medium), NS (negative small), PS (positive small), PM (positive medium), PB (positive big), L(low), M (medium), and H (high)

4.5.3. Adaptive fuzzy

This study involves the development of an AFL controller that considers two key input variables: battery current and the state of charge of the supercapacitor. Given that the battery acts as the primary long-term energy source, its SoC has minimal impact on the overall system's efficiency. The input variables are converted into fuzzy values using specific membership functions, as shown in Fig 4.16 and described in Table 4.4. In particular, the battery current is divided into six membership functions, while the supercapacitor's SoC is represented by three distinct membership functions.

Table 4.5: Fuzzy rules

	If	NB	NM	NS	PS	PM	PB
And							
L		PB	PM	PS	PM	PS	NS
M		PM	PS	PS	PS	NS	NM
Н		PS	NS	NS	NS	NM	NB

Once the inputs are fuzzified, a decision-making inference mechanism applies a rule base informed by experience and heuristic knowledge to generate fuzzy conclusions. The output of the fuzzy controller is the change ratio in battery current, which is used to modify the battery current according to a reference value obtained from the WT. Depending on the controller's decision, guided by the set of fuzzy logic rules outlined in Table 4.5, this adjustment may result in either an increase or decrease in battery current.

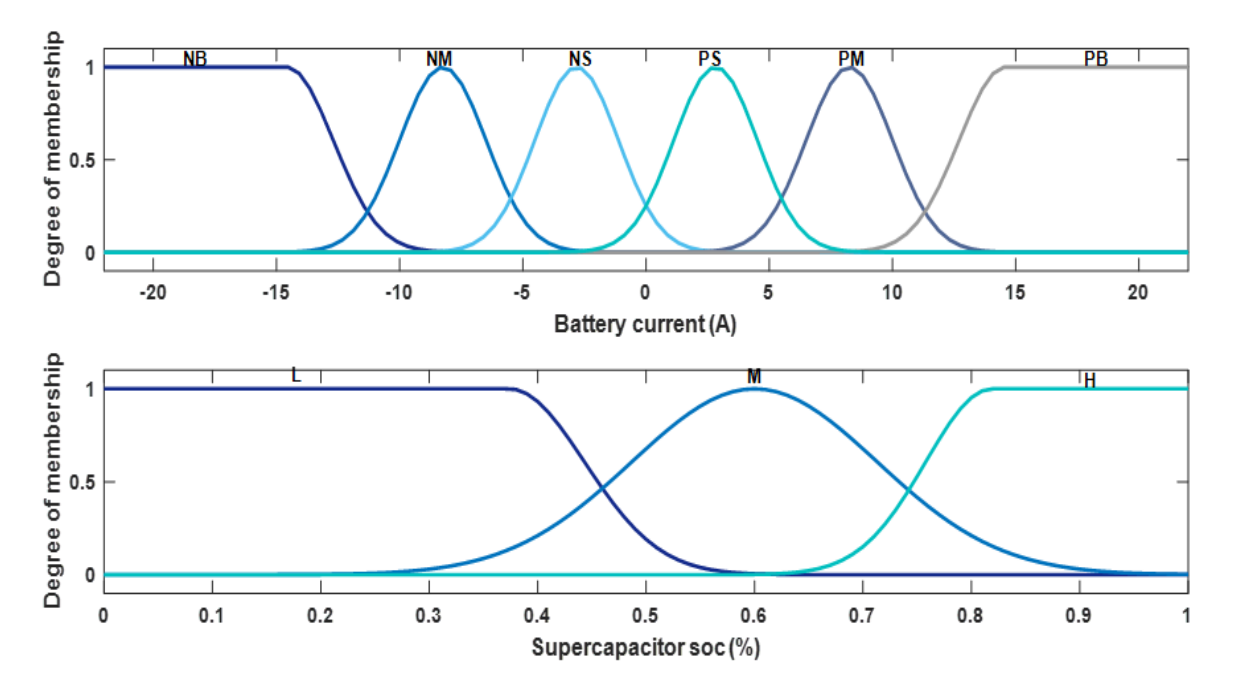


Fig 4.16: Fuzzy logic input membership functions.

It's important to note that the FL controller operates primarily (about 95% of the time) in the positive range of battery current, meaning it mainly manages scenarios where the battery is supplying current (i.e., discharging). This is because the system is generally designed to operate in conditions where the battery powers the DS. However, despite this focus, it is also essential to establish rules for the negative current range to address exceptional or edge cases where the battery might absorb current (i.e., charging). Even though these situations are rare, they must be considered to ensure the controller remains robust and effective under all operating conditions.

Because the output produced by the inference system is inherently fuzzy, it cannot be used directly as a control system signal. Therefore, an essential step is to translate this fuzzy output into a

practical, real-world value. This is achieved through the widely recognized center of gravity (COG) method, which is defined by the following equation [125]:

$$z^* = \frac{\int z.\mu_c(z)dz}{\int \mu_c(z)dz} \tag{4.34}$$

Where $\int \mu_c(z)dz$ indicates the area of the region enclosed by the curve μ_c , and z represents the z-coordinate of the center of gravity.

Six membership functions are defined for the output variable as defined in Table 4.3. If the output values are positive, it indicates that the batteries will supply more power than the reference power obtained from the WT. Conversely, If the output values are negative, it suggests that the batteries will either deliver less power than the reference or require recharging, depending on the change ratio determined by the fuzzy controller.

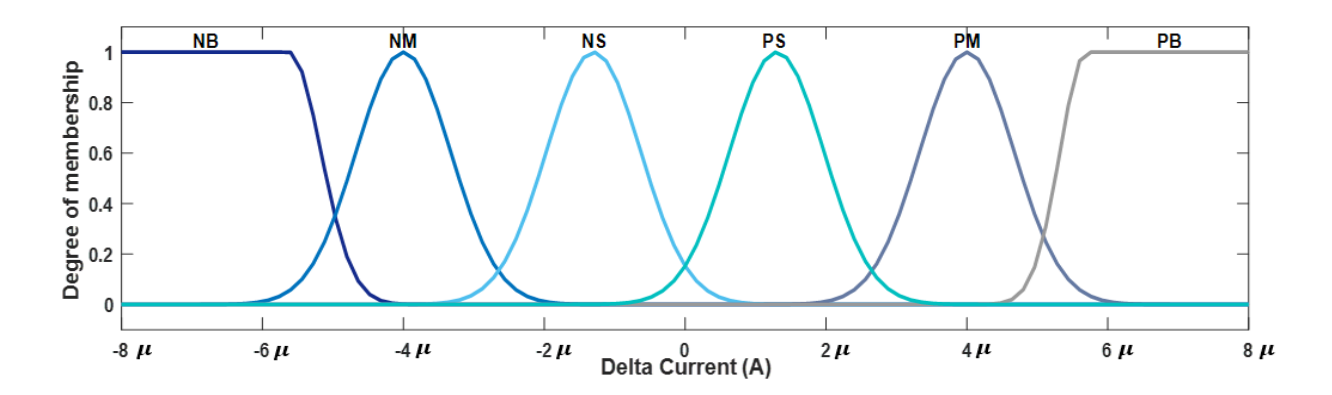


Fig 4.17: The output of adaptive fuzzy logic membership function.

Unlike classical FL, AFL defines the output membership function as adaptive, as illustrated in Fig 4.17. The ability to adjust the μ value introduces adaptivity into the FL system. The decision-making process for the adaptive fuzzy output is shown in Fig 4.18, where the basic concept is the periodic updating of the output membership function based on the recognition results. Additionally, a driving mode detector algorithm is designed to reverse the classification of driving patterns. It acts as a modifier, with 3 indicating urban driving patterns, 2 representing suburban

driving patterns, and 1 corresponding to highway driving patterns. This change is based on the observation that battery current peaks are higher during urban driving compared to highway driving. The factor g_i is selected to define the delta current interval, setting the acceptable range for current variations. A higher value of g_i could result in the cancellation of the battery current, while a lower value might increase the risk of uncontrolled current spikes. Therefore, g_i is crucial in fine-tuning the AFL system's response to changes in driving patterns.

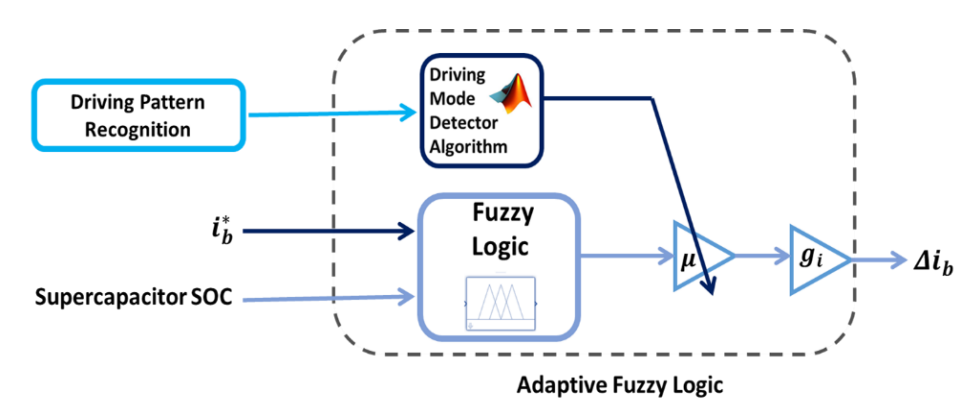


Fig 4.18: Adaptive fuzzy logic controller process

4.6. Traction part control

To replicate the motorization aspect of the VEs, a comparative speed control strategy is proposed for the first motor(M1), utilizing sliding mode theory and back-stepping to follow a reference speed profile. The method yielding the best results will be integrated into the proposed EMSs. Meanwhile, torque control using PI control is implemented in the second motor (M2) to emulate real-world driving conditions.

4.6.1. Speed control based on Sliding mode

Sliding Mode Control works by guiding the system's state to a sliding surface, where the switching function s equals zero. If the state crosses a threshold Δ , the switching control adjusts accordingly to keep the system on track. The goal of SMC is to ensure the system's output follows the desired reference with minimal error. It achieves this through two control modes: reaching mode, which uses a switching control to bring the system to the sliding surface, and sliding mode, which uses

an equivalent control u_{eq} to maintain stability. The control signal is a combination of these modes, where k_{sm} determines the speed of convergence to the sliding surface. To reduce chattering, smooth control actions can be implemented, such as using Eq (4.37), where δ is a small tuning parameter [126].

$$u_{SMC}(t) = u_{eq} + u_{sw} (4.35)$$

$$u_{sw} = k_{sm} \operatorname{sgn}(s) \tag{4.36}$$

$$u_{sw} = k_{sm} \frac{s}{|s| + \delta} \tag{4.37}$$

The transfer function of the PMDC motor can be represented as [127]:

$$\frac{\omega(s)}{v_m(s)} = \frac{k/L_m J}{s^2 + \left\lceil \frac{R_m}{L_m} + \frac{F}{J} \right\rceil s + \frac{R_m F + k^2}{L_m J}} = \frac{2.11 \times 10^5}{s^2 + 519.6772s + 1.59 \times 10^5}$$
(4.38)

In the time domain, Equation (38) can be expressed as:

$$\ddot{\omega}(t) + 519.67 \,\dot{\omega}(t) + 1.59 \times 10^5 \,\omega = 2.11 \times 10^5 \,v_m(t) \tag{4.39}$$

Let's consider

$$x_1 = \omega(t) \quad \text{and} \quad u = v_m(t) \tag{4.40}$$

The system can then be transformed into the canonical form mentioned below:

$$\dot{x}_1 = x_2 \tag{4.41}$$

$$\dot{x}_2 = \ddot{\omega} = -519.67x_2 - 1.59 \times 10^5 x_1 + 2.11 \times 10^5 u \tag{4.42}$$

$$y = x_1 \tag{4.43}$$

The equivalent control and switching control can now be designed, wherein the switching function is given by:

$$s = Ce + \dot{e} = C(\omega_r - \omega) + (\dot{\omega}_r - \dot{\omega}) \tag{4.44}$$

$$\dot{s} = C(\dot{\omega}_r - \dot{\omega}) + (\ddot{\omega}_r - \ddot{\omega}) \tag{4.45}$$

where ω_c is the speed reference and C > 0 is a performance parameter that ensures system stability

[12]. On the sliding surface $s = 0 \rightarrow \dot{s} = 0$

To find the equivalent control, substitute Equation (4.42) into Equation (4.45) with $\dot{s} = 0$

$$C(\dot{\omega}_r - \dot{\omega}) + \ddot{\omega}_r - (-519.67x_2 - 1.59 \times 10^5 x_1 + 2.11 \times 10^5 u) = 0$$
(4.46)

$$C(\dot{\omega}_r - \dot{\omega}) + \ddot{\omega}_r + 519.67\dot{\omega} + 1.59 \times 10^5 \omega - 2.11 \times 10^5 u = 0$$
(4.47)

Since the derivative of the reference signal is zero, Equation (4.47) simplifies to:

$$2.11 \times 10^5 u = 1.59 \times 10^5 \omega + (519.67 - C)\dot{\omega}$$
(4.48)

$$u_{eq} = u = \frac{1}{2.11 \times 10^5} (1.59 \times 10^5 \omega + (519.67 - C)\dot{\omega})$$
(4.49)

To reduce chattering, use the smooth switching control from Equation (4.37). Therefore, the final SMC control signal is:

$$u_{SMC} = \frac{1}{2.11 \times 10^5} (1.59 \times 10^5 \omega + (519.67 - C) \dot{\omega}) + k_{sm} \frac{s}{|s| + \delta}$$
(4.50)

4.6.2. Speed control based on Back-stepping

The basic idea of BS is to first stabilize the initial subsystem using a known stabilizing function through a chosen Lyapunov function. Then, an integrator is added to its input. This method is applied to each subsequent augmented subsystem, continuing in this manner until a global Lyapunov function is obtained. This global function then defines the overall control law that stabilizes the entire system[128].

From the electrical and mechanical equations of the motor explained in Chapter 3, we derive the following equations:

$$\dot{\omega}(t) = -\frac{F}{J}\omega(t) + \frac{k}{J}I_m(t) - \frac{1}{J}C_r(t) \tag{4.51}$$

$$\dot{I}_{m}(t) = -\frac{k}{L_{m}}\Omega(t) - \frac{R_{m}}{L_{m}}I_{m}(t) + \frac{1}{L_{m}}v_{m}(t)$$
(4.52)

we assume ω_{ref} as a desired reference. This leads to the following control error:

$$e_1 = \omega - \omega_{ref} \tag{4.53}$$

$$\dot{e}_1 = \dot{\omega} - \dot{\omega}_{ref}$$

$$= -\frac{F}{J}\omega + \frac{k}{J}I_m - \frac{1}{J}C_r - \dot{\omega}_{ref} \tag{4.54}$$

Thus, the quadratic form of the Lyapunov function V_1 is:

$$V_1 = \frac{1}{2}e_1^2 \tag{4.55}$$

Its temporal derivative is:

$$\dot{V}_1 = e_1 \dot{e}_1 \tag{4.56}$$

$$=e_{1}\left(-\frac{f}{J}\omega+\frac{k}{J}I_{a}-\frac{1}{J}C_{r}-\dot{\omega}_{ref}\right) \tag{4.57}$$

To make \dot{V}_1 negative and ensure stability we take:

$$-\frac{f}{J}\omega + \frac{k}{J}I_{m} - \frac{1}{J}C_{r} - \dot{\omega}_{ref} = -k_{1}e_{1} \qquad (k_{1} > 0)$$
(4.58)

$$\dot{V}_1 = -k_1 e_1^2 \tag{4.59}$$

Then the control law for current is given by:

$$I_{m}^{*} = \frac{F}{k}\omega + \frac{1}{k}C_{r} - \frac{J}{k}\dot{\omega}_{ref} - \frac{k_{1}J}{k}e_{1}$$
(4.60)

Now a new desired reference will be the control variable for the previous subsystem

$$e_2 = I_m - I_m^* (4.61)$$

$$\dot{e}_2 = \dot{I}_m - I_m^* \tag{4.62}$$

$$= -\frac{k}{L_m}\omega - \frac{R_m}{L_m}I_m + \frac{1}{L_m}v_m - I_m^*$$
(4.63)

So the extended Lyapunov function is:

$$V_2 = V_1 + \frac{1}{2}e_2^2 \tag{4.64}$$

$$=\frac{1}{2}(e_1^2+e_2^2) \tag{4.65}$$

$$\dot{V}_{2} = \dot{V}_{1} + e_{2}\dot{e}_{2} \tag{4.66}$$

$$\dot{V}_{2} = -k_{1}e_{1}^{2} + e_{2}\left(-\frac{k}{L_{m}}\omega - \frac{R_{m}}{L_{m}}I_{m} + \frac{1}{L_{m}}v_{m} - I_{m}^{*}\right)$$
(4.67)

To make \dot{V}_2 negative and ensure stability we take:

$$-\frac{k}{L_m}\omega - \frac{R_m}{L_m}I_m + \frac{1}{L_m}v_m - I_m^*)\dot{V}_2 = -k_2e_2 \qquad (k_2 > 0)$$
(4.68)

So, the control law for speed is given by:

$$v_{m} = k\omega + R_{m}I_{m} + L_{m}I_{m}^{*} - k_{2}L_{m}e_{2}$$
(4.69)

This ensures the negativity of the derivative of the extended Lyapunov function:

$$\dot{V}_2 = -k_1 e_1^2 - k_2 e_2^2 \le 0 \tag{4.70}$$

4.6.3. Torque control based on PI controller

The primary responsibility of M1 is to drive the system, serving as the main source of propulsion. It delivers the necessary force to move the system forward or maintain its speed. M2, on the other hand, has a secondary role, interacting with M1 during specific situations like deceleration. M2 is mechanically connected to M1 and electrically to a separate energy source via a DC/DC converter. which ensures the motor receives the precise amount of power required to match the reference torque.

During deceleration, a negative reference torque is required because of the resistive forces applied by the road to the wheels. This negative torque indicates that the system needs to slow down or resist forward motion. In response, M2 must generate torque that opposes the torque produced by M1. This opposition is necessary to achieve effective braking or slowing down of the system. The relationship between these forces and torques is governed by equation (3.29).

In the scenario where motor torque needs to be controlled, Equation (3.32) demonstrates that this can be done directly by managing the motor current. This control is implemented using a PI controller, with its transfer function provided in Equation (4.71). In this equation, $k_{p,m2}$ and $k_{i,m2}$ represent the proportional and integral gains, respectively. The controller's input er is the difference between the desired current I_{m2} and the actual current I_{m2} , as shown in Equation (4.72). The controller's output is the voltage, which must be applied to achieve the desired armature current, and consequently, the desired motor torque[129].

$$PI(s) = \frac{V_{m2}(s)}{er(s)} = k_{p,m2} + \frac{k_{i,m2}}{s}$$
(4.71)

$$er(s) = I_{m2}^{*}(s) - I_{m2}(s)$$
 (4.72)

The current control system is summarized below, where m_2 represents the second motor model:

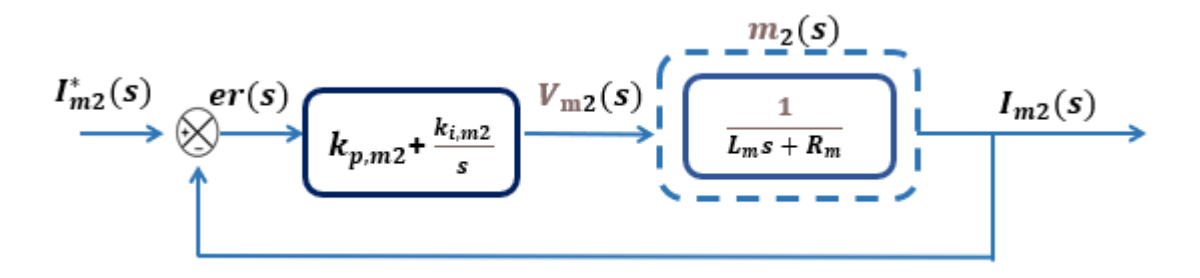


Fig 4.19: PI current control.

The $k_{p,m2}$ and $k_{i,m2}$ values are tuned to achieve the desired transient response. There are several methods to define this desired response. In the time domain, it is common to specify the desired rise time and overshoot for a step input, and the gains are adjusted accordingly to meet these criteria. Alternatively, in the frequency domain, the desired phase margin and cross-over frequency are specified.

4.7. Conclusion

In this chapter, a comprehensive overview of the new EMSs designed for smart power sharing in hybrid systems has been presented. Two adaptive wavelet methods were proposed, each employing distinct adaptation techniques to optimize performance. The chapter also covered the implementation of effective control strategies for the various static converters involved in the system, as well as the control mechanisms to emulate the electric vehicle traction system. The next chapter will delve into the experimental validation of these approaches, providing empirical evidence to support their effectiveness.

Chapter 5

Experimental validation and performance analysis

5.1.Introduction

A considerable effort of this research has been dedicated to creating a test vehicle that includes real-world sources, which will serve as a practical setup for studying power and energy management. This chapter details the experimental validation of the proposed strategy presented in the previous chapter, using a test bench to implement control laws within a software environment based on Matlab/Simulink, supported by a dSPACE DS 1104 board. The offline nature of the proposed methods adds complexity to the experimental implementation. However, the significance of testing and improving the strategy in real-world conditions is highlighted by the experimental results, which are used to evaluate the performance of the system and the different control algorithms.

5.2.Description of the test bench

A small-scale experimental test bench has been established to implement and validate the proposed strategies, as appears in Fig 5.1. The test bench is made up of:

- An EPS with two sources, a primary source consisting of five LiFePO4 batteries connected in series, and a secondary source using a Maxwell supercapacitor module with a capacity of 165 Farads. Each power source was connected to two separate arms of the SEMIKRON converter through a filter that included an inductor with specifications of 30mH and 0.9Ω.
- A DS emulator was created by assigning a third arm to a 24V PMDC motor, which is speedcontrolled to simulate the traction of an EV. Another SEMIKRON converter is used to control the torque of a second DC motor, identical to the first one, to emulate road driving conditions.

The system uses LA25NP and LV25P Hall sensors to measure various currents and voltages precisely. Also, a tacho generator with a sensitivity of 1 V per 1000 rpm is used to measure motor speed. System control is achieved using a dSPACE DS1104 prototyping tool combined with MATLAB® Simulink®. The Real-Time Interface (RTI) facilitates the transfer of applications to a microprocessor-based control system. The dSPACE card is connected via the PC's PCI port, while an interface card adapts the control signals for the power converters. Further details about the system components are provided in Table 5.1.

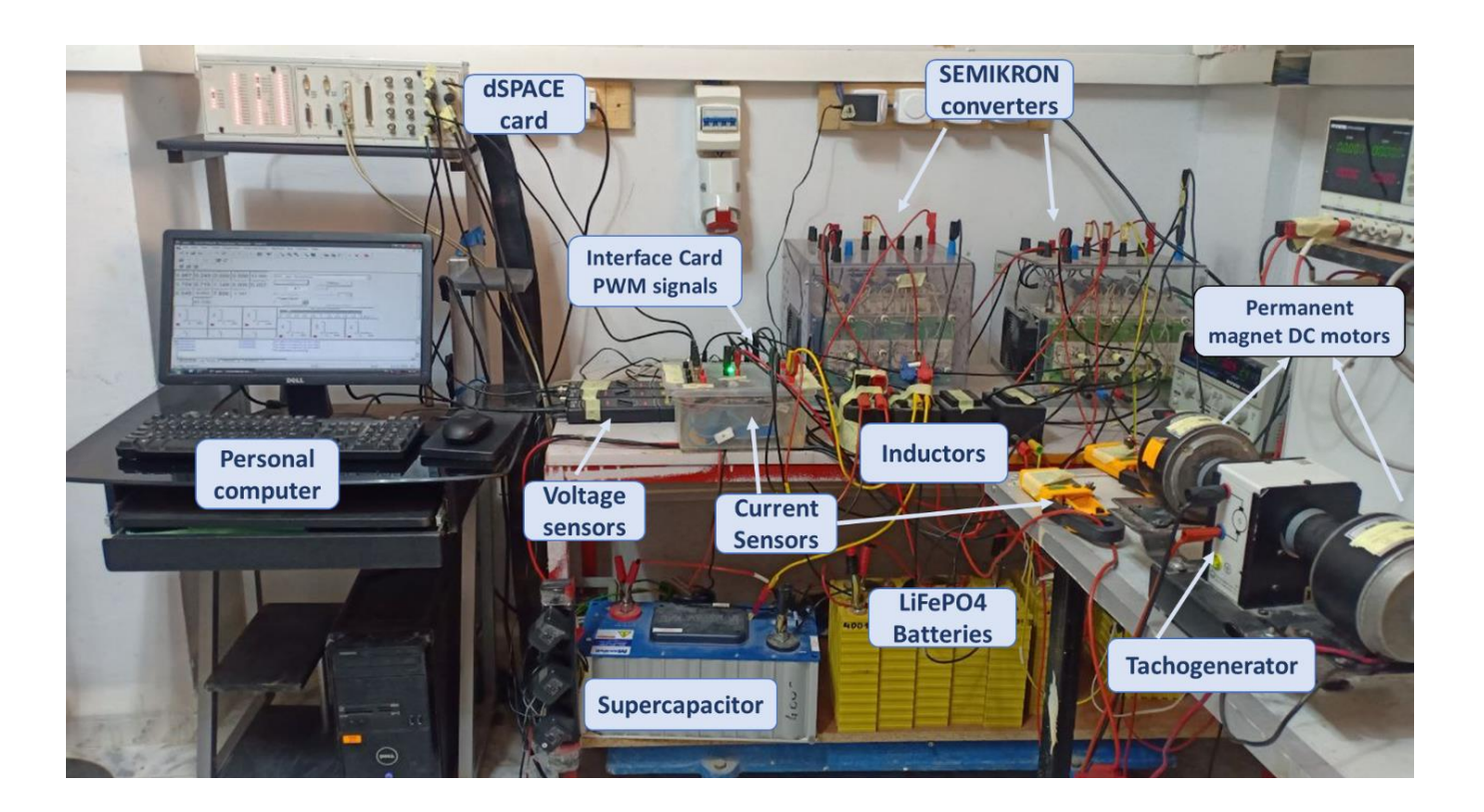


Fig 5.1: Experimental bench.

Table 5.1: Hardware characteristics

Battery	Model name	TSWB-LYP100AHA(B)
	pack Nominal voltage (v)	LiFeYPO4
	Pack Capacity (Ah)	3.3
	Pack Energy (wh)	100
	Pack Internal Resistance (m Ω)	330
	Pack Weight (kg)	0.45
		3.6
Supercapacitor	Model name	BMOD0165
	pack Nominal voltage (v)	48
	Pack Capacity (F)	165
	Pack Energy (wh)	53
	Pack Internal Resistance (m Ω)	6.3
	Pack Weight (kg)	13.5
Dc motor	Model	MY1016
	Supply Voltage (v)	24
	Output power (w)	250
	Rated Current (A)	14
	Rated Speed (RPM)	2750

5.2.1. DSPACE dS1104 Card

The dSPACE DS1104 Controller card is a standard board with a real-time processor that can be installed in a personal computer with a 5V PCI slot. According to Fig 5.2, the DS1104 includes [130]:

- 4 inputs connected to a 16-bit analog-to-digital converter (ADC), 4 inputs with separate 12-bit ADCs, and an 8-output digital-to-analog converter (DAC).
- 2 incremental encoders.
- Onboard 64-bit floating-point processor running at 250 MHz.
- Onboard Slave DSP based on the TMS320F240 DSP microcontroller.
- Onboard memory.
- Additional digital input/output capabilities.

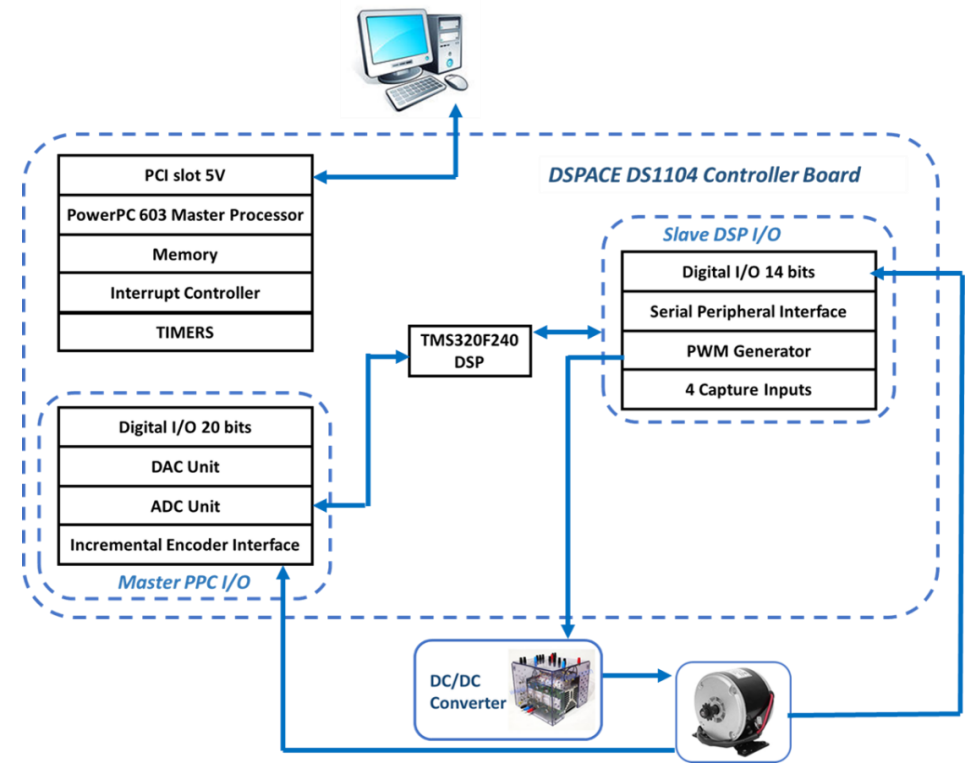


Fig 5.2: Structure of the dSPACE DS1104 controller board.

The integration of dSPACE with Simulink/Matlab software creates a powerful development environment. With Real-Time Interface (RTI), function models can be easily run on the dSPACE system. The process involves generating the model code using Simulink Coder, after which the

real-time simulated model is compiled, downloaded, and automatically started [131]. The connector panel links all system I/O signals to the DS1104, as shown in Fig. 5.3.

To configure these inputs and outputs of the control system graphically, ControlDesk software can be used, which offers all the tools needed to control and monitor experiments through graphical user interfaces, making it easier to develop controllers. To clarify more, ControlDesk allows users to design graphical layouts with diverse control elements. This platform facilitates real-time control and monitoring of parameters while also providing access to I/O signals linked to the hardware. [132].



Fig 5.3: The connector panel of DS1104 Card.

5.2.2. SEMIKRON Converter

The SEMIKRON converter is an advanced power electronics system designed to control and regulate high-voltage power precisely. It uses SKHI22 driver cards to manage voltage levels at 0V and 15V for each bridge arm. The driver in an IGBT system is essential for controlling the SKM50GB123 IGBT power modules and ensuring the safety of both the system and the user through segregation between the low and high-power sections of the converter. Its key functions include amplifying ON/OFF logic signals to deliver high peak currents for switching, monitoring errors like under-voltage and short circuits, and isolating the primary circuit from the high-power secondary circuit. This isolation prevents dangerous interactions while allowing the safe transmission of control signals, ensuring reliable performance and protection. The drivers use three SKHI 22 A-R cores, each controlling an inverter leg with both "Top" and "Bottom" IGBTs of a single module. The drivers require a 0/15V power supply with a maximum current consumption of 160 mA per driver. They operate with a negative logic error signal, outputting +15V when no errors are detected. In case of a fault, the driver stops, ignores input pulses, and resets the error

latch after resolving the issue. Each driver operates independently; safety precautions are necessary to handle error conditions[133].

The IGBT gate control circuit operates with 0/15V logic signals, while the dSPACE port outputs are in TTL format (0/5V). Therefore, to enable the inverter switches to be locked and adapt the control signal levels to match the IGBT gate voltage, an interface board was designed to align the dSPACE output with the inverter input logic levels. This board includes a buffering circuit using 74LS00 NAND gates to ensure reducing damage in case of inverter malfunction, this buffering circuit is cascaded by a voltage step-up stage using the 74LS17 circuit, comprising six open collector inverters.

5.2.3. Sensors

The current and voltage measurements shown in Fig 5.4 are performed using the LEM LA25-NP and LEM LV25P circuits, respectively. These sensors utilize the magnetic fields generated by electric currents to provide high accuracy and a broad dynamic range. A 4th-order Shpychev low-pass filter is employed to reduce noise, ensuring that the measurement signals are clean and reliable before being used in control algorithms. Gain adjustments are essential to align the sensor output with the input range of the analog-to-digital converter, ensuring accurate digital representation of the measured signals [134]. Additionally, speed is measured using a tachogenerator with a sensitivity of 1 V/1000 rpm. This is a direct current generator that produces an output voltage proportional to the RPM. It is connected to the machine via a clutch, as seen in Fig 5.4(c).



Fig 5.4.: Sensors: (a) Current sensor; (b) Voltage sensor; (c) A tachogenerator.

5.3. Experimental validation

The experimental study was carried out using the dedicated test bench, divided into two phases with different driving cycles. In the first phase, an AWT method based on the supercapacitor soc was implemented. This method was compared with three other frequency-based techniques: a fixed cut-off frequency, an adaptive filter, and the conventional WT. In this phase, the regenerative braking process was not considered.

In contrast, the second phase focused on applying the method developed in the previous chapter, which is based on Adaptive Wavelet-Adaptive Fuzzy Logic based K-Means-SVM Pattern Recognition. Here, attention was given to the regenerative braking phase, emulating the behavior of a real EV system where energy is recovered during braking. Various performance criteria were adopted to assess the effectiveness of the proposed EMS methods and determine how well each one managed energy under different driving conditions.

5.3.1. Adaptive wavelet-based strategy

In this part, a custom driving cycle is generated by randomly merging two standard driving cycles: HWFET (400 -500 s) and WLTP class 2(990-1140s), each with an average duration of 150 seconds. These selected cycles represent a variety of road conditions, including highways, suburban roads, and urban environments, providing a wide range of current load frequencies for the vehicle traction system. Then, this custom driving cycle is used in equation (3.28) to extract the mechanical power profile which is used as a speed profile.

Before selecting the most suitable speed control method for tracking the reference speed, an experiment was carried out using two speed profiles to compare the performance of the SM and BS controllers. The goal was to evaluate how effectively each controller tracks the desired speed. The results, displayed in Fig 5.5 indicate that the BS method significantly outperformed the alternative controller in terms of response accuracy and stability

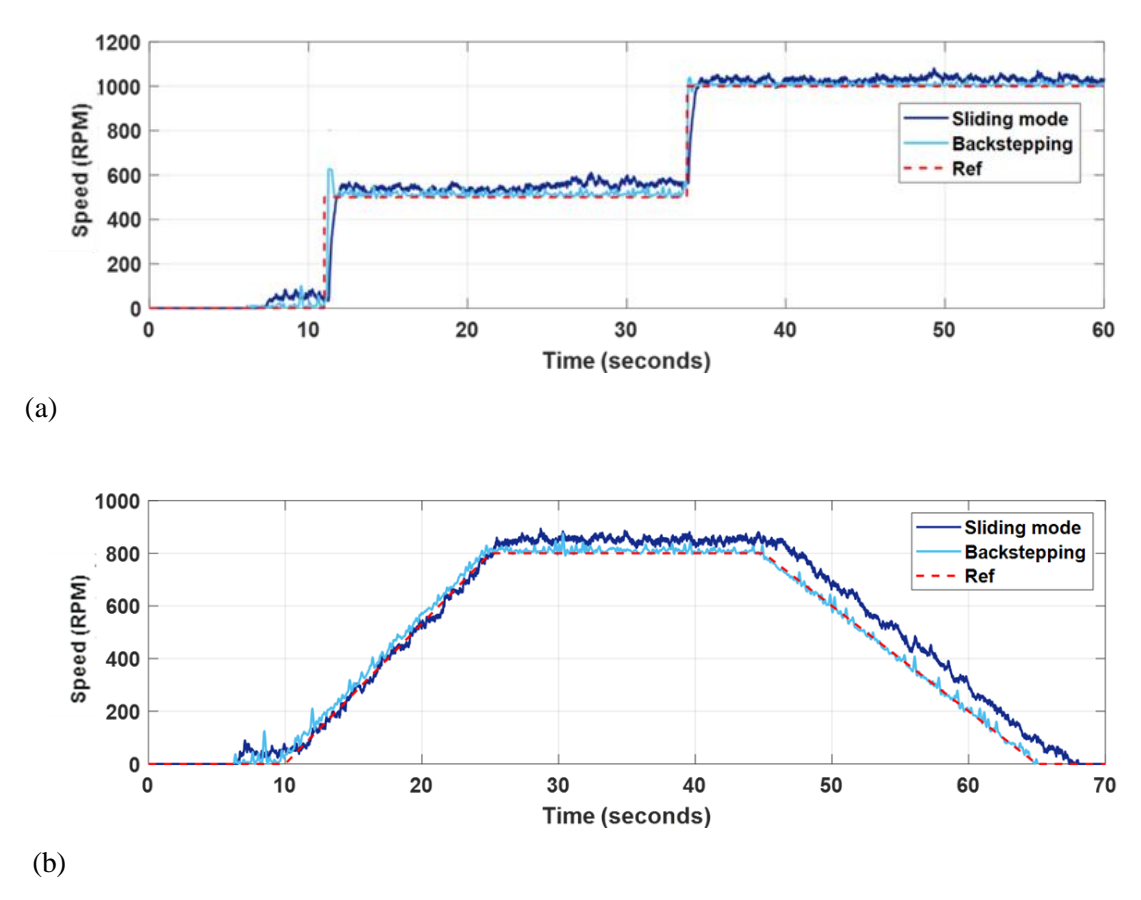


Fig 5.5: Speed tracking performance: (a) Profile 1; (b) Profile 2.

Then, this approach was applied using the driving cycle cited previously. Results can be found in Fig 5.6 with almost no overshoot and negligible static error.

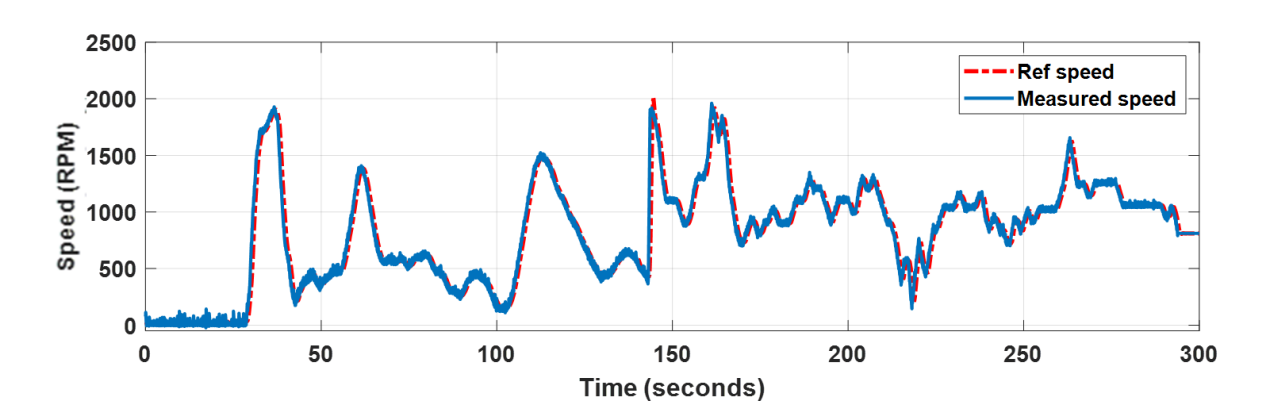
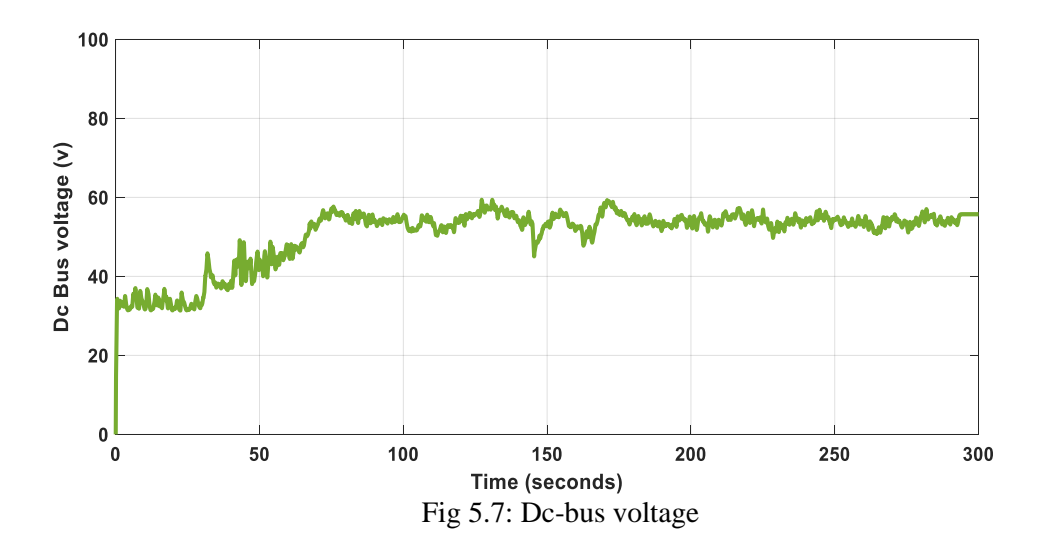
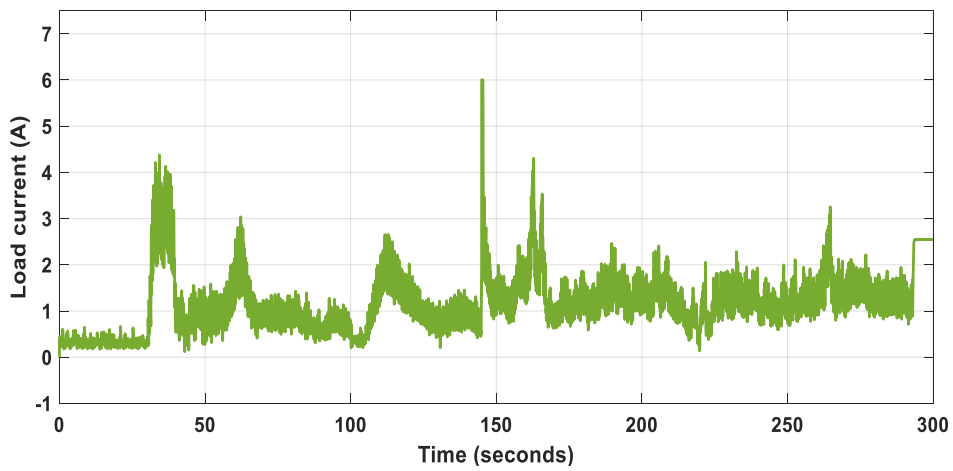


Fig 5.6: Motor speed.

A Lyapunov control system is used to regulate the DC-link voltage, enabling currents to be treated as control variables and viewed as an image of power transferred from the EPS to the DS. The results in Fig. 5.7 demonstrate that the DC bus remains regulated around its reference v_{dc-ref} .



The load current in Fig. 5.8 takes the same shape as the speed profile, reflecting a signal with the same frequency spectrum as the speed profile. Since the proposed strategy relies on frequency, this profile requires a frequency analysis, revealing three different sections with varying frequencies, caused by using different driving patterns. The FFT analysis results presented in Fig 5.9 show key frequencies of 0.01 Hz for the first section (Fig 5.9(a)), 0.06 Hz for the second section (Fig 5.9(b)), and 0.03 Hz for the third section (Fig 5.9(c)). These frequencies match urban, high-speed, and suburban driving patterns, respectively.



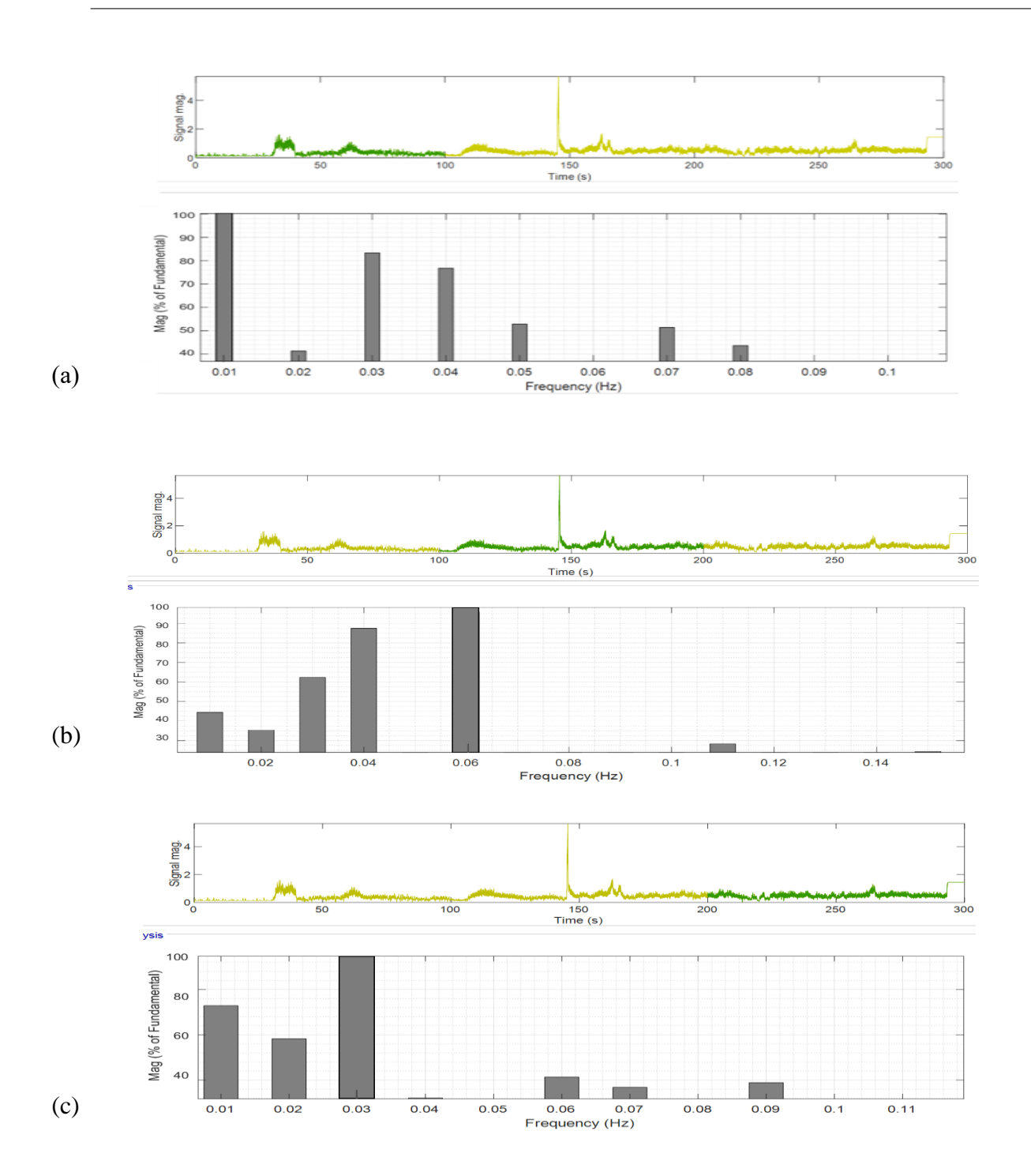


Fig 5.9. Load current FFT analysis: (a) Section 1 (green) load current during urban driving cycle; (b) Section 2 (green) load current during high-speed driving cycle; (c) Section 3 (green) load current during suburban driving cycle.

In order to evaluate the effectiveness of the proposed method, it was compared with three other frequency-based techniques: a fixed cut-off frequency, an adaptive filter, and the conventional wavelet transform. The comparison focused on battery and supercapacitor currents as well as their state of charge.

Figs 5.10(a) and 5.10(b) illustrate changes in battery and supercapacitor currents when using fixed and adaptive cut-off frequencies for frequency separation. As the cut-off frequency increases from 0.01 Hz to 0.06 Hz, the battery current shows greater fluctuations, while the supercapacitor current becomes more stable. This demonstrates the supercapacitor's effectiveness in handling fluctuations, as reflected by the higher state of charge for the batteries and the lower one for the supercapacitor shown in Figs 5.11(a) and 5.11(b). The adaptive frequency separation method proves to be the most effective in managing high-frequency components while maintaining a stable supercapacitor current.

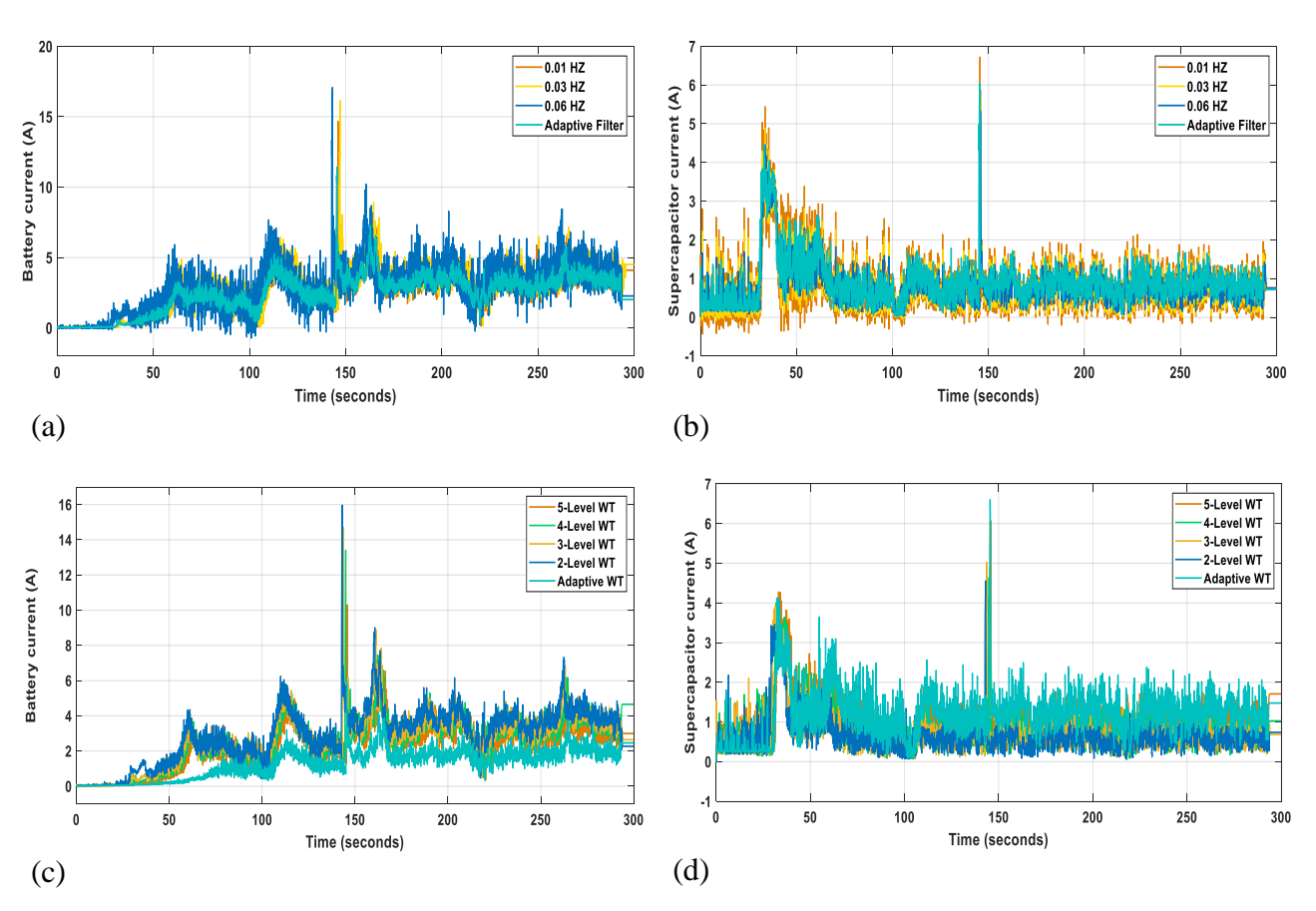


Fig 5.10. Currents of batteries and supercapacitors using tested techniques: (a) Battery current over various cut-off frequencies; (b) Current of the supercapacitor with various cut-off frequencies; (c) Battery current

with different wavelet levels and the adaptive method; (d) Current of the supercapacitor with different wavelet levels and the adaptive technique.

The analysis also explores the WT method using different decomposition levels (2, 3, 4, and 5) and an adaptive approach, Figs 5.10(c) and 5.10(d) show battery and supercapacitor current under these different levels. Higher levels result in more rapid changes in battery current and frequent power exchanges, while higher levels filter out high-frequency components in supercapacitor current, reducing those fluctuations. AWT method performs best at managing high-frequency components while keeping the supercapacitor current stable. This appears through the analysis of the State of Charge curves in Figs 5.11 (c), and 5.11 (d) where high wavelet decomposition levels introduce smoother changes and more balanced energy flow in the SoC curves for the battery. Conversely, they lead to greater dynamics and fluctuations in the supercapacitor Soc.

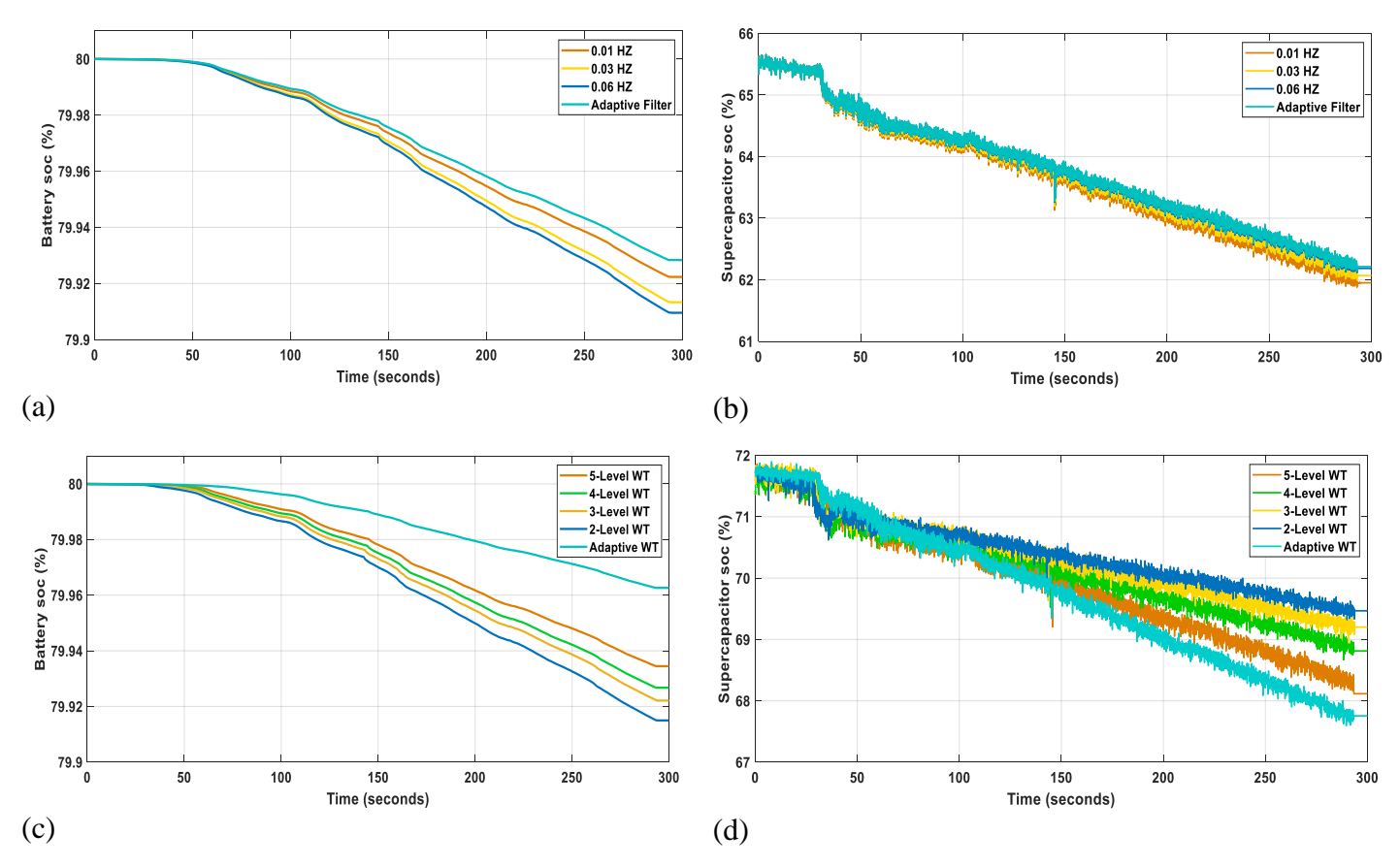


Fig 5.11. State of charge of Battery and supercapacitor under validated techniques:(a) Variations in battery SoC at various cut-off frequencies;(b) Variations in supercapacitor SoC at various cut-off frequencies;(c) Battery SoC at various wavelet levels and adaptive method;(d) Supercapacitor SoC at varying wavelet levels and the adaptive technique.

Depending on the application's particular requirements, frequency separation and wavelet transform approaches each have unique benefits and trade-offs. Adaptive strategies are highly effective at managing energy precisely and maintaining the stability of both battery current and State of Charge. However, selecting the optimal approach requires considering additional criteria, particularly when aiming to extend battery life. Battery current RMS and peaks are important indicators of aging and provide valuable insights into battery health and performance. Another key aspect is system losses, as reducing these losses can greatly affect the battery's lifespan. These considerations are discussed below:

Current Root Mean Square (RMS)

The Root Mean Square current serves as an important evaluation metric in EMSs for HESS. It offers key insights into system performance and the strain imposed on the energy storage components, especially batteries. The significance of RMS lies in its ability to evaluate the smoothness and stability of current flows, which directly influence the lifespan and reliability of these storage devices. RMS may be computed using the following formula:

$$I_{RMS} = i_{rms-b} + i_{rms-sc} \tag{5.1}$$

$$I_{RMS} = \frac{1}{N} \left(\sqrt{\sum_{b-mes_i}} + \sqrt{\sum_{c-mes_i}} \right)$$
(5.2)

Fig 5.12 proves the ability of AWT method to lower the total RMS current. The current dropped to 2.81 A; a 34% decrease compared to the fixed cut-off frequency method. This improvement allows for smoother power transfer, less battery stress, and prolongs component lifespan, contributing to better system stability. The conventional WT method also reduces RMS current to values between 3.7 A and 3.9 A, representing a decrease of 9.36% to 14.63% compared to the fixed cut-off frequency range of 4.04 A to 4.34 A, demonstrating its capability in controlling current variations. Although the adaptive filter reduces RMS current to around 4 A, showing improved handling of fluctuations over the fixed cut-off frequency method, it does not match the precision of the AWT. The fixed cut-off frequency method, which produces high RMS current values, poses concerns regarding increased stress on energy storage components and its effect on battery longevity. Therefore, the AWT method proves to be the most effective solution for

optimizing energy management and safeguarding components in the HESS. This makes it the preferred choice for maintaining reliable performance.

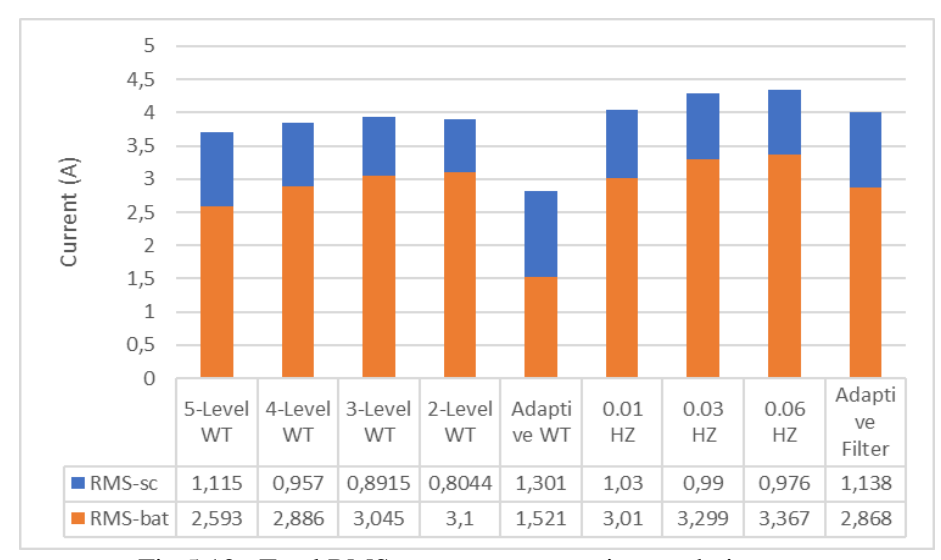


Fig 5.12: Total RMS current across various techniques

> Maximum current

Reducing the maximum current in an EMS for HESSs is crucial. This value indicates the highest instantaneous current provided by the battery and supercapacitor during operation. High peak currents may put enormous pressure on these energy storage elements, accelerating their failure and reducing their lifespan. Furthermore, high peak currents can cause drops in voltage, energy loss, and instability in the system.

Examining the maximum current criterion shown in Fig 5.13 demonstrates that the AWT approach excels at lowering peak currents to 12.58 A, which is essential for smoother power delivery and minimizing battery stress. The current profile obtained using the adaptive wavelet approach indicate longer component life and enhanced system stability, reducing the probabilities of premature failure and expensive repairs. In contrast, other methods exhibit higher peak currents: 16.36 A to 20.46 A for the conventional WT, 21 A for the adaptive filter, and 21.7 A to 22.68 A for the fixed cut-off frequency. These elevated currents can accelerate the aging of energy storage components, resulting in inefficiencies and safety problems. Thus, the AWT method effectively minimizes peak current values, making it a strong alternative for EMSs in EVs. Its ability to reduce

maximum currents plays a key role in optimizing energy management, ensuring the long-term health of the HESS, and protecting components.

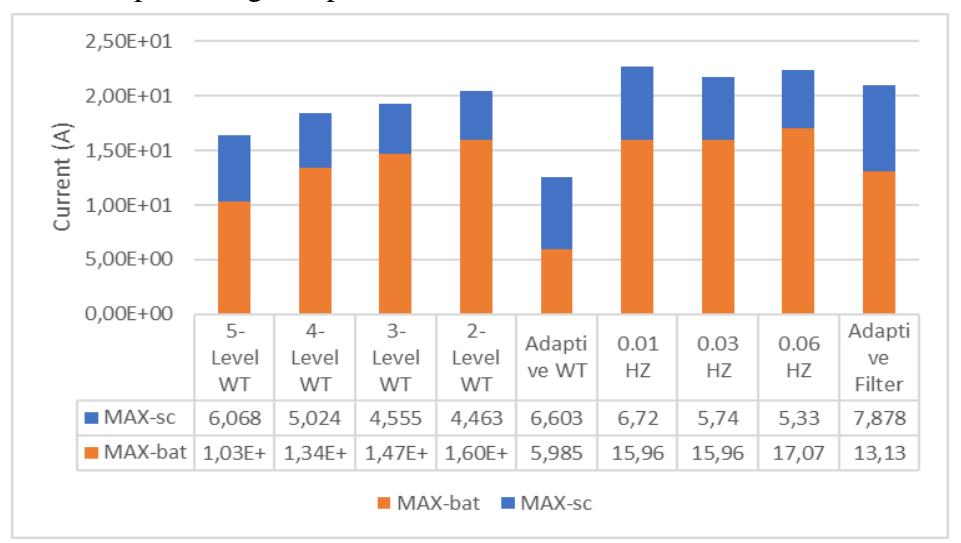


Fig 5.13: The total maximum current with different techniques

\triangleright The Delta State of Charge (\triangle SoC)

This criterion quantifies variations in SoC over time and offers valuable data about energy consumption efficiency. Reducing the Delta SoC is important for achieving balanced energy sharing between the battery and supercapacitor, reducing excessive discharge cycles, and enhancing the use of storage system.

Fig 5.14 illustrates the ability of the AWT method to lower the total Delta SoC to 30%, demonstrating its precise control and efficient energy distribution for a more stable SoC profile. In comparison, other methods show higher Delta SoC values: 20.2% to 24.1% for the conventional WT, 19.6% for the adaptive filter, and 9.2% to 14.6% for the fixed cut-off frequency method. Elevated Delta SoC values signify less efficient energy sharing and imbalances between the battery and supercapacitor. Large and frequent SoC fluctuations can accelerate degradation, reduce capacity, and shorten battery lifespan. The AWT method successfully reduces Delta SoC, emphasizing its role in optimizing energy use and maintaining the long-term health and reliability of the HESS.

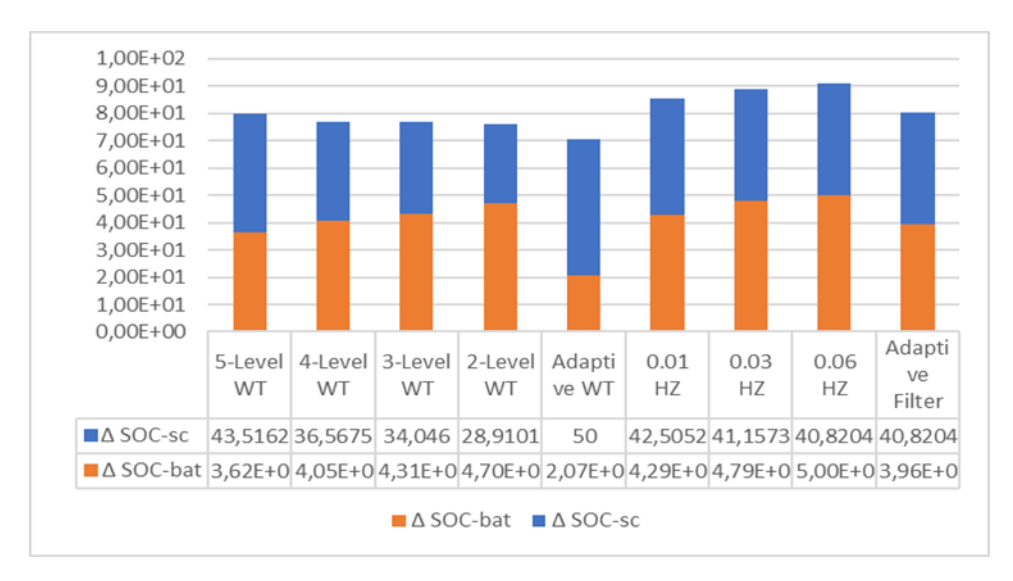


Fig 5.14: Delta SOC with various techniques.

> losses

The losses in EMSs have a direct impact on system efficiency and energy usage. Limiting losses is important for achieving better energy conversion efficiency, less energy waste, and improved performance of the Hybrid Energy Storage System. Battery and supercapacitor losses can be stated as [135]:

$$L_T = L_b + L_{sc} \tag{5.3}$$

$$L_T = \left(R_b \times i_{b-mes}^2\right) + \left(R_{sc} \times i_{sc-mes}^2\right) \tag{5.4}$$

$$L_T(\%) = \frac{L_T}{L_{T-\text{max}}} \tag{5.5}$$

Fig 5.15 shows that the adaptive wavelet method achieves the lowest energy losses, at just 20.40% of the total losses related to the fixed cut-off frequency EMS. This demonstrates the good performance of the AWT in optimizing power flow and minimizing energy waste. In comparison, the conventional WT approach has a bit more losses, ranging from 59.30% to 84.76% depending on the decomposition level, whereas the adaptive filter method has even greater losses, at 72.55%. The ability of the AWT strategy to attain the lowest losses is a major advantage, resulting in greater energy efficiency, less heat generation, and a longer lifespan for energy storage devices. As well as Lower losses contribute to increased system reliability and economic viability.

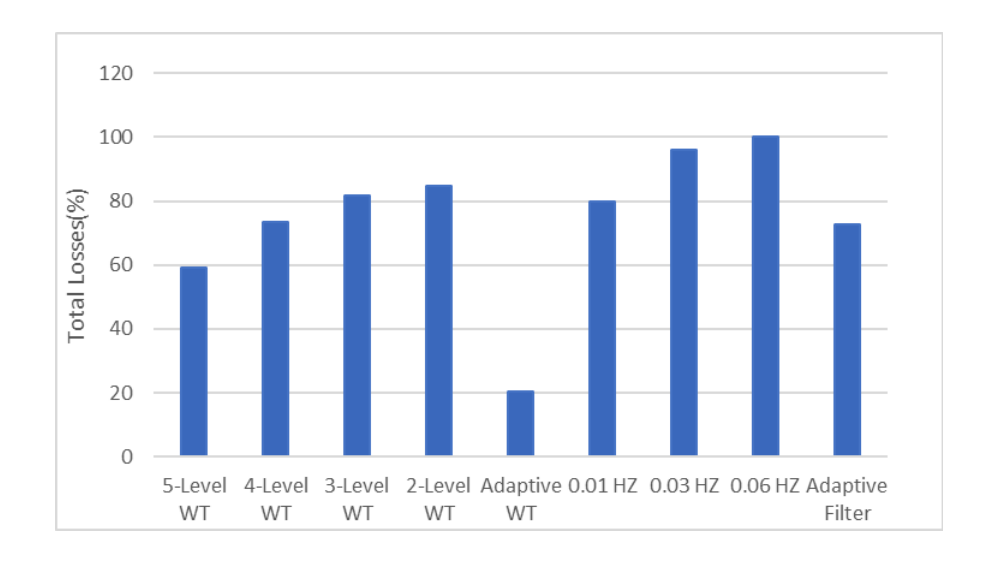


Fig 5.15: Total Losses under different techniques implementation

The results obtained using the above mentioned criteria can be summarized in Table 5.2 as follows:

Table 5.2: Detailed evaluation of the suggested EMS, the standard wavelet approach, and the adaptive filter compared to a fixed cut-off frequency

Criteria	Proposed EMS	Wavelet-based EMS	Adaptive Filter
Total RMS current	66%	85.37% -90.64%	87%
Total maximum current	55.47%	72.14% -90.22%	92.60%
Δ soc	70%	75.9% -79.8%	80.4%
Total Losses	20.40%	59.30% -84.76%	72.55%

In the existing literature, EMS comparisons typically contrasted fixed cut-off frequencies with adaptive ones or the traditional WT to the AWT. In this part, four different approaches are tested under the same experimental conditions to assess their performance, making the comparison more technical and detailed. Table 5.3 shows the obtained comparative results as well as selected comparisons from the literature. The numerical results show that the adaptive techniques regularly outperform their fixed versions in terms of battery RMS current, peak power, longevity, maximum current, and losses. Notably, the proposed EMS, which has been experimentally compared with the conventional WT, adaptive filter, and fixed cut-off frequencies in this work, proves to be of special significance.

Table 5.3: Comparison of Frequency-Based EMS Performance for Both Classical and Adaptive Versions.

Reference	Comparison method	Finding
[136]	Adaptive Filter Vs fixed cut-off frequency	Battery RMS current: Reduction by 17.03% Battery peak power: Diminution by 3.71% Battery lifespan: Improvement by 32.40%
[137]	Adaptive Filter Vs fixed cut-off frequency	Battery RMS current: Reduction by 14% and 55% for NEDC and urban Artemis cycle
[138]	Adaptive wavelet vs conventional wavelet	Battery maximum current: Minimization by 58.2% Battery lifespan: Enhancement by: 6.16%
[135]	Adaptive wavelet vs conventional wavelet	Losses: Diminution by 10.66%
Proposed	Proposed adaptive wavelet, conventional	Total RMS current: Reduction by 34%,
EMS	wavelet, and adaptive Filter Vs fixed cut-off	9.36% -14.63% and 13%
	frequency	Total maximum current: Lowering by 44.53%, 27.86% -9.78% and 7.40%
		Losses: Minimization by 79.6%, 15.24% -
		40.7% and 27.45%

5.3.1. Adaptive Fuzzy Logic based K-Means-SVM Pattern Recognition strategy

During the second experimental phase, a developed adaptive wavelet was validated considering driving conditions. Therefore, K-Means-SVM drive Pattern Recognition was adopted as an important part of this EMS. Table 5.4 shows comparative results from the literature where K-Means and SVM outperformed their alternatives. The validity of this recognizer was tested by applying the first 500 seconds of the FTP72 standard driving cycle which includes a mix of urban, suburban, and highway driving environments. The recognition process results are shown in Fig 5.16 by the blue line where 1 represents urban driving patterns, 2 corresponds to suburban driving patterns, and 3 indicates highway driving patterns. The outcome demonstrates that the developed driving pattern recognizer can accurately identify different driving patterns, confirming the effectiveness of the k-means-SVM recognizer.

Table 5.4: Accuracy comparison of diverse machine learning techniques in Driving state recognition

	Methods	Accuracy	Reference
Clustering	K-means, Fuzzy C-means, K-	K-means 97.84%	[139]
	medoids, GMM	Fuzzy C-means 97.12%	
		K-medoids 96.82%	
		GMM 96.29%	
Classification	SVM, KNN, RF	SVM 67.4%	[140]
		KNN 66.8%,	
		RF 81.3%	
SVM, KNN, Linear	Linear SVM 95.51%	[141]	
	Discriminant	Coarse Gaussian SVM 91.02%	
		Quadratic SVM 89.79%	
		Medium Gaussian SVM 85.47%	
		Fine Gaussian SVM 85.25%	
		Cubic SVM 67.16%	
		KNN 92.3%	
		Linear Discriminant 90.6%	

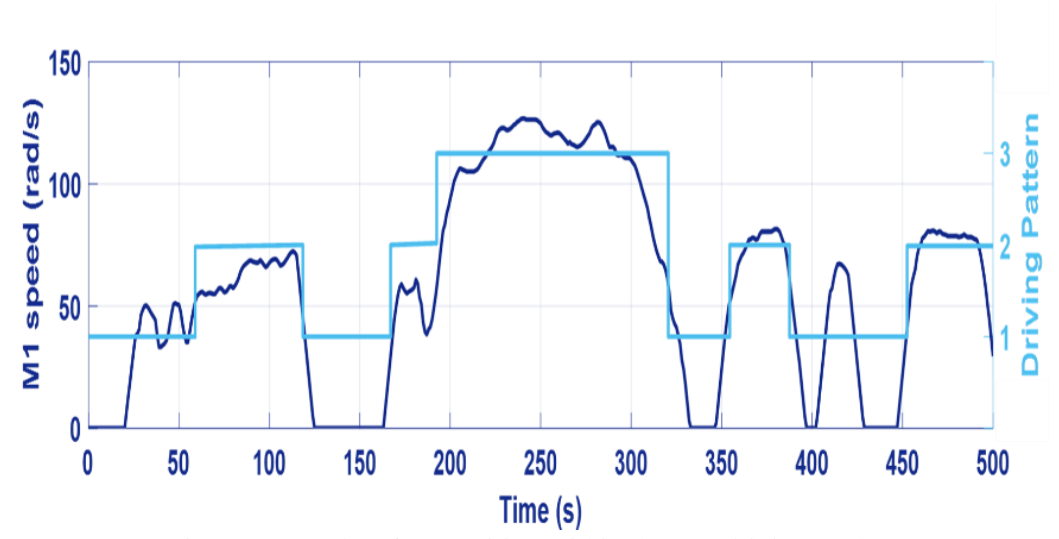
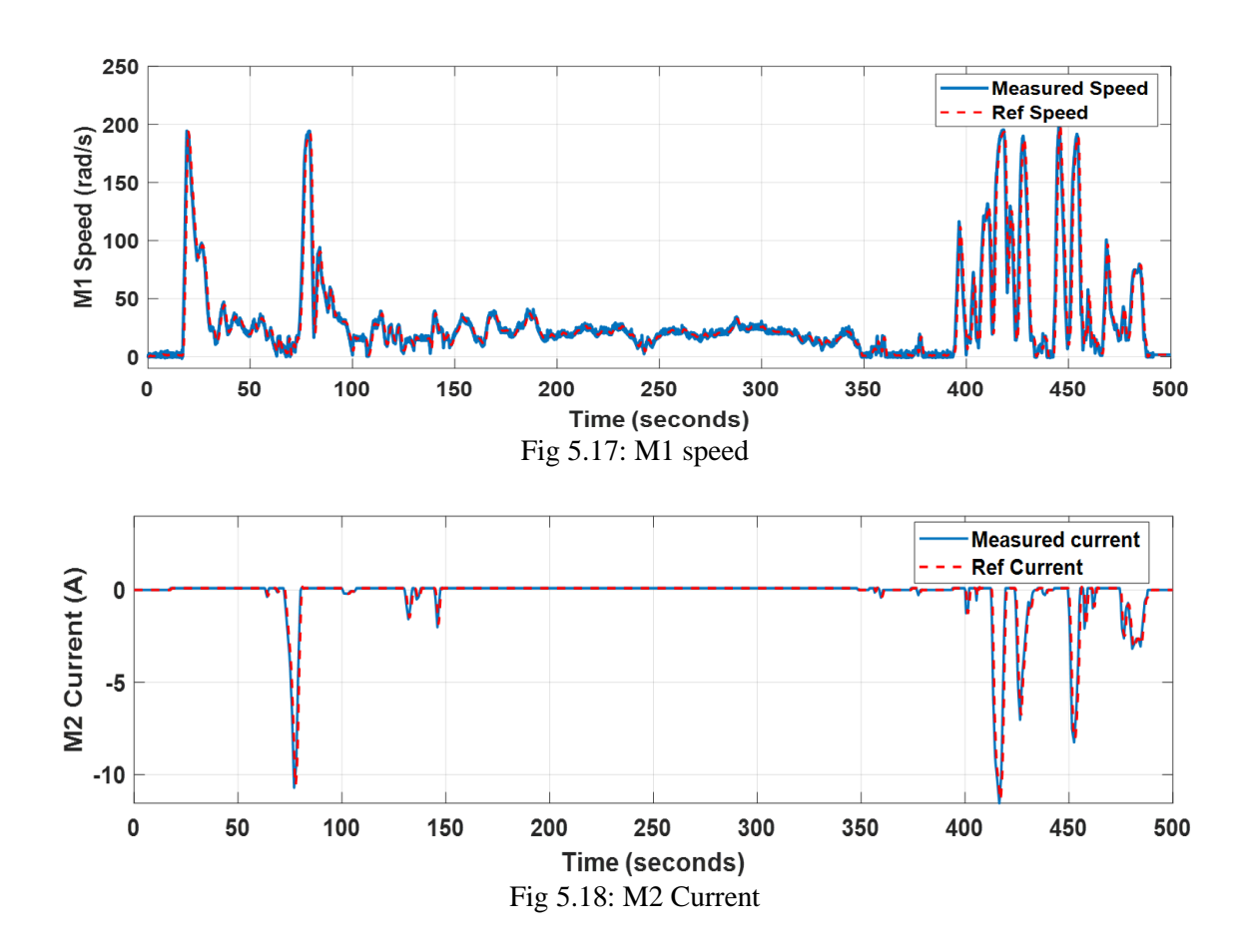


Fig 5.16: Results of recognition within the test-driving cycle

To emulate the traction part, the power profile generated from the previously shown FTP72 drive cycle was used as a reference profile. Specifically, the positive portion of the power profile was used as the M1 speed reference, while the negative portion was used as the M2 torque reference. During the discharge phase, the system operated with a variable positive speed and constant torque, placing M1 in quadrant 1 and ensuring that the frequency behavior of the power was dictated by the speed profile. In the braking phase, a constant speed with variable negative torque was applied, making the power's frequency behavior dependent on the torque profile and transitioning M1 from quadrant 1 to quadrant 4. This approach allowed the system to accurately represent the energy dynamics of real-world driving conditions. Results in Fig 5.17 demonstrate that M1 speed closely tracks its reference signal, with only a small overshoot. Fig 5.18 also shows that the M2 current matches its reference signal precisely. This current corresponds to the resistance torque exerted on M1.

Fig 5.19 represents the evolution of traction current during this process demonstrating that M1 operated under realistic load scenarios throughout the tests.



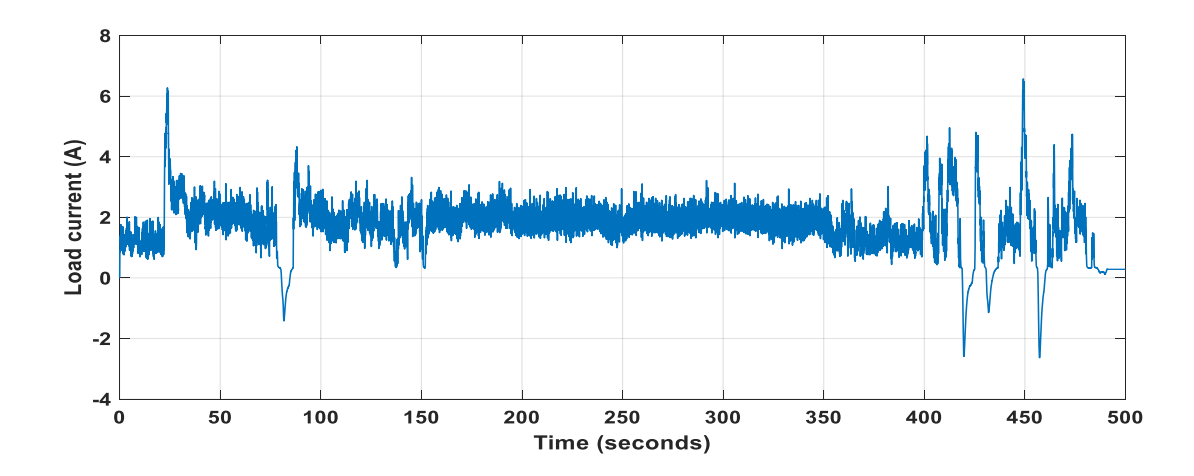


Fig 5.19: Current of load

A comparative analysis is conducted to assess the impact of DPR on WT adaptability, using a traditional WT with fixed decomposition levels. Fig 5.20(a) gives details about the battery's discharge current at different wavelet decomposition levels, clearly showing that AWT can lower the discharge current. Moreover, Fig 5.20 (b) shows the charge/discharge current of the supercapacitor, demonstrating its ability to manage significant peak currents. Higher decomposition levels effectively filter out high-frequency components, improving the supercapacitor's rapid charge/discharge capabilities and decreasing battery current variations.

Tables 5.6 and 5.7 verify those results by comparing the RMS values of the obtained battery current for the EMSs implemented. AWT technique appears as the most efficient strategy, with RMS reductions ranging from 3.28 to 21.85% when compared to traditional WT with a fixed decomposition level.

The battery Soc indicates a slower reduction of 0.001% in comparison to the initial Soc when exposed to AWT, as illustrated in Fig 5.20(c). This behavior is due to combining the WT with DPR. This result refers to the dynamic power distribution between the battery and supercapacitor, which is adjusted in real-time based on DPR. When examining the details provided in Table 5.4, it is clear that the battery Soc curve variations are smoother at higher wavelet decomposition levels. This smoother progression helps reduce battery SoC consumption, with final SoC values of 79.9987%, 79.99885%, and 79.9989% for decomposition levels 2, 3, and 4, respectively. At the same time, higher wavelet decomposition levels direct high-frequency components to the supercapacitors, aligning their soc changes with these variations, as shown in Fig 5.20(d).

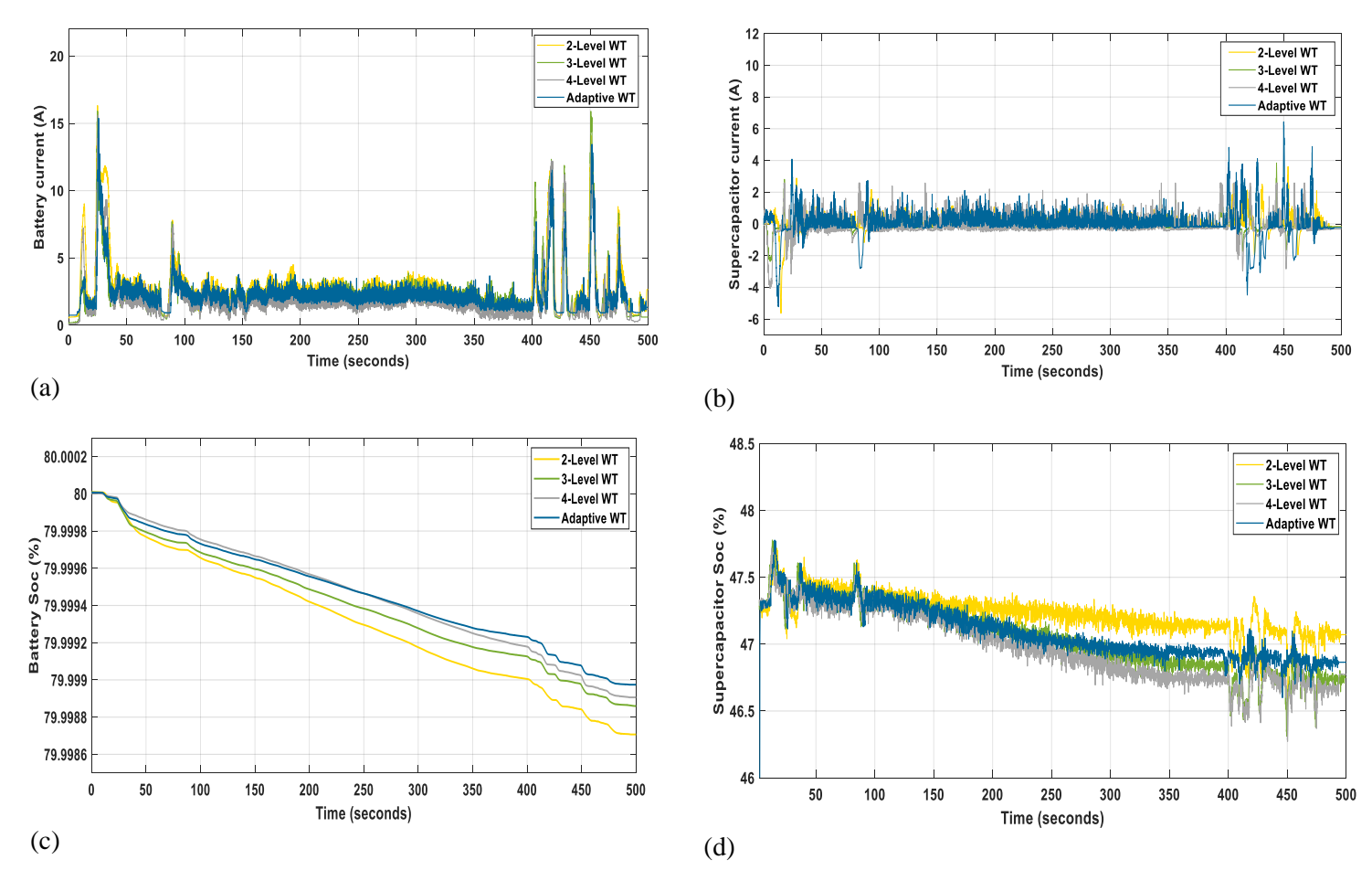


Fig 5.20: Results of experiments with wavelet transform, both fixed and adaptive: (a) Current of battery; (b) Current of supercapacitor; (c) Battery state of charge; (d) Supercapacitor state of charge.

Table 5.5: Assessment criteria results.

Parameters	2-Level WT	3-Level WT	4-Level WT	AWT	AWT-FL	AWT-AFL
Battery RMS current (A)	3,5	2,964	2,828	2,735	2,732	2,163
Supercapacitor RMS current (A)	0,4904	0,4097	0,6708	0,8374	0,9345	0,9546
Battery peak current (A)	16,32	15,9	15,62	15,39	14,15	13,5
Terminal Battery Soc (%)	79,9987	79,99885	79,9989	79,999	79,99917	79,9992
Terminal Supercapacitor Soc (%)	47,11	46,78	46,75	46,85	47,02	47,63

Dc-link voltage fluctuations (%)	21,08271	20,55604	20,55604	14,67813	13,91813	11,59854	

Table 5.6: Reduction in AWT RMS battery current compared to fixed-WT

Donomotora			
Parameters	AWT vs	2-Level AWT vs 3-Level	WT AWT vs 4-Level
	WT		WT
Battery current RMS reduction	on (%) 21.85 %	7.726%	3.28 %
Duttery current KWIS reduction	SH (70) 21.03 70	7.72070	3.20 /0
		12	
	Adaptive WT-FL Adaptive WT-Adaptive FL	210	Adaptive WT-FL
	Adaptive Wi-Adaptive LE	Supercapacitor current (A) 2- 3- 4- 5- 6- 7- 7- 7- 8- 8- 9- 8- 9- 9- 9- 9- 9- 9	——Adaptive WT-Adaptiv
		ē 6	
N	-	บี 4	116
			Table 14 and 11 les
L. M		eg og g	
		ğ -2	
Marika Marika Marika Arabin Kabupatan Arabin Kabupatan Kabupatan Kabupatan Kabupatan Kabupatan Kabupatan Kabupat		o -4	סיו וויק
		·	
0 50 100 150 200 250 300	350 400 450 500	-6 0 50 100 150 2	00 250 300 350 400 450
Time (seconds)	350 400 450 500		Time (seconds)
		(b)	
.0002		49	
.0002	——Adaptive WT	49	— Adaptive WT
.0002	Adaptive WT-FL		—— Adaptive WT —— Adaptive WT-FL
80			
80	Adaptive WT-FL		Adaptive WT-FL
80	Adaptive WT-FL		Adaptive WT-FL
.9998 - .9996 -	Adaptive WT-FL		Adaptive WT-FL
.9998 - .9996 -	Adaptive WT-FL		Adaptive WT-FL
.9998 - .9996 -	Adaptive WT-FL		Adaptive WT-FL
1.9998 1.9996 1.9994	Adaptive WT-FL	49 (%) 30C (%) 48.5 47.5 48.5 47.5 48.5 48.5 47.5 48.5 48.5 47.5 48.5 48.5 48.5 48.5 48.5 48.5 48.5 48	Adaptive WT-FL
.9998 .9996	Adaptive WT-FL	48.5 - 48.5 - 48.4 - 47.5 - 48.4 - 47.5 - 47.5 - 48	Adaptive WT-FL
80 1.9998 1.9996 1.9994 - 1.9992	Adaptive WT-FL	88 - 48.5	Adaptive WT-FL
.9998 - .9996 - .9994 -	Adaptive WT-FL Adaptive WT-Adaptive FL	48.5 - 48.5 - 48.4 - 47.5 - 48.4 - 47.5 - 47.5 - 48	Adaptive WT-Adaptive

Fig 5.21: Results of experiments conducted with various adaptive techniques: (a) Current of battery; (b) Current of supercapacitor; (c) Battery state of charge; (d) Supercapacitor state of charge.

From the results above, it is strongly evident that the adaptive version outperforms the fixed counterpart. This prompts a comparison of the adaptive versions used in this study: AWT-AFL, AWT-FL, and AWT, which is done by adopting several criteria as follows:

Battery current RMS

The changes in battery and supercapacitor current curves are shown in Fig 5.21(a) and Fig 5.21(b), respectively. The results show that the EMS based on AWT-AFL has fewer fluctuations compared to AWT-FL and AWT. This obvious reduction in fluctuations leads to a significantly smoother battery current profile, thus decreasing the battery damage. Additionally, as shown in Table 5.7, the proposed EMS achieves an important reduction in RMS current, with a 20.92% decrease compared to the AWT strategy and a 20.83% decrease compared to the AWT-FL. This considerable reduction highlights the efficiency of the proposed strategy in enhancing and stabilizing the performance of batteries.

Maximum battery current

The proposed strategy also performs well in reducing peak current, with a maximum battery current of 13.5 A, representing a notable 4.59% decrease compared to the AWT-FL strategy's peak of 14.15 A. Moreover, the reduction becomes even more significant at 12.28% when compared to the AWT strategy, which has a peak current of 15.39 A. Fig 5.22 illustrates the effectiveness of the proposed strategy in minimizing peak battery current. A depth analysis is provided through a probability assessment across specific current ranges, utilizing the following equation to calculate the probability:

$$P(i_p) = \frac{n(i_p)}{n(s)} \tag{5.6}$$

Within the [10 A-15 A] range, the proposed EMS demonstrates a notably low probability of 7.5%, outperforming AWT (8.79%) and AWT-FL (8%). In the [15 A-20 A] range, the proposed EMS entirely eliminates the occurrence of peaks, whereas AWT-FL shows a probability of 1% and AWT a slightly higher 4%. This detailed analysis further highlights the precision and efficiency of the proposed strategy in controlling and reducing peak battery currents.

Table 5.7: Comparison of the proposed EMS to AWT-FL and AWT in terms of battery current RMS and peak reduction

Parameters	Proposed EMS vs AWT-FL	Proposed EMS vs AWT
Battery current RMS reduction (%)	20.83%	20.92%
Maximum Battery current reduction (%)	4.59%	12.28 %

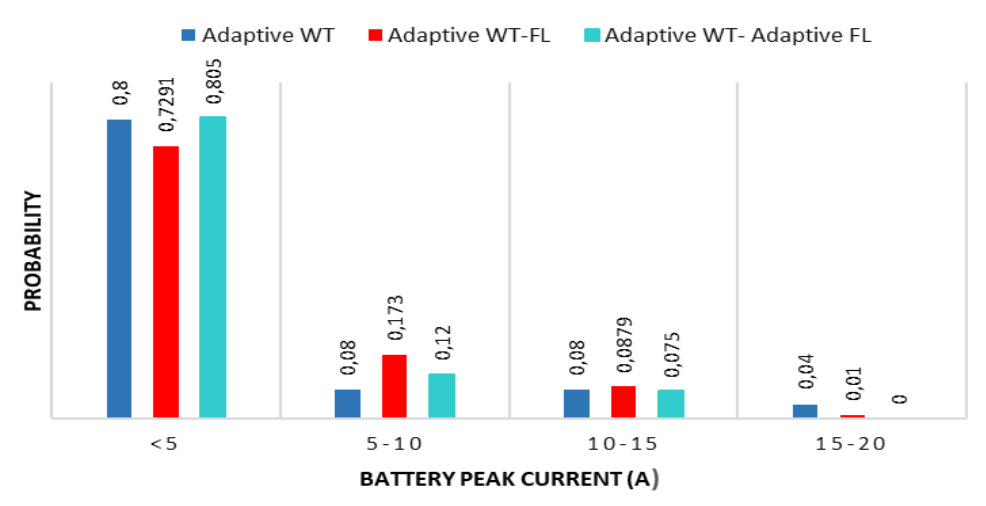


Fig 5.22: The distribution of battery current peaks under adopted techniques.

> Rate of change of battery current

The effectiveness of the suggested technique is further emphasized by its ability to reduce the rate of change of battery current $\frac{di_b}{dt}$, an essential parameter defined through the Equation (7) [136]:

$$\frac{di_b}{dt} = \left(\frac{i_{b-\text{max}} - i_{b-\text{min}}}{t_{\text{max}} - t_{\text{min}}}\right) \tag{5.7}$$

This parameter indicates the rate at which the current flowing into or out of the battery changes. Consequently, Fig 5.23 offers a detailed representation of the stress placed on the battery by

showing the normal distribution of this parameter, characterized by a mean δ_{ib} , standard deviation σ_{ib} , and variance σ_{ab}^2 , as expressed by the following probability distribution [142]:

$$f(\frac{di_b}{dt}, \delta_{ib}, \sigma_{ib}) = \frac{1}{\sigma_{ib}\sqrt{2\pi}} \exp\left[-\frac{(\frac{di_b}{dt} - \delta_{ib})^2}{2\sigma_{ib}^2}\right]$$
(5.8)

In the AWT-AFL scenario, the rate of change mostly stays within a small range of [0 - 7.5] A, showing that the battery experiences less operational stress. However, the AWT-FL strategy has a wider range, with the rate of change in battery current reaching up to 9.4 A, and the AWT strategy goes even higher, up to 10.6 A. This detailed analysis shows that the battery experiences significantly less operational stress under AWT-AFL compared to AWT-FL and AWT. This suggests that the proposed strategy successfully reduces higher and sudden changes in battery current, limiting the growth of Li+ concentration and preventing the film's irregular, steeper gradients, both of which are affecting battery life[143].

Under the proposed control strategy, the supercapacitor current consistently exceeds that of the AWT-FL strategy and AWT, showing that it effectively manages all peak currents by supplying power during periods of peak demand. Moreover, the supercapacitor's output current shows a dynamic pattern, alternating between positive and negative values, indicating charging and discharging operations. The charging was attributed only to the supercapacitor due to the battery slow charging requirements and the short braking periods. In contrast, discharging is specifically designed to handle the transient portions of the load current demand. This charge/discharge functionality allows the supercapacitor to adjust to the vehicle's energy needs in real-time, optimizing energy flow and usage. As a result, the battery's electrochemical structure stays protected from sudden changes in load demand, leading to safer operation and a longer battery lifespan.

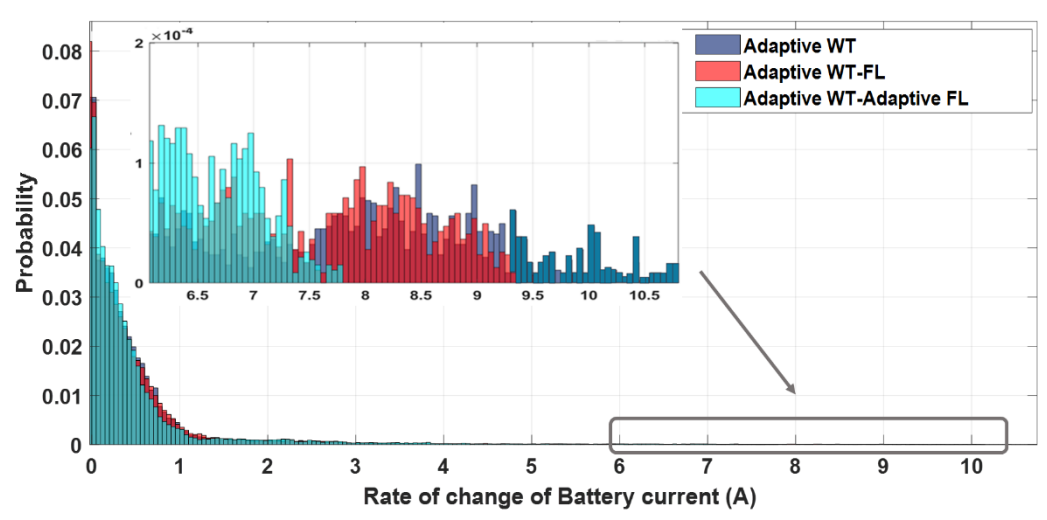


Fig 5.23: Battery current rate of change Distribution within tested strategies.

➤ Battery state of charge

A comparative analysis of the battery and the supercapacitor soc is provided in Fig 5.21(c) and (d). Fig 5.21 (c) focuses on the battery's SoC, which is initially set to 80% for all EMSs. In comparison to the other two strategies, it appears that the AWT-AFL strategy finishes the driving cycle with a higher battery SoC. For EMSs using AWT, AWT-FL, and AWT-AFL, the final battery Soc values are 79,999%, 79,99917%, and 79,9992%, respectively. On the other hand, Fig 5.17(d) indicates the supercapacitors Soc changes over time where 47.3% is set as the initial value for the adopted EMSs. It is worth noting that AWT-FL completes the driving cycle with a 0.17% higher supercapacitor Soc than AWT, according to the description in Table 5.5, where fuzzy logic control is used to keep the supercapacitor Soc within predetermined limits (60%) and minimize battery peaks by assisting these peaks with the supercapacitor. Because the initial value was lower than the intended Soc, the AWT-FL attempted to achieve a balance between the battery current output and supercapacitor Soc consumption. While the supercapacitor Soc gains 0.33% at the end of the driving cycle for AWT-AFL EMS. AFL control enables more flexible current use for both the battery and supercapacitor based on real-time recognition findings. This approach aims to keep the supercapacitor's soc close to the target level by recovering more braking energy, consuming less battery current, and preventing high battery current peaks.

> Dc-link voltage fluctuations

Furthermore, the importance of the proposed EMS is determined by the frequent voltage fluctuations in the bus caused by sudden changes in EV load current. A well-designed EMS is crucial in greatly reducing V_{dc} [136]. This decrease is accomplished through the optimal use of the supercapacitor, especially during abrupt load changes.

$$Fv_{dc} = \left(\frac{v_{\text{max}} - v_{\text{min}}}{v_{dc}}\right).100$$
(5.9)

Fig 5.24 presents a comparison of DC-link voltage using different strategies, comprising the proposed approach, AWT-FL, and AWT, over the testing cycle. The evaluation shows that Fv_{dc} of AWT exceeded both AWT-FL and AWT-AFL, with AWT reaching 14.67%, while AWT-FL and AWT-AFL achieved 13.91% and 11.59%, respectively, as detailed in Table 5.5. This confirms the ability of the proposed strategy, not only in reducing bus voltage fluctuations but also in improving the system's overall stability and performance of the system under varying EV load situations.

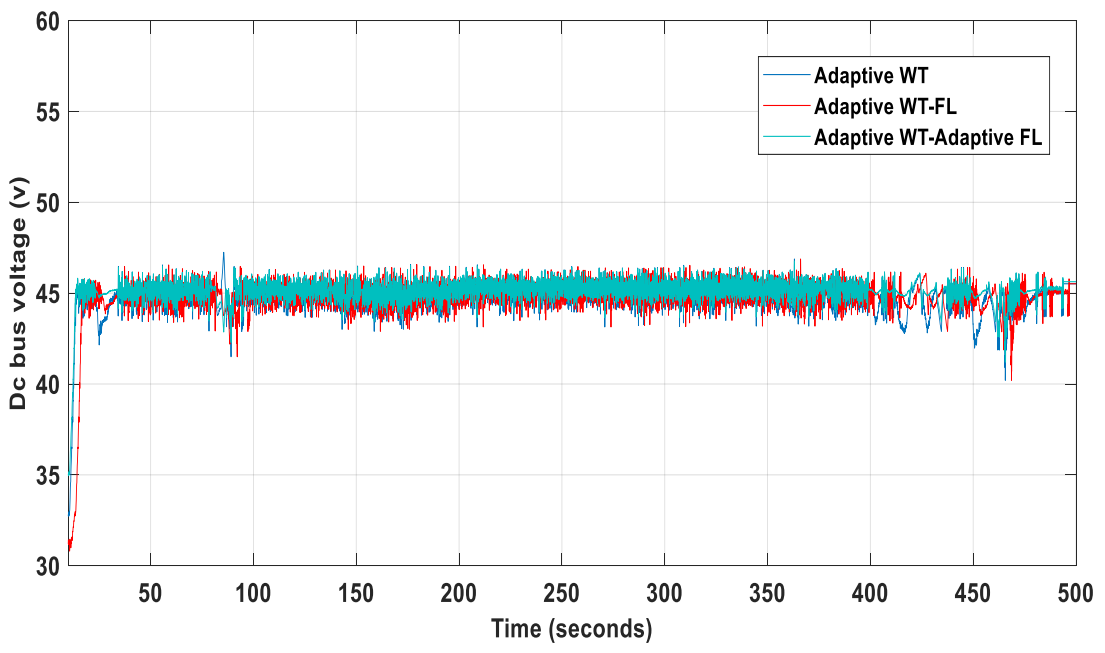


Fig 5.24: Dc-bus voltage using adopted strategies.

The results mentioned above reveal that the AWT-FL EMS excels at assuring the optimum functioning of both the battery and the supercapacitor within their respective frequency bands.

Wavelet and fuzzy logic integration is specifically designed to accommodate diverse driving cycle types. This special benefit allows the HESS to be used efficiently and intelligently, guaranteeing a reasonable load power demand distribution while accounting for the characteristics of the different drive cycles.

5.4. Conclusion

In this chapter, we presented experimental results following the description of the test bench setup, which was used to validate the earlier study. This bench enabled us to assess the effectiveness of energy management algorithms developed using an adaptive wavelet-based supercapacitor SoC supervisor. The success of this phase encouraged us to further explore adaptivity to driving conditions by implementing an Adaptive Wavelet EMS with K-Means-SVM pattern recognition alongside Adaptive Fuzzy Logic. Additionally, the traction system of the vehicle was accurately emulated to reflect the real behavior of an electric vehicle during both the acceleration and energy recuperation phases. The experimental results validated the proposed EMS, offering a promising approach for extending battery life and reducing overall operational costs in electric vehicles.

Chapter 6

Conclusion and future work

6.1. Conclusion

Electric vehicles currently available in the market use batteries as their primary energy source. However, these batteries face significant challenges, particularly in terms of energy delivery capabilities and lifespan, especially under varying and high-demand driving conditions. To overcome these limitations, researchers have developed HESS, which combine two types of energy storage devices: batteries and supercapacitors. In such configuration, batteries are used as the main energy storage device because of their high energy density, which allows them to store large amounts of energy for extended driving ranges. However, batteries have relatively low power density, making them less efficient at handling sudden surges in power demand, which is common in dynamic driving situations. On the other hand, supercapacitors have a much higher power density, enabling them to quickly deliver or absorb power during short, high-power demands like acceleration or regenerative braking. This complementary relationship between batteries and supercapacitors enhances the overall performance and longevity of the ESS.

Many studies have proposed various hybrid topologies that integrate batteries and supercapacitors in different ways to optimize performance. The topology presented in this thesis is an active configuration, where both the battery and supercapacitor are connected to the DC bus through a bidirectional DC-DC converter. This allows flexible control over power flow, ensuring that each storage device operates in its optimal range. The DC-DC converter manages the charging and discharging of both devices, dynamically allocating power between the battery and supercapacitor based on the vehicle's power demands.

In many HESS designs, a frequency-based control strategy is employed to manage power flow to the DC bus. This strategy typically assigns lower-frequency power demands (sustained energy needs) to the battery, while higher-frequency components (rapid power fluctuations) are handled by the supercapacitor. While effective in theory, this approach has limitations in real-world applications. It often lacks adaptability to changing driving conditions, such as rapid transitions between different driving modes (e.g., city driving, highway driving). Furthermore, the frequency-based strategy is challenging to implement in real-time control systems due to its reliance on offline calculations, making it difficult to respond to real-time variations in vehicle power demand.

This thesis presents enhancements to frequency-based EMS by introducing an adaptive wavelet-based approach that optimizes power distribution in a HESS by dynamically adjusting the wavelet

decomposition level according to the supercapacitor's charge state, the system effectively handles sudden power demands, significantly reducing the strain on the battery during high-load situations. Real-time experiments comparing this approach with other frequency-based methods confirm its effectiveness. The findings prove an improvement in battery lifespan through:

- A reduction in RMS current by up to 34% compared to fixed cut-off frequency methods. In comparison, conventional wavelet and adaptive cut-off frequency techniques showed reductions of 9.36% to 14.63% and 13%, respectively, indicating lower energy losses.
- Improved battery performance during high-current peaks, with a reduction of 44.53% compared to fixed cut-off frequency methods. This outperformed the conventional wavelet and adaptive cut-off frequency methods, which showed reductions between 9.78% and 27.86% and 7.40%, respectively.

These techniques give promising results in terms of performance, allowing the power demanded by the load to be distributed suitably over the two sources.

Based on the previous approach, a novel EMS is proposed to deal with challenges imposed by the driving conditions. This approach consists of two essential components: an adaptive wavelet that expertly supervises the power allocation to each source and as a complementary component, adaptive fuzzy logic that maintains the supercapacitor continuously at the desired level, preventing peak current surges. Additionally, integrating k-means clustering and Support Vector Machine recognition improves the driving pattern recognition system, enhancing the adaptability of the wavelet-fuzzy system to various driving conditions. The experimental validation shows an interesting increase in battery lifespan, as proven by several notable contributions:

- A significant decrease in the battery's operational stress was observed, with AWT-AFL limited to a range of [0, 7.5] A. In comparison, AWT-FL covers 9.4 A, and AWT extends up to 10.6 A.
- A reduction of up to 20.83% in RMS current was achieved compared to AWT-FL, which exceeds the 0.09% reduction observed with AWT.
- An important reduction in peak battery current occurrences, particularly in the [10 A 15
 A] range, where the probability is low at 7.5%, compared to 8.79% for AWT and 8% for

AWT-FL. In the [15 A - 20 A] range, the new energy management system eliminates the probability of peaks, while AWT-FL has a 1% probability and AWT has a 4% probability.

 A clear decrease in bus voltage oscillations is observed, with the proposed method outperforming both AWT-FL and AWT, achieving a reduction of 14.67% compared to their values of 13.91% and 11.59%, respectively.

Although online experimental validation presents obvious challenges, the dedication to thoroughly testing and improving the strategy in real conditions enhances the authority and practicality of the results. These results reveal a promising approach to increasing battery longevity, which can lead to reduced overall operational costs in electric vehicles

6.2. Future work

For future work, this research suggests further exploration in the following areas:

- Investigate the integration of various energy sources, such as fuel cells, into the existing system. This expansion will provide greater flexibility in energy management and improve overall efficiency by allowing for better utilization of diverse energy sources.
- Focus on creating a robust algorithm to accurately estimate the State of Charge of the battery.
 This algorithm will help ensure that the battery operates within optimal ranges, providing crucial information for effective energy management.
- Integrate battery State of Health into the energy management systems. By considering the
 condition of the battery, the system can make more informed decisions about power
 allocation, ultimately leading to improved durability and reliability of the energy storage
 system.
- Account for the temperature of energy sources in the optimization process. By regulating the sources around a nominal temperature value, we can mitigate risks associated with overheating or cold conditions, thus prolonging the lifespan and efficiency of the hybrid energy system.

Create an EMS that relies entirely on artificial intelligence such as reinforcement learning.
 This advanced system will utilize machine learning and data-driven approaches to optimize energy distribution, predict energy needs, and adapt to changing conditions in real time.

6.3. Publication

- Hasrouri, M., Charrouf, O., Betka, A., & Abdeddaim, S. (2024). Experimental validation of a real-time energy management system using four frequency-based approaches. *Journal of Energy Storage*, 79, 110139.
 https://doi.org/10.1016/j.est.2023.110139
- Mourad, T., Omar, C., Malika, H., Achour, B., Kethiri, F. M., & Sabrina, A. (2024).
 Experimental validation of a real-time fuzzy logic-based MPPT controller for a PEM fuel cell emulator system. *Studies in Engineering and Exact Sciences*, 5(1), 2774-2798.
 https://doi.org/10.54021/seesv5n1-137
- Hasrouri, M., Charrouf, O., Betka, A., & Abdeddaim, S. (2022, May). Wavelet-based control approach for hybrid energy storage system. In 2022 19th International Multi-Conference on Systems, Signals & Devices (SSD) (pp. 509-514). IEEE. https://doi.org/10.1109/SSD54932.2022.9955967

References

- [1] S. Tang, Y. Wan, F. Shang, S. Wang, and J. Jiang, "Urban non-point source pollution modelling: A physics-informed neural network approach," Copernicus Meetings, 2023. Accessed: Feb. 02, 2024. [Online]. Available: https://meetingorganizer.copernicus.org/EGU23/EGU23-2543.html
- [2] P. Mala *et al.*, "Sustainable Decision-Making Approach for Dual-Channel Manufacturing Systems under Space Constraints," *Sustainability*, vol. 13, no. 20, p. 11456, Oct. 2021, doi: 10.3390/su132011456.
- [3] L. E. Mitchell *et al.*, "A multi-city urban atmospheric greenhouse gas measurement data synthesis," *Sci. Data*, vol. 9, no. 1, p. 361, 2022, Accessed: Feb. 02, 2024. [Online]. Available: https://www.nature.com/articles/s41597-022-01467-3
- [4] A. Sharma, S. Narayan Singh, and V. Strezov, "Sustainability impact assessment of urban energy transformation in smart cities," in *EGU General Assembly Conference Abstracts*, 2023, p. EGU-17148. Accessed: Feb. 02, 2024. [Online]. Available: https://ui.adsabs.harvard.edu/abs/2023EGUGA..2517148S/abstract
- [5] G. E. M. Abro, S. A. B. Zulkifli, K. Kumar, N. El Ouanjli, V. S. Asirvadam, and M. A. Mossa, "Comprehensive Review of Recent Advancements in Battery Technology, Propulsion, Power Interfaces, and Vehicle Network Systems for Intelligent Autonomous and Connected Electric Vehicles," *Energies*, vol. 16, no. 6, p. 2925, 2023, Accessed: Feb. 02, 2024. [Online]. Available: https://www.mdpi.com/1996-1073/16/6/2925
- [6] R. Manca, L. Mi. C. Molina, S. Hegde, A. Tonoli, N. Amati, and L. Pazienza, "Optimal Torque-Vectoring Control Strategy for Energy Efficiency and Vehicle Dynamic Improvement of Battery Electric Vehicles with Multiple Motors," SAE Technical Paper, 2023. Accessed: Feb. 02, 2024. [Online]. Available: https://www.sae.org/publications/technical-papers/content/2023-01-0563/
- [7] I. Banagar, A. Mahmoudzadeh Andwari, S. Mehranfar, J. Könnö, and E. Kurvinen, "Electric vehicles' powertrain systems architectures design complexity," 2023, Accessed: Feb. 02, 2024. [Online]. Available: https://oulurepo.oulu.fi/handle/10024/44739

- [8] S. Verma, "EV and its History," *INTERANTIONAL J. Sci. Res. Eng. Manag.*, vol. 07, no. 04, Apr. 2023, doi: 10.55041/IJSREM18882.
- [9] F. Alanazi, "Electric Vehicles: Benefits, Challenges, and Potential Solutions for Widespread Adaptation," *Appl. Sci.*, vol. 13, no. 10, p. 6016, 2023, Accessed: Feb. 02, 2024. [Online]. Available: https://www.mdpi.com/2076-3417/13/10/6016
- [10] R. V. Bonkuri, "A Study of Electric Vehicle and Power Management Strategies," vol. 7, no. 2, 2021.
- [11] M. Morimoto, "Which is the First Electric Vehicle?," *Electr. Eng. Jpn.*, vol. 192, no. 2, pp. 31–38, Jul. 2015, doi: 10.1002/eej.22550.
- [12] N. Tomić-Petrović, "VEHICLES FOR THE FUTURE-DILLEMAS AND PERSPECTIVES," *Trans Motauto World*, vol. 3, no. 4, pp. 155–156, 2018, Accessed: Feb. 03, 2024. [Online]. Available: https://stumejournals.com/journals/tm/2018/4/155
- [13] B. SEZEN and A. U. İŞLER, "Elektrikli Araçlarin Mevcut Durumu, Tercih Edilme Ve Edilmeme Sebepleri," *Turk. J. Mark.*, vol. 2, no. 2, pp. 82–103, 2017, Accessed: Feb. 03, 2024. [Online]. Available: https://www.tujom.org/index.php/1/article/view/19
- [14] B. Dzialo, "Charging down the Road: A Historical Analysis of the American Auto Industry and Tesla Inc.," 2018, Accessed: Feb. 03, 2024. [Online]. Available: https://scholarworks.uvm.edu/hcoltheses/228/
- [15] D. S. Rapson and E. Muehlegger, "The Economics of Electric Vehicles," *Rev. Environ. Econ. Policy*, vol. 17, no. 2, pp. 274–294, Jun. 2023, doi: 10.1086/725484.
- [16] A. Visakh and M. P. Selvan, "Smart charging of electric vehicles to minimize the cost of chargingand the rate of transformer aging in a residential distribution network," *Turk. J. Electr. Eng. Comput. Sci.*, vol. 30, no. 3, pp. 927–942, 2022, Accessed: Feb. 03, 2024. [Online]. Available: https://journals.tubitak.gov.tr/elektrik/vol30/iss3/28/
- [17] Q. Ajao and L. Sadeeq, "Overview Analysis of Recent Developments on Self-Driving Electric Vehicles," Jun. 23, 2023, *arXiv*: arXiv:2307.00016. Accessed: Feb. 03, 2024. [Online]. Available: http://arxiv.org/abs/2307.00016
- [18] V. M. Macharia, V. K. Garg, and D. Kumar, "A review of electric vehicle technology: Architectures, battery technology and its management system, relevant standards, application of artificial intelligence, cyber security, and interoperability challenges," *IET Electr. Syst. Transp.*, vol. 13, no. 2, p. e12083, Jun. 2023, doi: 10.1049/els2.12083.

- [19] T. Frambach, R. Kleisch, R. Liedtke, J. Schwarzer, and E. Figgemeier, "Environmental impact assessment and classification of 48 V plug-in hybrids with real-driving use case simulations," *Energies*, vol. 15, no. 7, p. 2403, 2022, Accessed: Feb. 03, 2024. [Online]. Available: https://www.mdpi.com/1996-1073/15/7/2403
- [20] K. Anastasiadou and N. Gavanas, "State-of-the-Art Review of the Key Factors Affecting Electric Vehicle Adoption by Consumers," *Energies*, vol. 15, no. 24, p. 9409, 2022, Accessed: Feb. 03, 2024. [Online]. Available: https://www.mdpi.com/1996-1073/15/24/9409
- [21] A. Gaonkar, H. Valladares, A. Tovar, L. Zhu, and H. El-Mounayri, "Multi-objective Bayesian optimization of lithium-ion battery cells for electric vehicle operational scenarios," *Electron. Mater.*, vol. 3, no. 2, pp. 201–217, 2022, Accessed: Feb. 03, 2024. [Online]. Available: https://www.mdpi.com/2673-3978/3/2/17
- [22] M. Iqbal, A. Benmouna, M. Becherif, and S. Mekhilef, "Survey on Battery Technologies and Modeling Methods for Electric Vehicles," *Batteries*, vol. 9, no. 3, p. 185, 2023, Accessed: Feb. 03, 2024. [Online]. Available: https://www.mdpi.com/2313-0105/9/3/185
- [23] J. Zhao and A. F. Burke, "Electric vehicle batteries: Status and perspectives of data-driven diagnosis and prognosis," *Batteries*, vol. 8, no. 10, p. 142, 2022, Accessed: Feb. 03, 2024. [Online]. Available: https://www.mdpi.com/2313-0105/8/10/142
- [24] "Lithium-ion Battery Market Size to Hit USD 387.05 Bn by 2032." Accessed: Mar. 07, 2024. [Online]. Available: https://www.precedenceresearch.com/lithium-ion-battery-market
- [25] H. A. Debella, S. M. Atnaw, and V. R. Ancha, "A Comprehensive Review on Hybrid and Electric Vehicle Energy Control and Management Strategies," *Dyn. Veh.-Basics Simul. Auton. Syst.*, 2023, Accessed: Mar. 07, 2024. [Online]. Available: https://www.intechopen.com/chapters/87182
- [26] E. ElGhanam, H. Sharf, M. S. Hassan, and A. Osman, "Performance Evaluation of Hybrid Battery–Supercapacitor-Based Energy Storage Systems for Urban-Driven Electric Vehicles," *Sustainability*, vol. 15, no. 11, p. 8747, May 2023, doi: 10.3390/su15118747.
- [27] K. Sayed, S. Abdel-Khalek, H. M. H. Zakaly, and M. Aref, "Energy Management and Control in Multiple Storage Energy Units (Battery–Supercapacitor) of Fuel Cell Electric Vehicles," *Materials*, vol. 15, no. 24, p. 8932, Dec. 2022, doi: 10.3390/ma15248932.

- [28] K. Subasinghage, K. Gunawardane, N. Padmawansa, N. Kularatna, and M. Moradian, "Modern Supercapacitors Technologies and Their Applicability in Mature Electrical Engineering Applications," *Energies*, vol. 15, no. 20, p. 7752, Oct. 2022, doi: 10.3390/en15207752.
- [29] D. Lemian and F. Bode, "Battery-Supercapacitor Energy Storage Systems for Electrical Vehicles: A Review," *Energies*, vol. 15, no. 15, p. 5683, Aug. 2022, doi: 10.3390/en15155683.
- [30] J. Ren, W. Lin, X. Liu, S. He, Z. Dongye, and L. Diao, "Full Current-Type Control-Based Hybrid Energy Storage System," *Energies*, vol. 15, no. 8, p. 2910, Apr. 2022, doi: 10.3390/en15082910.
- [31] M. J. Lencwe, S. P. D. Chowdhury, and T. O. Olwal, "Hybrid energy storage system topology approaches for use in transport vehicles: A review," *Energy Sci. Eng.*, vol. 10, no. 4, pp. 1449–1477, Apr. 2022, doi: 10.1002/ese3.1068.
- [32] M. J. Van Jaarsveld and R. Gouws, "An Active Hybrid Energy Storage System Utilising a Fuzzy Logic Rule-Based Control Strategy," *World Electr. Veh. J.*, vol. 11, no. 2, p. 34, Apr. 2020, doi: 10.3390/wevj11020034.
- [33] M. Maalandish, S. H. Hosseini, M. Sabahi, N. Rostami, and M. Khooban, "B-MIMO high step-up DC/DC converter with high capability to control inputs," *IET Power Electron.*, vol. 16, no. 9, pp. 1499–1513, Jul. 2023, doi: 10.1049/pel2.12486.
- [34] P. Chaudhari, P. Student, S. Bhusawal, A. P. Chaudhari, and N. M. Khandare, "Study Between Rule Based & Frequency Separation Energy Management Strategies within fuel cell Battery Electric Vehicles.," vol. 4, no. 4, 2020.
- [35] N. Azim Mohseni, N. Bayati, and T. Ebel, "Energy management strategies of hybrid electric vehicles: A comparative review," *IET Smart Grid*, p. stg2.12133, Sep. 2023, doi: 10.1049/stg2.12133.
- [36] T. Marzougui, E. S. Saenz, and M. Bareille, "A rule-based energy management strategy for hybrid powered eVTOL," in *Journal of Physics: Conference Series*, IOP Publishing, 2023, p. 012024. Accessed: Feb. 07, 2024. [Online]. Available: https://iopscience.iop.org/article/10.1088/1742-6596/2526/1/012024/meta
- [37] K. D. Huang, M.-K. Nguyen, and P.-T. Chen, "A Rule-Based Control Strategy of Driver Demand to Enhance Energy Efficiency of Hybrid Electric Vehicles," *Appl. Sci.*, vol. 12, no. 17, p. 8507, 2022, Accessed: Feb. 07, 2024. [Online]. Available: https://www.mdpi.com/2076-3417/12/17/8507

- [38] Z. A. Memon, D. M. Said, M. Y. Hassan, H. M. Munir, F. Alsaif, and S. Alsulamy, "Effective Deterministic Methodology for Enhanced Distribution Network Performance and Plugin Electric Vehicles," *Sustainability*, vol. 15, no. 9, p. 7078, 2023, Accessed: Feb. 07, 2024. [Online]. Available: https://www.mdpi.com/2071-1050/15/9/7078
- [39] Ö. Tan, D. Jerouschek, R. Kennel, and A. Taskiran, "Energy Management Strategy in 12-Volt Electrical System Based on Deep Reinforcement Learning," *Vehicles*, vol. 4, no. 2, pp. 621–638, 2022, Accessed: Feb. 07, 2024. [Online]. Available: https://www.mdpi.com/2624-8921/4/2/36
- [40] L. Chen, H. Hamedmoghadam, M. Jalili, and M. Ramezani, "Electric Vehicle E-hailing Fleet Dispatching and Charge Scheduling," Feb. 24, 2023, *arXiv*: arXiv:2302.12650. Accessed: Feb. 07, 2024. [Online]. Available: http://arxiv.org/abs/2302.12650
- [41] S. Liu, M. Wu, J. Chen, L. Ding, and D. Pang, "Research of Energy Management Strategy for Hybrid HEV Based on Optimization Rules," in *The proceedings of the 16th Annual Conference of China Electrotechnical Society*, vol. 891, J. He, Y. Li, Q. Yang, and X. Liang, Eds., in Lecture Notes in Electrical Engineering, vol. 891., Singapore: Springer Nature Singapore, 2022, pp. 808–816. doi: 10.1007/978-981-19-1532-1 86.
- [42] R. Abdelhedi, A. Lahyani, A. Ammari, A. Sari, and P. Venet, "Frequency Power Sharing for Battery/Supercapacitors Hybrid Energy Storage System in Electric Vehicles," *Int. Rev. Model. Simul. IREMOS*, vol. 10, p. 399, Dec. 2017, doi: 10.15866/iremos.v10i6.12364.
- [43] E. M. Asensio, G. A. Magallan, C. H. De Angelo, and F. M. Serra, "Energy management on battery/ultracapacitor hybrid energy storage system based on adjustable bandwidth filter and sliding-mode control," *J. Energy Storage*, vol. 30, p. 101569, 2020.
- [44] Q. Zhang, L. Wang, G. Li, and Y. Liu, "A real-time energy management control strategy for battery and supercapacitor hybrid energy storage systems of pure electric vehicles," *J. Energy Storage*, vol. 31, p. 101721, Oct. 2020, doi: 10.1016/j.est.2020.101721.
- [45] A. Wangsupphaphol, N. R. N. Idris, A. Jusoh, N. D. Muhamad, and S. Phichaisawat, "A Systematic Review of Energy Management System for Battery/Supercapcitor Electric Vehicle Applications," 2023, Accessed: Mar. 05, 2024. [Online]. Available: https://www.preprints.org/manuscript/202304.1178
- [46] H. Jbari, R. Askour, and B. B. Idrissi, "Fuzzy logic-based energy management strategy on dual-source hybridization for a pure electric vehicle.," *Int. J. Electr. Comput. Eng. 2088-8708*, vol.

- 12, no. 5, 2022, Accessed: Feb. 08, 2024. [Online]. Available: https://www.researchgate.net/profile/Rachid-Askour/publication/362024944_Fuzzy_logic-based_energy_management_strategy_on_dual-source_hybridization_for_a_pure_electric_vehicle/links/62d1cec35aab971198b1931b/Fuzzy-logic-based-energy-management-strategy-on-dual-source-hybridization-for-a-pure-electric-vehicle.pdf
- [47] X. Jia and M. Zhao, "A Hierarchical Energy Control Strategy for Hybrid Electric Vehicle with Fuel Cell/Battery/Ultracapacitor Combining Fuzzy Controller and Status Regulator," *Electronics*, vol. 12, no. 16, p. 3428, Aug. 2023, doi: 10.3390/electronics12163428.
- [48] M. Hasrouri, O. Charrouf, A. Betka, and S. Abdeddaim, "Experimental validation of a real-time energy management system using four frequency-based approaches," *J. Energy Storage*, vol.
- 79, p. 110139, 2024, Accessed: Mar. 05, 2024. [Online]. Available: https://www.sciencedirect.com/science/article/pii/S2352152X23035387
- [49] Y. Cao, M. Yao, and X. Sun, "An Overview of Modelling and Energy Management Strategies for Hybrid Electric Vehicles," *Appl. Sci.*, vol. 13, no. 10, p. 5947, 2023, Accessed: Mar. 05, 2024. [Online]. Available: https://www.mdpi.com/2076-3417/13/10/5947
- [50] A. Ragab, M. I. Marei, and M. Mokhtar, "Comprehensive Study of Fuel Cell Hybrid Electric Vehicles: Classification, Topologies, and Control System Comparisons," *Appl. Sci.*, vol. 13, no. 24, p. 13057, 2023, Accessed: Mar. 05, 2024. [Online]. Available: https://www.mdpi.com/2076-3417/13/24/13057
- [51] C. Du, S. Huang, Y. Jiang, D. Wu, and Y. Li, "Optimization of energy management strategy for fuel cell hybrid electric vehicles based on dynamic programming," *Energies*, vol. 15, no. 12, p. 4325, 2022, Accessed: Feb. 09, 2024. [Online]. Available: https://www.mdpi.com/1996-1073/15/12/4325
- [52] H. Yin, C. Zhao, M. Li, C. Ma, and M.-Y. Chow, "A game theory approach to energy management of an engine–generator/battery/ultracapacitor hybrid energy system," *Ieee Trans. Ind. Electron.*, vol. 63, no. 7, pp. 4266–4277, 2016, Accessed: Mar. 05, 2024. [Online]. Available: https://ieeexplore.ieee.org/abstract/document/7428943/
- [53] Q. Zhang and G. Li, "A game theory energy management strategy for a fuel cell/battery hybrid energy storage system," *Math. Probl. Eng.*, vol. 2019, 2019, Accessed: Mar. 05, 2024. [Online]. Available: https://www.hindawi.com/journals/mpe/2019/7860214/abs/

- [54] A. K. Gautam, M. Tariq, J. P. Pandey, K. S. Verma, and S. Urooj, "Hybrid Sources Powered Electric Vehicle Configuration and Integrated Optimal Power Management Strategy," *IEEE Access*, vol. 10, pp. 121684–121711, 2022, Accessed: Mar. 05, 2024. [Online]. Available: https://ieeexplore.ieee.org/abstract/document/9931721/
- [55] Y. Zhu, X. Li, Q. Liu, S. Li, and Y. Xu, "Review article: A comprehensive review of energy management strategies for hybrid electric vehicles," *Mech. Sci.*, vol. 13, no. 1, pp. 147–188, Mar. 2022, doi: 10.5194/ms-13-147-2022.
- [56] W. Yan, M.-J. Li, N. Mei, C.-Y. Qu, Y. Wang, and L.-P. Liu, "Control strategy research of electric vehicle thermal management system based on MGA-SVR algorithm," *Meas. Control*, vol. 56, no. 5–6, pp. 1026–1036, May 2023, doi: 10.1177/00202940221105851.
- [57] H.-B. Yuan, W.-J. Zou, S. Jung, and Y.-B. Kim, "A real-time rule-based energy management strategy with multi-objective optimization for a fuel cell hybrid electric vehicle," *IEEE Access*, vol. 10, pp. 102618–102628, 2022, Accessed: Feb. 09, 2024. [Online]. Available: https://ieeexplore.ieee.org/abstract/document/9896826/
- D. Yao et al., "Adaptive Equivalent Fuel Consumption Minimization Based Energy Management Strategy for Extended-Range Electric Vehicle," Sustainability, vol. 15, no. 5, p. 4607, 2023, Accessed: Feb. 10, 2024. [Online]. Available: https://www.mdpi.com/2071-1050/15/5/4607 [59] J. Zhao, J. Zhou, L. Wang, and Y. Zhao, "An Energy Management Strategy to Reduce Comprehensive Cost of Hybrid Energy Storage Systems in Electric Vehicles," Front. Energy Res., 11, 1191565, Accessed: Feb. 10, 2024. [Online]. Available: p. https://www.frontiersin.org/articles/10.3389/fenrg.2023.1191565/full
- [60] M. Schwenzer, M. Ay, T. Bergs, and D. Abel, "Review on model predictive control: an engineering perspective," *Int. J. Adv. Manuf. Technol.*, vol. 117, no. 5–6, pp. 1327–1349, Nov. 2021, doi: 10.1007/s00170-021-07682-3.
- [61] Q. Hu *et al.*, "Robust Thermal Management of Electric Vehicles Using Model Predictive Control With Adaptive Optimization Horizon and Location-Dependent Constraint Handling Strategies," *IEEE Trans. Control Syst. Technol.*, 2023, Accessed: Mar. 05, 2024. [Online]. Available: https://ieeexplore.ieee.org/abstract/document/10188476/
- [62] S. East and M. Cannon, "Scenario model predictive control for data-based energy management in plug-in hybrid electric vehicles," *IEEE Trans. Control Syst. Technol.*, vol. 30, no.

- 6, pp. 2522–2533, 2022, Accessed: Feb. 10, 2024. [Online]. Available: https://ieeexplore.ieee.org/abstract/document/9737697/
- [63] S. Pu, L. Chu, J. Hu, S. Li, and Z. Hou, "An Equivalent Consumption Minimization Strategy for a Parallel Plug-In Hybrid Electric Vehicle Based on an Environmental Perceiver," *Sensors*, vol. 22, no. 24, p. 9621, 2022, Accessed: Mar. 05, 2024. [Online]. Available: https://www.mdpi.com/1424-8220/22/24/9621
- [64] M. Fayyazi *et al.*, "Artificial Intelligence/Machine Learning in Energy Management Systems, Control, and Optimization of Hydrogen Fuel Cell Vehicles," *Sustainability*, vol. 15, no. 6, p. 5249, 2023, Accessed: Mar. 03, 2024. [Online]. Available: https://www.mdpi.com/2071-1050/15/6/5249
- [65] J. Lou, X. Yuan, M. Pan, H. Wang, and N.-F. Tzeng, "Data Privacy Examination against Semi-Supervised Learning," 2023, Accessed: Mar. 03, 2024. [Online]. Available: https://prefernsf.org/pdf/asiaccs_2023.pdf
- [66] S. Li, P. Zhao, C. Gu, D. Huo, J. Li, and S. Cheng, "Linearizing battery degradation for health-aware vehicle energy management," *IEEE Trans. Power Syst.*, 2022, Accessed: Mar. 02, 2024. [Online]. Available: https://ieeexplore.ieee.org/abstract/document/9932019/
- [67] X. Sun, Y. Cao, Z. Jin, X. Tian, and M. Xue, "An adaptive ECMS based on traffic information for plug-in hybrid electric buses," *IEEE Trans. Ind. Electron.*, vol. 70, no. 9, pp. 9248–9259, 2022, Accessed: Mar. 02, 2024. [Online]. Available: https://ieeexplore.ieee.org/abstract/document/9912303/
- [68] D. Pecioski, V. Gavriloski, S. Domazetovska, and A. Ignjatovska, "An overview of reinforcement learning techniques," in *2023 12th Mediterranean Conference on Embedded Computing (MECO)*, IEEE, 2023, pp. 1–4. Accessed: Mar. 03, 2024. [Online]. Available: https://ieeexplore.ieee.org/abstract/document/10155066/
- [69] A. R. R. Habib, "A comparative study of the machine learning-based energy management system for hydrogen fuel cell electric vehicles," *Future Technol.*, vol. 3, no. 1, pp. 13–24, 2024, Accessed: Mar. 03, 2024. [Online]. Available: https://fupubco.com/futech/article/view/103
- [70] Y. Cheng, G. Xu, and Q. Chen, "Research on Energy Management Strategy of Electric Vehicle Hybrid System Based on Reinforcement Learning," *Electronics*, vol. 11, no. 13, p. 1933, 2022, Accessed: Mar. 03, 2024. [Online]. Available: https://www.mdpi.com/2079-9292/11/13/1933

- [71] C. Wang, F. Liu, A. Tang, and R. Liu, "A dynamic programming-optimized two-layer adaptive energy management strategy for electric vehicles considering driving pattern recognition," *J. Energy Storage*, vol. 70, p. 107924, 2023, Accessed: Mar. 03, 2024. [Online]. Available: https://www.sciencedirect.com/science/article/pii/S2352152X2301321X
- [72] L. Pulvirenti, L. Rolando, and F. Millo, "Energy management system optimization based on an LSTM deep learning model using vehicle speed prediction," *Transp. Eng.*, vol. 11, p. 100160, 2023, Accessed: Mar. 03, 2024. [Online]. Available: https://www.sciencedirect.com/science/article/pii/S2666691X23000015
- [73] H. Sun, F. Tao, Z. Fu, A. Gao, and L. Jiao, "Driving-behavior-aware optimal energy management strategy for multi-source fuel cell hybrid electric vehicles based on adaptive soft deep-reinforcement learning," *IEEE Trans. Intell. Transp. Syst.*, vol. 24, no. 4, pp. 4127–4146, 2023, Accessed: Mar. 03, 2024. [Online]. Available: https://ieeexplore.ieee.org/abstract/document/10007717/
- [74] M. Martí-Florences, A. Cecilia, and R. Costa-Castelló, "Modelling and Estimation in Lithium-Ion Batteries: A Literature Review," *Energies*, vol. 16, no. 19, p. 6846, Sep. 2023, doi: 10.3390/en16196846.
- [75] Skill-Lync, "Week 1 Understanding Different Battery Chemistry," Skill-Lync. Accessed: May 03, 2024. [Online]. Available: https://skill-lync.com/student-projects/week-1-understanding-different-battery-chemistry-257
- [76] CT, "LiFePO4 CONTRE. Li-ion contre. Guide complet de la batterie Li-Po," Professional Lithium Battery Manufacturer Vendor. Accessed: May 03, 2024. [Online]. Available: https://www.lithiumbatterytech.com/fr/lifepo4-vs-li-ion-vs-li-po-battery-complete-guide/
- [77] M. Tekin and M. İ. Karamangil, "Comparative analysis of equivalent circuit battery models for electric vehicle battery management systems," *J. Energy Storage*, vol. 86, p. 111327, May 2024, doi: 10.1016/j.est.2024.111327.
- [78] T. Huria, M. Ceraolo, J. Gazzarri, and R. Jackey, "High fidelity electrical model with thermal dependence for characterization and simulation of high power lithium battery cells," in 2012 IEEE International Electric Vehicle Conference, Greenville, SC: IEEE, Mar. 2012, pp. 1–8. doi: 10.1109/IEVC.2012.6183271.

- [79] Z. Haizhou, "Modeling of Lithium-ion Battery for Charging/Discharging Characteristics Based on Circuit Model," *Int. J. Online Eng. IJOE*, vol. 13, no. 06, p. 86, Jun. 2017, doi: 10.3991/ijoe.v13i06.6799.
- [80] C. Yang, X. Wang, Q. Fang, H. Dai, Y. Cao, and X. Wei, "An online SOC and capacity estimation method for aged lithium-ion battery pack considering cell inconsistency," *J. Energy Storage*, vol. 29, p. 101250, 2020, Accessed: Aug. 22, 2024. [Online]. Available: https://www.sciencedirect.com/science/article/pii/S2352152X19311028
- [81] A. Abdisattar *et al.*, "Recent advances and challenges of current collectors for supercapacitors," *Electrochem. Commun.*, vol. 142, p. 107373, 2022, Accessed: Jul. 13, 2024. [Online]. Available: https://www.sciencedirect.com/science/article/pii/S1388248122001758
- [82] X. Chen, R. Paul, and L. Dai, "Carbon-based supercapacitors for efficient energy storage," *Natl. Sci. Rev.*, vol. 4, no. 3, pp. 453–489, 2017, Accessed: Jul. 13, 2024. [Online]. Available: https://academic.oup.com/nsr/article-abstract/4/3/453/3058971
- [83] S. Marín-Coca, A. Ostadrahimi, S. Bifaretti, E. Roibás-Millán, and S. Pindado, "New Parameter Identification Method for Supercapacitor Model," *IEEE Access*, vol. 11, pp. 21771–21782, 2023, doi: 10.1109/ACCESS.2023.3250965.
- [84] X. Zhang, H. Xue, Y. Xu, H. Chen, and C. Tan, "An investigation of an uninterruptible power supply (UPS) based on supercapacitor and liquid nitrogen hybridization system," *Energy Convers. Manag.*, vol. 85, pp. 784–792, Sep. 2014, doi: 10.1016/j.enconman.2014.01.058.
- [85] Y. Wang, Z. Sun, and Z. Chen, "Development of energy management system based on a rule-based power distribution strategy for hybrid power sources," *Energy*, vol. 175, pp. 1055–1066, 2019.
- [86] P. Shrivastava, T. K. Soon, M. Yamani Bin Idris, and S. Mekhilef, "Lithium-ion Battery Model Parameter Identification Using Modified Adaptive Forgetting Factor-Based Recursive Least Square Algorithm," in 2021 IEEE 12th Energy Conversion Congress & Exposition Asia (ECCE-Asia), Singapore, Singapore: IEEE, May 2021, pp. 2169–2174. doi: 10.1109/ECCE-Asia49820.2021.9479079.
- [87] L. Zubieta and R. Bonert, "Characterization of double-layer capacitors for power electronics applications," *IEEE Trans. Ind. Appl.*, vol. 36, no. 1, pp. 199–205, Feb. 2000, doi: 10.1109/28.821816.

- [88] N. Mohamed, F. Aymen, Z. M. Ali, A. F. Zobaa, and S. H. E. Abdel Aleem, "Efficient Power Management Strategy of Electric Vehicles Based Hybrid Renewable Energy," *Sustainability*, vol. 13, no. 13, Art. no. 13, Jan. 2021, doi: 10.3390/su13137351.
- [89] T. A. Zarma, A. A. Galadima, and M. A. Aminu, "Review of Motors for Electrical Vehicles," *J. Sci. Res. Rep.*, pp. 1–6, Oct. 2019, doi: 10.9734/jsrr/2019/v24i630170.
- [90] National University Of Sciences And Technology, Karachi Campus, H. Ahmed, Capt. Dr. S. H. Zaidi, National University Of Sciences And Technology, Karachi Campus, F. Khan, and National University Of Sciences And Technology, Karachi Campus, "A Comparative Study on Different Motors used in Electric Vehicles," *J. Indep. Stud. Res. Comput.*, vol. 20, no. 2, Dec. 2022, doi: 10.31645/JISRC.22.20.2.5.
- [91] A Laidani, M Benghanem, M Bouhamida, and Z Bellahcene, "Commande Sans Capteur de Vitesse D'un Moteur à Courant Continu," 2012, doi: 10.13140/RG.2.2.33694.84801.
- [92] V. Vodovozov, Z. Raud, and E. Petlenkov, "Review on Braking Energy Management in Electric Vehicles," *Energies*, vol. 14, no. 15, p. 4477, Jul. 2021, doi: 10.3390/en14154477.
- [93] L. C. Rosario, "Power and energy management of multiple energy storage systems in electric vehicles," Sep. 2008, Accessed: Aug. 15, 2024. [Online]. Available: http://hdl.handle.net/1826/2992
- [94] x-engineer.org, "EV design energy consumption x-engineer.org." Accessed: Aug. 03, 2024. [Online]. Available: https://x-engineer.org/ev-design-energy-consumption/
- [95] J. Yano, S. Nishimura, K. Fukunaga, M. Nakajima, H. Yamada, and M. Moriguchi, "Estimation of EV Power Consumption and Route Planning Using Probe Data".
- [96] x-engineer.org, "EV design battery calculation x-engineer.org." Accessed: Aug. 04, 2024. [Online]. Available: https://x-engineer.org/ev-design-battery-calculation/
- [97] "What is the output voltage of a boost converter with given input and load current?," Quora. Accessed: Aug. 04, 2024. [Online]. Available: https://www.quora.com/What-is-the-output-voltage-of-a-boost-converter-with-given-input-and-load-current
- [98] D. Petreus, D. Moga, R. Galatus, and R. A. Munteanu, "Modeling and Sizing of Supercapacitors," *Adv. Electr. Comput. Eng.*, vol. 8, no. 2, pp. 15–22, 2008, doi: 10.4316/aece.2008.02003.

- [99] L. Zhang, X. Xia, and F. Barzegar, "Control of a battery/supercapacitor hybrid energy storage system for electric vehicles," in *2017 36th Chinese Control Conference (CCC)*, IEEE, 2017, pp. 9560–9565.
- [100] A. Florescu, S. Bacha, I. Munteanu, A. I. Bratcu, and A. Rumeau, "Adaptive frequency-separation-based energy management system for electric vehicles," *J. Power Sources*, vol. 280, pp. 410–421, Apr. 2015, doi: 10.1016/j.jpowsour.2015.01.117.
- [101] N. Guruwacharya *et al.*, "Data-Driven Power Electronic Converter Modeling for Low Inertia Power System Dynamic Studies," Sep. 05, 2020, *arXiv*: arXiv:2009.02621. Accessed: Aug. 26, 2024. [Online]. Available: http://arxiv.org/abs/2009.02621
- [102] M. R. Ghazali, M. A. Ahmad, and R. M. T. R. Ismail, "Data-Driven PID Control for DC/DC Buck-Boost Converter-Inverter-DC Motor based on Safe Experimentation Dynamics," in *2018 IEEE Conference on Systems, Process and Control (ICSPC)*, Melaka, Malaysia: IEEE, Dec. 2018, pp. 89–93. doi: 10.1109/SPC.2018.8704161.
- [103] A. Tahri, H. El Fadil, F. Giri, and F. Z. Chaoui, "A Lyapunov based power management for a fuel cell hybrid power source for electric vehicle," in *2015 3rd International Renewable and Sustainable Energy Conference (IRSEC)*, Marrakech: IEEE, Dec. 2015, pp. 1–6. doi: 10.1109/IRSEC.2015.7454992.
- [104] B. Traore, M. Doumiati, C. Morel, J.-C. Olivier, and O. Soumaoro, "Energy management strategy design based on frequency separation, fuzzy logic and Lyapunov control for multi-sources electric vehicles," in *IECON 2019 45th Annual Conference of the IEEE Industrial Electronics Society*, Lisbon, Portugal: IEEE, Oct. 2019, pp. 2676–2681. doi: 10.1109/IECON.2019.8927661.
- [105] M. R. Çorapsız and H. Kahveci, "Double adaptive power allocation strategy in electric vehicles with battery/supercapacitor hybrid energy storage system," *Int. J. Energy Res.*, vol. 46, no. 13, pp. 18819–18838, Oct. 2022, doi: 10.1002/er.8501.
- [106] M. Masih-Tehrani, "Wavelet-based power management for hybrid energy storage system".
- [107] D. Tang and H. Wang, "Energy Management Strategies for Hybrid Power Systems Considering Dynamic Characteristics of Power Sources," *IEEE Access*, vol. 9, pp. 158796–158807, 2021, doi: 10.1109/ACCESS.2021.3131168.
- [108] K. Lei and Z. Chen, "Energy Management Strategy Based on Adaptive Wavelet Analysis for HESS," in 2019 IEEE 3rd International Electrical and Energy Conference (CIEEC), Beijing, China: IEEE, Sep. 2019, pp. 890–894. doi: 10.1109/CIEEC47146.2019.CIEEC-2019342.

- [109] Q. Zhang and W. Deng, "An adaptive energy management system for electric vehicles based on driving cycle identification and wavelet transform," *Energies*, vol. 9, no. 5, p. 341, 2016, Accessed: Sep. 03, 2024. [Online]. Available: https://www.mdpi.com/1996-1073/9/5/341
- [110] F. Chen, "Research on Transient Power Suppression Method Based on Wavelet Algorithm," *Nanjing Nanjing Univ. Aeronaut. Astronaut.*, 2016.
- [111] J. Wang, Y. Huang, H. Xie, and G. Tian, "Driving Pattern Recognition and Energy Management for Extended Range Electric Bus," in 2014 IEEE Vehicle Power and Propulsion Conference (VPPC), Coimbra, Portugal: IEEE, Oct. 2014, pp. 1–6. doi: 10.1109/VPPC.2014.7007052.
- [112] L. Han, Z. Du, S. Wang, and Y. Chen, "Analysis of Traffic Signs Information Volume Affecting Driver's Visual Characteristics and Driving Safety," *Int. J. Environ. Res. Public. Health*, vol. 19, no. 16, p. 10349, Aug. 2022, doi: 10.3390/ijerph191610349.
- [113] J. Hu, X. Niu, X. Jiang, and G. Zu, "Energy management strategy based on driving pattern recognition for a dual-motor battery electric vehicle," *Int. J. Energy Res.*, vol. 43, no. 8, pp. 3346–3364, Jun. 2019, doi: 10.1002/er.4474.
- [114] X. Zhou, J. Huang, W. Lv, and D. Li, "Fuel Consumption Estimates Based on Driving Pattern Recognition," in 2013 IEEE International Conference on Green Computing and Communications and IEEE Internet of Things and IEEE Cyber, Physical and Social Computing, Beijing, China: IEEE, Aug. 2013, pp. 496–503. doi: 10.1109/GreenCom-iThings-CPSCom.2013.99.
- [115] H. He, C. Sun, and X. Zhang, "A Method for Identification of Driving Patterns in Hybrid Electric Vehicles Based on a LVQ Neural Network," *Energies*, vol. 5, no. 9, pp. 3363–3380, Sep. 2012, doi: 10.3390/en5093363.
- [116] G. U. O. Jia-chen, J. Heng, L. E. I. Shi-ying, Z. Zhi-rong, Z. U. O. Hong-fu, and X. U. Juan, "Vehicle driving cycle construction method of urban roads," 交通运输工程学报, vol. 20, no. 6, pp. 197–209, 2020.
- [117] M. Li, Y. Wang, P. Yu, Z. Sun, and Z. Chen, "Online adaptive energy management strategy for fuel cell hybrid vehicles based on improved cluster and regression learner," *Energy Convers. Manag.*, vol. 292, p. 117388, Sep. 2023, doi: 10.1016/j.enconman.2023.117388.

- [118] T. Li, Y. Ma, and T. Endoh, "Normalization-Based Validity Index of Adaptive K-Means Clustering for Multi-Solution Application," *IEEE Access*, vol. 8, pp. 9403–9419, 2020, doi: 10.1109/ACCESS.2020.2964763.
- [119] A. Kabra, Clustering of Driver Data based on Driving Patterns. 2019.
- [120] C. Liu and Y. Liu, "Energy Management Strategy for Plug-In Hybrid Electric Vehicles Based on Driving Condition Recognition: A Review," *Electronics*, vol. 11, no. 3, p. 342, Jan. 2022, doi: 10.3390/electronics11030342.
- [121] S. L. Karri, L. C. De Silva, D. T. C. Lai, and S. Y. Yong, "Classification and Prediction of Driving Behaviour at a Traffic Intersection Using SVM and KNN," *SN Comput. Sci.*, vol. 2, no. 3, p. 209, May 2021, doi: 10.1007/s42979-021-00588-7.
- [122] H. Kong and D. Wu, "Research on Land Use Classification Method of High Resolution Remote Sensing Image Based on SVM," *Acad. J. Sci. Technol.*, vol. 7, no. 2, pp. 111–114, Sep. 2023, doi: 10.54097/ajst.v7i2.11953.
- [123] Y. Ma, C. Li, and S. Wang, "Multi-objective energy management strategy for fuel cell hybrid electric vehicle based on stochastic model predictive control," *ISA Trans.*, vol. 131, pp. 178–196, Dec. 2022, doi: 10.1016/j.isatra.2022.04.045.
- [124] P. Shao, W. Shi, Z. Liu, and T. Dong, "Unsupervised Change Detection Using Fuzzy Topology-Based Majority Voting," *Remote Sens.*, vol. 13, no. 16, p. 3171, Aug. 2021, doi: 10.3390/rs13163171.
- [125] D. Samanta, "Defuzzification Techniques," *IIT Kharagpur*, 2018, Accessed: Feb. 18, 2024. [Online].

 Available:
- http://213.55.90.4/admin/home/Dmu%20Academic%20Resource/Institute%20of%20Technology/Electrical%20and%20Computer%20Engineering/4th%20Year/FL-03%20Defuzzification.pdf
- [126] H. Maghfiroh, A. Sujono, M. Ahmad, and C. H. B. Apribowo, "Basic Tutorial on Sliding Mode Control in Speed Control of DC-motor," *J. Electr. Electron. Inf. Commun. Technol.*, vol. 2, no. 1, Apr. 2020, doi: 10.20961/jeeict.2.1.41354.
- [127] R. A. Soumana, M. J. Saulo, and C. M. Muriithi, "Enhanced Speed Control of Separately Excited DC Motor Using Fuzzy-Neural Networks Controller," in *2022 4th International Conference on Smart Systems and Inventive Technology (ICSSIT)*, Tirunelveli, India: IEEE, Jan. 2022, pp. 729–736. doi: 10.1109/ICSSIT53264.2022.9716556.

- [128] D. Adel and B. Assam, "COMMANDE EN VITESSE D'UN MOTEUR A COURANT CONTINU PAR BACKSTEPPING".
- [129] "DC motor speed control." Accessed: Sep. 04, 2024. [Online]. Available: https://sciamble.com/resources/pe-drives-lab/basic-drives/dc-speed-control
- [130] A. A. Salem, N. A. N. Aldin, A. M. Azmy, and W. S. E. Abdellatif, "Implementation and Validation of an Adaptive Fuzzy Logic Controller for MPPT of PMSG-Based Wind Turbines," *IEEE Access*, vol. 9, pp. 165690–165707, 2021, doi: 10.1109/ACCESS.2021.3134947.
- [131] S. Mensou, A. Essadki, T. Nasser, B. B. Idrissi, and L. Ben Tarla, "Dspace DS1104 implementation of a robust nonlinear controller applied for DFIG driven by wind turbine," *Renew. Energy*, vol. 147, pp. 1759–1771, Mar. 2020, doi: 10.1016/j.renene.2019.09.042.
- [132] P. Sotoodeh, "A SINGLE-PHASE MULTI-LEVEL D-STATCOM INVERTER USING MODULAR MULTI-LEVEL CONVERTER (MMC) TOPOLOGY FOR RENEWBLE ENERGY SOURCES".
- [133] Yumpu.com, "Application Note IGBT Power Electronics Teaching ... Semikron," yumpu.com. Accessed: Sep. 11, 2024. [Online]. Available: https://www.yumpu.com/en/document/view/4877701/application-note-igbt-power-electronics-teaching-semikron
- [134] Đ. Lazarević, M. Živković, Đ. Kocić, and J. Ćirić, "The utilizing Hall effect-based current sensor ACS712 for true RMS current measurement in power electronic systems," *Sci. Tech. Rev.*, vol. 72, no. 1, pp. 27–32, 2022, doi: 10.5937/str2201027L.
- [135] K. Lei and Z. Chen, "Energy Management Strategy Based on Adaptive Wavelet Analysis for HESS," in *2019 IEEE 3rd International Electrical and Energy Conference (CIEEC)*, Beijing, China: IEEE, Sep. 2019, pp. 890–894. doi: 10.1109/CIEEC47146.2019.CIEEC-2019342.
- [136] V. P. Sidharthan, Y. Kashyap, and P. Kosmopoulos, "Adaptive-Energy-Sharing-Based Energy Management Strategy of Hybrid Sources in Electric Vehicles," *Energies*, vol. 16, no. 3, p. 1214, Jan. 2023, doi: 10.3390/en16031214.
- [137] H.-L. T. Nguyen, B.-H. Nguyễn, T. Vo-Duy, and J. P. F. Trovão, "A Comparative Study of Adaptive Filtering Strategies for Hybrid Energy Storage Systems in Electric Vehicles," *Energies*, vol. 14, no. 12, p. 3373, Jun. 2021, doi: 10.3390/en14123373.

- [138] J. Hu, D. Liu, C. Du, F. Yan, and C. Lv, "Intelligent energy management strategy of hybrid energy storage system for electric vehicle based on driving pattern recognition," *Energy*, vol. 198, p. 117298, May 2020, doi: 10.1016/j.energy.2020.117298.
- [139] A. T. Abdel-Wahed, Z. Ullah, A. S. Abdel-Khalik, M. S. Hamad, S. Ahmed, and N. Elmalhy, "Drive Cycle-Based Design With the Aid of Data Mining Methods: A Review on Clustering Techniques of Electric Vehicle Motor Design With a Case Study," *IEEE Access*, vol. 11, pp. 115775–115797, 2023, doi: 10.1109/ACCESS.2023.3325400.
- [140] D. Yi, J. Su, C. Liu, M. Quddus, and W.-H. Chen, "A machine learning based personalized system for driving state recognition," *Transp. Res. Part C Emerg. Technol.*, vol. 105, pp. 241–261, Aug. 2019, doi: 10.1016/j.trc.2019.05.042.
- [141] S. L. Karri, L. C. De Silva, D. T. C. Lai, and S. Y. Yong, "Classification and Prediction of Driving Behaviour at a Traffic Intersection Using SVM and KNN," *SN Comput. Sci.*, vol. 2, no. 3, p. 209, May 2021, doi: 10.1007/s42979-021-00588-7.
- [142] P. Bhandari, "Normal Distribution | Examples, Formulas, & Uses," Scribbr. Accessed: Feb. 27, 2024. [Online]. Available: https://www.scribbr.com/statistics/normal-distribution/
- [143] M. K. Jangid and A. Mukhopadhyay, "Real-time monitoring of stress development during electrochemical cycling of electrode materials for Li-ion batteries: overview and perspectives," *J. Mater. Chem. A*, vol. 7, no. 41, pp. 23679–23726, 2019, doi: 10.1039/C9TA06474E.